

***The Use of Coordination Chemistry Principles to
Control Aggregation Processes of Metal Ions***

***Dissertation
Sanjit Nayak
Universität Karlsruhe (TH)***

The Use of Coordination Chemistry Principles to Control Aggregation Processes of Metal Ions

Zur Erlangung des akademischen Grades eines

DOKTORS DER NATURWISSENSCHAFTEN

(Dr. rer. nat.)

der Fakultät für Chemie und Biowissenschaften der
Universität Karlsruhe (TH)
angenommene

DISSERTATION

von

Sanjit Nayak
(Master of Science)

aus Burdwan (Indien)

Dekan: Prof. Dr. Stefan Bräse
Referent: Prof. Dr. Annie K. Powell
Korreferent: Prof. Dr. Peter Roesky
Tag der mündlichen Prüfung: 23.10.2008

This thesis was completed in the period from September 2005 until September 2008 in the Institut für Anorganische Chemie der Universität Karlsruhe (TH) under the supervision of Prof. Dr. Annie K. Powell.

*Dedicated to
Ma and Baba*

“The chemists are a strange class of mortals, impelled by an almost maniacal impulse to seek their pleasure amongst smoke and vapour, soot and flames, poison and poverty, yet amongst all these evils I seem to live so sweetly that I would rather die than change places with the King of Persia.”

Johann Joachim Becher, *Physica Subterranea* (1667)

ACKNOWLEDGEMENTS

The research presented in this thesis would not have been possible without the generous help and support of many people. In this section I would like to thank and acknowledge all of them.

First of all, I would like to thank my Ph. D. supervisor, Prof. Annie K. Powell, for her great care and guidance throughout the three years of my research. Despite her very busy schedule, she always had time to hear about problems as well as new achievements. I will never forget the freedom of research that was possible during my time in Karlsruhe. She is one of the best individuals and supervisors that I have ever met.

I am grateful to Dr. Yanhua Lan, Prof. Rodolphe Clérac, and Prof. Wolfgang Wernsdorfer for their help in magnetic measurements and analyses.

I would like to thank Dr. Christopher E. Anson for his kind help with crystallographic measurements and structural analyses, many of which were really difficult with severe disorder. Many thanks to Dr. Henning Henke for his sincere helps, speciall with powder XRD instrument.

At the Forschungszentrum, Karlsruhe, I would like to thank Dr. Sharali Malik for performing several SEM, FIB and high-temperature analyses of my samples. I would also like to thank Priv. Doz. Dr. Carsten Von Hänisch and Dr. Sylvio Indris for their help in dynamic light scattering and capacitance measurements, respectively.

I would like to thank Frau Gertraud Amschlinger and Herr Rolf Lehmann for their daily help in the department. Thanks to Frau Gabi Kuhn, Frau Sybille Böker and Herr Kalam Munshi for their kind help in the chemical store and the glass blowing facilities.

Special thanks to Dr. Lianne Beltran who joined our group while I was planning to write my thesis. Without her sincere help, this thesis would not be in its present form. My real introduction to scientific writing has been through her. I am also grateful to her for her help in learning X-ray crystal structure analysis. I will miss our discussions.

Special thanks to Dr. Ghenadie Novitchi for his help and explanations regarding many research problems. He was never busy whenever I asked for his help. I always learned something new during our discussions.

I would like to thank Sudarshana Mukherjee and Frederik Klöwer, and Julia Rink for being in the neighboring labs and sharing my frustrations and celebrations of everyday research

life. Thanks Sudarshana for proofreading my thesis too. Frederik, I think I will miss your “keine lust”! Julia, you did great help to organize things in my Ph.D. party. Thanks for that.

Thanks to my other groupmates, Dr. Ayuk M. Ako, Dr. Valeriu Mereacre, Dr. Yanzhen Zheng, Dr. George Kostakis, Dr. Usman Anwar, Dr. Ahmed Abouelwafa, Julia Rink, Ghulam Abbas, Nadeem Akhtar, Sven Pfirrmann, Jürgen Feuersenger, and Kartik C. Mondal, for providing a friendly environment throughout my stay in Karlsruhe.

I would also like to thank my previous undergraduate supervisor Prof. Parimal K. Bharadwaj and graduate mentors (Dr. Subhadip Neogi and Dr. Sujit K. Ghosh) from whom I learned many research basics. Without their help, I would not have been able to pursue this research.

Last of all, but most importantly, I would like to express my gratitude to the few persons who have motivated me since I was introduced to the alphabet. I am grateful and proud of my grandma, who never had a connection with reading or writing, but she always wished good things for me. She used to say “One day you will write with a golden pen.” This has been a constant inspiration throughout my career. I would like to express my gratitude to my cousin-brother (Mr. Saikat Pal), sister (Mrs. Sangita Nayak) and uncle (Mr. Basudeb Mandal). They have always had time to hear about my hurdles and successes.

Last, but not least, my deepest gratitude goes to my wife (Mrs. Suparna Mitra) and my parents (Mr. Bhakta Ram Nayak & Mrs. Reba Nayak) for their support during all these years. It is not easy to express in words, but I will always be there for you too.

CONTENTS

ACKNOWLEDGEMENTS	iv
CHAPTER 1 Introduction	1
1.1 Molecule-based magnets	1
1.1.1 Basic terms and definitions of magnetic properties	1
1.1.2 Single Molecule Magnet (SMMs)	5
1.1.3 Background and a brief literature review	8
1.1.3.1 A compound with a record ground state spin	8
1.1.3.2 A compound with record magnetic anisotropy	9
1.1.3.3 The prototypical SMM of iron	10
1.1.3.4 The largest iron SMM	11
1.1.3.4 The largest SMM	12
1.2 Biomineralization: Biologically controlled growth of minerals	13
1.2.1 Basic ideas	13
1.2.2 Calcium carbonate mineralization	15
1.2.2.1 The ions involved	15
1.2.2.2 Morphology and polymorph selection in CaCO ₃ mineralization	17
1.3 Thesis overview	21
CHAPTER 2 Research objectives	22
CHAPTER 3 High-nuclearity aggregates of manganese and iron using polyols: Clusters with polyhedral cores	24

3.1	A hexanuclear manganese cluster,	
	$[(\text{PtolH})_4(\text{O}_2\text{CMe})_6(\mu_6\text{-O})\text{Mn}^{\text{III}}_6] \cdot 1.5\text{en}$, 3.1 , showing SMM behavior	26
3.1.1	Introduction	26
3.1.2	Results and discussion	26
	3.1.2.1 Description of the structure	26
	3.1.2.2 Magnetic properties	28
3.2	Structure and magnetic properties of a Mn_{17} cluster compound	
	$[\text{Mn}^{\text{III}}_{11}\text{Mn}^{\text{II}}_6(\mu_4\text{-O})_8(\mu_3\text{-Cl})_4(\mu_5\text{-O}_2\text{CMe})_2(\text{DPD})_{10}\text{Cl}_{2.34}(\text{O}_2\text{CMe})_{0.66}(\text{py})_3$ $(\text{MeCN})_2] \cdot 7\text{MeCN}$, 3.2	30
3.2.1	Introduction	30
3.2.2	Results and discussion	31
	3.2.2.1 Description of the structure	31
	3.2.2.2 Magnetic properties	34
3.3	A three dimensional network:	
	$[\{\text{Mn}^{\text{III}}_{12}\text{Mn}^{\text{II}}_9(\mu_4\text{-O})_8(\text{glycH})_{12}(\mu\text{-}1,1\text{-N}_3)_6(\text{OH}_2)_6(\text{N}_3)_{1.5}\} \{\text{Mn}^{\text{II}}(\mu\text{-}1,3\text{-N}_3)_{4.5}(\text{OH}_2)_{1.5}\}] \text{Cl}_4 \cdot \text{ca.} 7.5\text{H}_2\text{O}$, 3.3	36
3.3.1	Introduction	36
3.3.2	Results and discussion	37
	3.3.2.1 Description of the structure	37
	3.3.2.2 Magnetic properties	41
3.3.3	Pyrolysis and degassing of the Mn_{21} network:	44
	3.3.3.1 Thermogravimetric analysis	45
	3.3.3.2 Powder XRD analysis	45

3.3.3.3 Infrared spectroscopy study	47
3.3.3.4 Scanning electron microscopy	49
3.3.3.5. Capacitance measurements	50
3.4 An Fe ₆ cluster: [Fe ₆ O ₂ (Piv) ₆ (PdolH) ₆](NO ₃) ₂ ·2CH ₃ CN (3.4), connecting two Fe ₃ -triangles	51
3.4.1 Introduction	51
3.4.2 Results and discussions	52
3.4.2.1 Description of the structure	52
3.4.2.2 Magnetic properties	55
3.5. Summary	55
CHAPTER 4 A family of 1D lanthanide chain compounds	58
4.1 Introduction	58
4.2 Results and discussion	59
4.2.1 Synthesis and structural description	59
4.2.2 Magnetic properties	63
4.2.2.1 Temperature dependence of susceptibility	63
4.2.2.2 Field dependence of magnetization	70
4.2.2.3 Fitting of the magnetic data for 4.3	72
4.3 Summary	74
CHAPTER 5 Control over biomineralization of CaCO₃ using simple organic Templates	75
5.1 Control over calcite crystal growth using 1,3-diamino-2-hydroxypropane- <i>N,N,N',N'</i> -tetraacetic acid, hpdtA ₅	79

5.1.1	Introduction	79
5.1.2	Results and discussion	80
5.1.2.1	Surface dependence	82
5.1.2.2	pH dependence	86
5.1.2.3	Concentration dependence	88
5.2	A systematic study on the functional group orientations and their effects on CaCO ₃ biomineralization	89
5.2.1	Introduction	89
5.2.2	Results and discussion	90
5.3	A comparative study of the mineralization of BaCO ₃ and SrCO ₃ influenced by 1,2,4-benzenetricarboxylic acid	96
5.3.1	Introduction	96
5.3.2	Results and discussion	97
5.4	Summary	104
CHAPTER 6 Conclusions		106
CHAPTER 7 Experimental		110
7.1	Materials	110
7.2	Identification and characterization of materials	110
7.2.1	X-ray crystallography	110
7.2.2	X-ray powder diffraction	110
7.2.3	FT-IR spectroscopy	110
7.2.4	Elemental analysis	111
7.2.5	Scanning electron microscopy	111
7.2.6	Dynamic light scattering	111

7.2.7	Magnetic measurements	111
7.3	Preparation of the compounds and materials	112
7.3.1	Preparation of 3.1	112
7.3.2	Preparation of 3.2	112
7.3.3	Preparation of 3.3	112
7.5	Preperation of 3.4	113
7.3.5	Preparations of 4.1-4.7	113
7.3.6	Preparation of 5.1-5.10	114
7.3.7	Preparation of 5.11-5.15	114
7.3.8	Preparation of 5.16 and 5.17	115
CHAPTER 8	Bibliography	117
Appendix I	Crystallographic data	123
Appendix II	List of crystalline compounds	125
Appendix III	List of abbreviations	125
Appendix IV	List of figures	128
Appendix V	List of schemes	131
Appendix VI	List of tables	131
CURRICULUM VITAE		132

CHAPTER 1

Introduction

Since Alfred Werner proposed the concept of coordination chemistry at the beginning of 20th century, this field has developed very fast and led to the development of many interdisciplinary areas.¹ Coordination chemistry research has revealed the potential of using molecular architecture to build well-designed compounds with interesting properties. Together with supramolecular chemistry, coordination chemistry has developed new, sophisticated ways to synthesize novel materials for catalysis, gas storage and magnetic data storage.²

In this work, research was focused on the use of small, flexible ligands in the synthesis and characterization of nanoscale metal clusters, networks and CaCO₃ aggregates. In the field of biomineralization, ligands are generally called templates because they act very often as a pattern for the synthesis of different morphologies. Although polynuclear clusters and networks of transition metals and lanthanides are of interest from many perspectives, these investigations were mainly focused on their magnetic properties (Chapters 3 and 4). Afterwards, using flexible and rigid ligands that have already been well-established in coordination chemistry, efforts were made to rationalize the controlled formation of different kinds of CaCO₃ (Chapter 5) morphologies.

1.1. Molecule-based magnets

1.1.1. Basic terms and definitions of magnetic properties

This brief introduction defines and explains basic magnetic properties. For additional details, standard text books are available.³

Behavior of a substance in magnetic field: When a substance is placed in a magnetic field (H), the density of lines of force in the sample, known as the *magnetic induction* or *magnetic flux density* (B) is related to (H) by the *permeability* of the substance (μ):

$$B = \mu H$$

$$B = \mu_0 H + \mu_0 M$$

where μ_0 is the *permeability* of free space and M is the magnetization or *magnetic moment* of the sample. Here, $\mu_0 H$ is the induction generated by the field alone and $\mu_0 M$ is the additional induction contributed by the sample. The *magnetic susceptibility* is defined as the ratio of magnetization to the field

$$\chi = \frac{M}{H}$$

and therefore,

$$\mu = \mu_0(1 + \chi)$$

The ratio μ/μ_0 , which equals to $(1+\chi)$, is known as the *relative permeability*, μ_r . The magnetic behavior of all materials can be categorized by the values of χ and μ_r and by their temperature dependence and field dependence. For a vacuum, $\mu_r = 1$. When χ is negative, the $\mu_r < 1$ and the substance is *diamagnetic*. Such a substance allows a smaller number of lines of force to pass through it (as compared to that *in vacuo*), and thus it prefers to move to the region of the lowest magnetic field strength. On the other hand, when χ is positive, then $\mu_r > 1$ and the substance is *paramagnetic*. Such a substance allows more lines of force to pass through it, and therefore prefers to move to the region of the highest magnetic field.

Effects of temperature - Curie and Curie-Weiss Laws: The susceptibilities of different kinds of magnetic materials are distinguished by both their temperature dependence and their absolute magnitudes. Many paramagnetic substances obey the simple Curie law, especially at high temperature. This states that the magnetic susceptibility is inversely proportional to temperature:

$$\chi = \frac{C}{T}$$

where C is the Curie constant. The Curie law is obeyed in materials where is not any spontaneous interaction between adjacent unpaired electrons. When there are some spontaneous interactions between adjacent spins, a better fit to the high-temperature, paramagnetic behavior is often provided by the Curie-Weiss law:

$$\chi = \frac{C}{T - \theta}$$

where θ is the Weiss constant. Depending on the ferro- or antiferromagnetism, θ is positive or negative, respectively. These two types of behavior are shown in Figure 1.1. Diamagnetic substances have their magnetic susceptibility invariant to temperature, whereas the magnetic

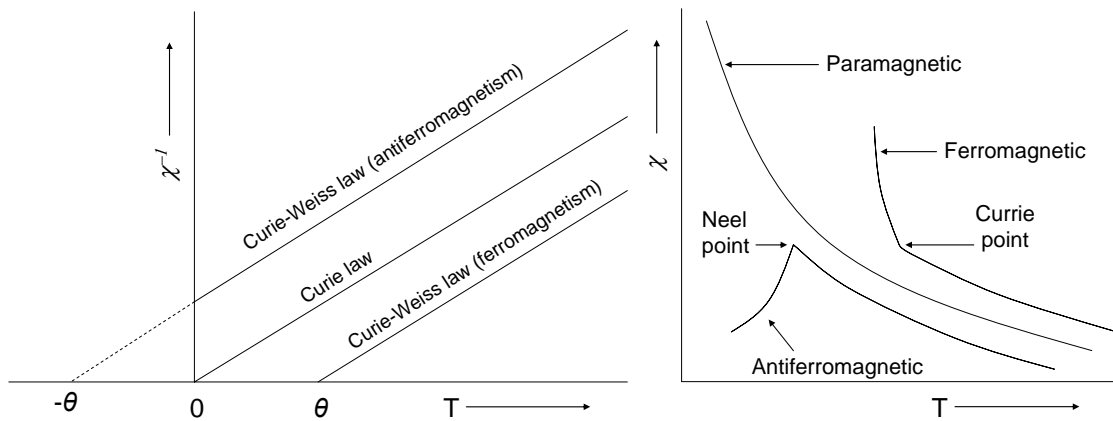


Figure 1.1: χ^{-1} versus T plot and χ versus T plot for the ferromagnetic, antiferromagnetic and paramagnetic materials.

susceptibility of a paramagnet follows an inverse relationship with temperature. An *antiferromagnet* has a characteristic *Néel temperature* (T_N) above which it behaves like a paramagnet, but below this temperature, its magnetic susceptibility decreases with decreasing temperature (Figure 1.1, right). A *ferromagnet* has a characteristic *Curie temperature* (T_c) above which it behaves like a paramagnet, but below this temperature, its magnetic susceptibility increases rapidly.

Magnetic hysteresis: When a ferromagnetic material is magnetized in one direction, it will not relax back to zero magnetization when the imposed magnetizing field is removed. It must be

driven back to zero by a field in the opposite direction. When the magnetization is plotted, a loop called a *hysteresis loop* results (Figure 1.2). The lack of retraceability of the

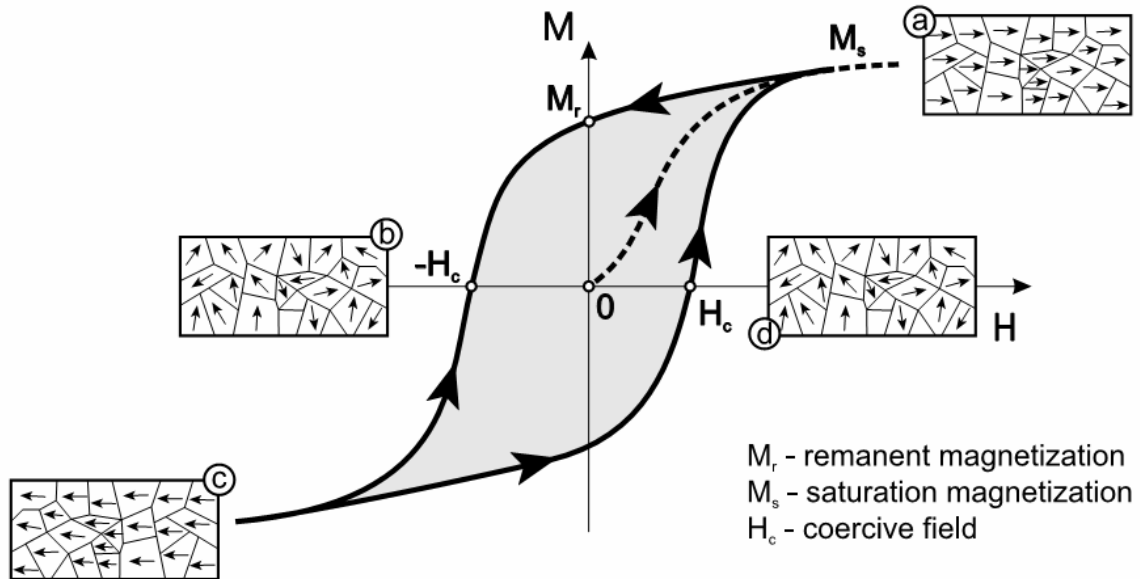


Figure 1.2: The plot of magnetization (M) versus magnetic field (H) for a ferromagnetic compound is illustrated by showing the orientations of the electrons in each domain at different points of the loop.

magnetization-curve is the property called *hysteresis*, and it is related to the existence of magnetic domains in the material. Once the magnetic domains are reoriented, it takes some energy to turn them back again. This property of ferromagnetic materials is useful as a magnetic “memory”. When the ferromagnetic material retains an imposed magnetization indefinitely, it is termed as a “permanent magnet”. The magnetic memory aspects of iron and chromium oxides make them useful in audio tape recording and for the magnetic storage of data on computer disks. As shown in Figure 1.2, the phenomena can be described in the following way: Starting at zero field, the material follows a non-linear magnetization curve and reaches the saturation level, when all the spins are aligned along the direction of a field (Figure 1.2, point a). As the field is decreased and drops to zero, the ferromagnetic material retains a considerable degree of magnetization (M_r). It can

be thought of as “remembering” the previous state of magnetization. At this point, when $H = 0$, a ferromagnet is not fully demagnetized and only a partial domain reorientation has happened. When a reverse field is applied, at a given point the magnetization reaches zero ($-H_c$). This field required to demagnetize a ferromagnetic material is called the “*coercive field*” (H_c , point b). Saturation of magnetization also achieved by applying an opposite field (point c) and then decreasing the field and reversing it again in the opposite direction completes the loop after going through a point with zero magnetization (point d).

1.1.2. Single Molecule Magnet (SMMs)

A single molecule can show all the above mentioned properties of a bulk magnet. These single molecules, termed as single-molecule magnets (SMMs) were discovered during the course of investigations into the miniaturization of the size of magnetic devices. Many difficulties have been encountered in the “top-down” approach. For example, these are often nano particles with inhomogeneous size distributions of the domains. Decreasing the domain-size also makes the magnet less efficient. As a result, research is now intensely focused on the “bottom-up” approach in order to produce nano-scale materials starting from the atomic or molecular level.⁴ The ability of a single molecule to behave like a bulk magnet caught the attention of researchers because such systems may lead to the smallest possible magnetic devices.⁵ These SMMs are of interest because they exhibit magnetic bistability of pure molecular origin. The slow relaxation in the magnetization is the source of this interesting behavior and is due to the presence of an energy barrier which has to be overcome in the reversal of the magnetic moment. This behavior has been compared to that of superparamagnetic materials. Superparamagnetic behavior occurs when a single magnetically ordered domain has a reorientation barrier that is comparable to the thermal energy.⁶ As a consequence, the magnetization flips freely and its time average is zero, as in a paramagnet. In an external field, it behaves like a paramagnet until the temperature is sufficiently reduced such that

the barrier can not be easily overcome. Thus the magnetization is blocked, below a blocking temperature, T_B , and the superparamagnet reverts to its usual bulk behavior (*i.e.* ferro-, ferri-, or antiferromagnetic). For a molecule to have a barrier in a system of ground spin S , it must have the magnetic sub-states, $M = \pm S$ lying lowest in energy. In the case of axial symmetry, where the system has an integer spin in the ground state, the height of the energy barrier (ΔE) can be associated with the difference between the lowest energy $M = \pm S$ states and the highest energy $M = 0$ state. For a negative axial zero-field splitting parameter, D , $\Delta E = |D|S^2$ (for integer-spin) and $\Delta E = |D|(S^2 - 1/4)$ (for half-integer-spin). To produce new nanomagnetic materials based on molecular clusters, it is therefore necessary to achieve a reasonably large ground state spin. For this purpose $S = 5/2$ ions such as high-spin Mn^{II} and Fe^{III} are well-suited metal ions for SMM. Subsequently a large ground state spin can be achieved just by using a small number of ions.

The prototypical SMM $[\text{Mn}_{12}\text{O}_{12}(\text{CH}_3\text{COO})_{16}(\text{H}_2\text{O})_4] \cdot 2\text{CH}_3\text{COOH} \cdot 4\text{H}_2\text{O}$, abbreviated to $\text{Mn}_{12}\text{-ac}$,⁷ is a suitable example to illustrate SMM behavior. The structure of the compound is shown below (Figure 1.3). The $\text{Mn}_{12}\text{-ac}$ cluster contains twelve manganese ions, bridged *via* oxygen atoms. In the structure, four Mn^{IV} ions reside on the alternating vertices of a central cubane. All of these Mn^{4+} ($3d^3$, $S = 3/2$) ions are ferromagnetically coupled. The other vertices are occupied by four μ_4 -oxo groups. The other eight ions are Mn^{3+} , and they define a crown-like geometry surrounding the Mn_4 -cubane. All these eight Mn^{3+} ($3d^4$, $S = 2$) ions are also ferromagnetically coupled. Although the Mn^{4+} and Mn^{3+} ions in the inner cubane and outer crown are ferromagnetically coupled among themselves, the total spins of these two parts are coupled antiferromagnetically to give a total net spin of 10 ($8 \times 2 - 4 \times 3/2 = 10$). The two spin states ($M_S = +10$ and -10) are separated by an energy barrier of Around 50 cm^{-1} (Figure 1.4). The blocking temperature was found to be 3 K for this $\text{Mn}_{12}\text{-ac}$ molecule. The ac magnetic susceptibility measurements enabled the measurement of the relaxation rate. In this process, the susceptibility of a sample is measured using a weak magnetic

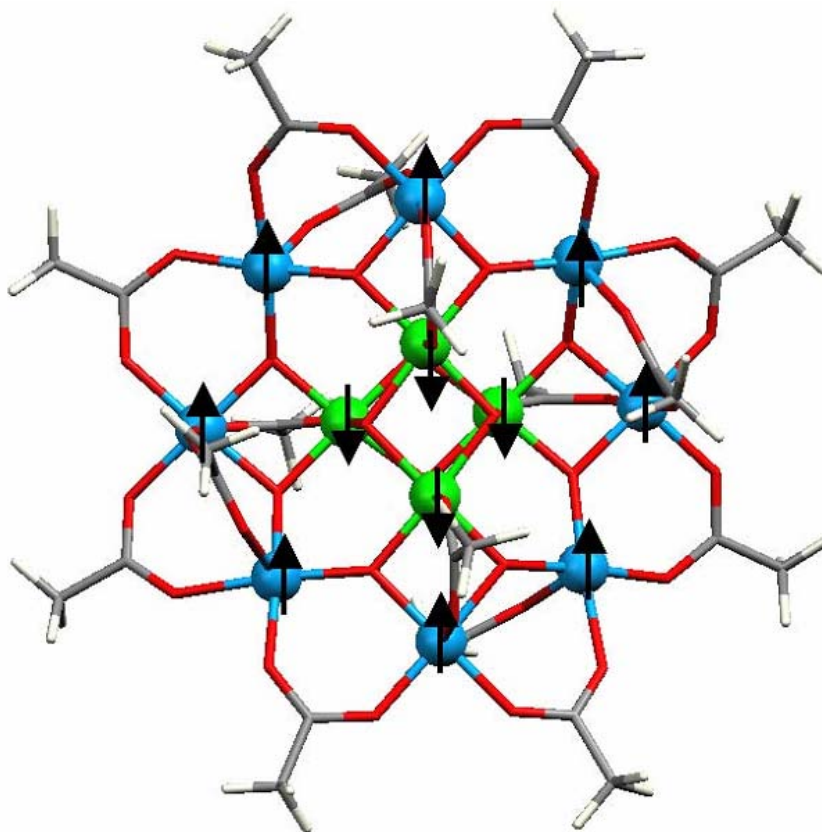


Figure 1.3: Structure of $[\text{Mn}_{12}\text{O}_{12}(\text{CH}_3\text{COO})_{16}(\text{H}_2\text{O})_4] \cdot 2\text{CH}_3\text{COOH} \cdot 4\text{H}_2\text{O}$ (abbreviated $\text{Mn}_{12}\text{-ac}$)⁷. Green, blue, red and grey centers represent Mn^{IV} , Mn^{III} , O and C atoms, respectively. The arrows indicate the resultant spin orientation of different Mn ions. Four Mn^{4+} ($3d^3$, $S = 3/2$) are ferromagnetically coupled for a total spin of $S = 6$. The remaining eight Mn^{3+} ($3d^4$, $S = 2$) are also ferromagnetically coupled to one another in a crown structure resulting into a total spin of $S = 16$. The Mn^{3+} crown is antiferromagnetically coupled to the inner Mn^{4+} cubane, yielding a total spin of $S = 10$.

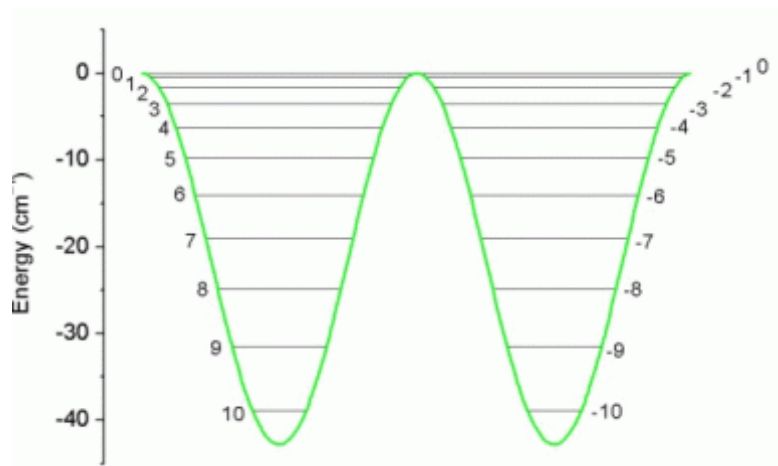


Figure 1.4: Energy level diagram of $S = 10$. The horizontal lines are the energies of the spin microstates belonging to the $S = 10$ multiplet.

field (usually of approximately 1000 Oe) that switches direction at a fixed frequency. As the switching frequency starts to approach the relaxation rate for the magnetization of the molecules, the measured susceptibility or the in-phase or real component of the ac susceptibility (χ') begins to diminish. Accordingly, the out-of-phase or the imaginary component of the ac susceptibility (χ'') increases. Using these data, the energy barrier (ΔE) and the relaxation rate (τ) can be obtained using an Arrhenius plot. After plotting $\ln\tau$ versus $1/T$ (T = temperature), τ_0 and ΔE can be obtained, where τ_0 is the relaxation time of the resultant spin of the molecule.

$$\tau = \tau_0 e^{\frac{\Delta E}{k_B T}}$$

In this work, attempts were made to design new compounds with high ground state spins and high magnetic anisotropy using the self-assembly of metal ions (mainly Mn, Fe and lanthanides) and flexible organic ligands containing potential bridging groups such as alcohols and carboxylic acids.

1.1.3. Background and a brief literature review

Research on multinuclear manganese and iron clusters began about 40 years ago with the aim of mimicking clusters of such metals found in biology, such as the oxygen evolving center of photosynthesis and the iron storage center of the protein ferritin.⁸ Subsequently, it was realized that high nuclearity clusters of paramagnetic metal ions can be used to build SMMs. Some examples of magnetically interesting metal clusters are discussed below.

1.1.3.1. A compound with a record ground state spin: Many compounds having interesting magnetic behavior have been recently synthesized. For example, a $[\text{Mn}^{\text{III}}_{12}\text{Mn}^{\text{II}}_7(\mu_4\text{-O})_8(\mu_3, \eta^1\text{-N}_3)_8(\text{HL})_{12}(\text{MeCN})_6]\text{Cl}_2 \cdot 10\text{MeOH} \cdot \text{MeCN}$ (H_3L = 2,6-bis(hydroxy-methyl)-4-methylphenol) cluster (Figure 1.5), synthesized by Ako *et al.*, possesses a record spin of $S = 83/2$ (Figure 1.5).⁹ Besides having such a high-spin ground state, the compound is also interesting from the structural point of view. It contains two tetrahedral units of Mn_{10} linked *via* a common vertex.

All the vertices of the tetrahedron are occupied by Mn^{II} ions and a Mn^{III} lies at the center of each edge. Interestingly, it was found that all the manganese centers in this molecule are ferromagnetically coupled. An example of a structurally related ($\text{Mn}^{\text{II}}_6\text{Mn}^{\text{III}}_{11}$) cluster with high ground spin state was synthesized during the course of this research and is described in Section 3.2.

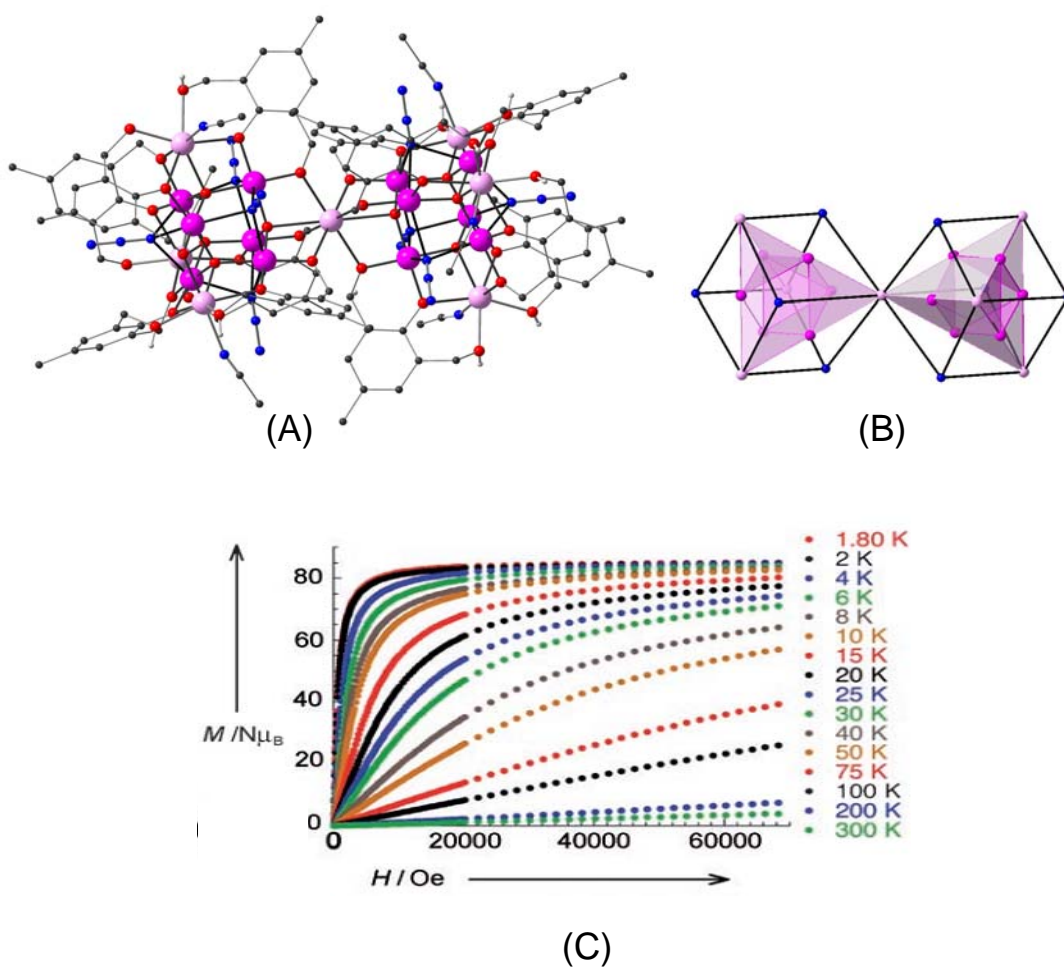


Figure 1.5: (A) The structure of the $[\text{Mn}^{\text{III}}_{12}\text{Mn}^{\text{II}}_7(\mu_4\text{-O})_8(\mu_3, \eta^1\text{-N}_3)_8(\text{HL})_{12}(\text{MeCN})_6]^{2+}$ cluster. Black, blue, red, dark violet and light violet spheres representing C, N, O, Mn^{III} and Mn^{II} atoms, respectively. (B) The rationalized view of the cluster with two tetrahedral units linked *via* a common vertex. (C) Magnetization plot showing the high ground state spin.

1.1.3.2. A compound with record magnetic anisotropy: A class of hexanuclear manganese clusters, $[\text{Mn}^{\text{III}}_6\text{O}_2(\text{sao})_6(\text{O}_2\text{CPh})_2(\text{EtOH})_4]$ ($\text{saoH}_2 = 2\text{-hydroxybenzaldehyde oxime}$), was synthesized by Milios *et al.* using relatively bulky oxime ligands. (Figure 1.6).¹⁰ They also reported that by using a bulkier derivative of saoH_2 , the magnetic interactions can be modified from

antiferromagnetic to ferromagnetic exchange. By using 2-hydroxy-(3,5-dimethyl phenyl)-propanone oxime, it was possible to obtain a distorted cluster $[\text{Mn}^{\text{III}}_6\text{O}_2(\text{Et-sao})_6(\text{O}_2\text{CPh}(\text{Me})_2)_2(\text{EtOH})_6]$ that possesses a ground state spin of $S = 12$ and a record energy barrier of 86.4 K for magnetization relaxation.

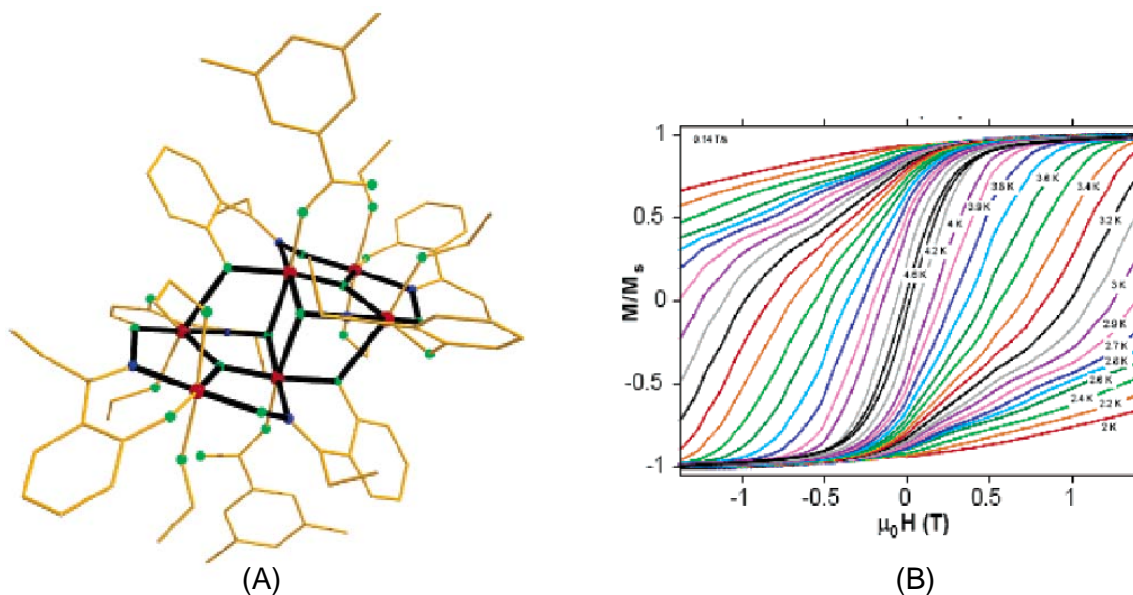


Figure 1.6: (A) Molecular Structure of the compound $[\text{Mn}^{\text{III}}_6\text{O}_2(\text{Et-sao})_6(\text{O}_2\text{CPh}(\text{Me})_2)_2(\text{EtOH})_6]$. Color code: Mn, red; O, green; N, blue. (B) Showing slow relaxation of magnetization at different temperatures.

1.1.3.3. The prototypical SMM of iron: An octanuclear iron cluster, $[\text{Fe}_8\text{O}_2(\text{OH})_{12}(\text{tacn})_6]\text{Br}_8$ (tacn = 1,4,7-triazacyclononane), was synthesized long before its¹¹, SMM behavior was observed¹², as in the case of the Mn_{12} -ac compound. This was the first iron compound properly identified as a SMM. The compound was synthesized using $[\text{Fe}(\text{tacn})\text{Cl}_3]$ and NaBr in H_2O . The compound (Figure 1.7.) contains a central unit of four Fe^{III} ions linked by two $\mu_3\text{-O}^{2-}$ groups in a “butterfly” arrangement. Bound to the metals of this central core via hydroxide bridges are four additional Fe^{III} centres. These and the wing metals of the “butterfly” are capped by tridentate tacn ligands. The ground spin state of this compound was found to be $S = 10$.¹³ The superparamagnet-like behavior was established by both Mössbauer and ac magnetic susceptibility measurements.¹²

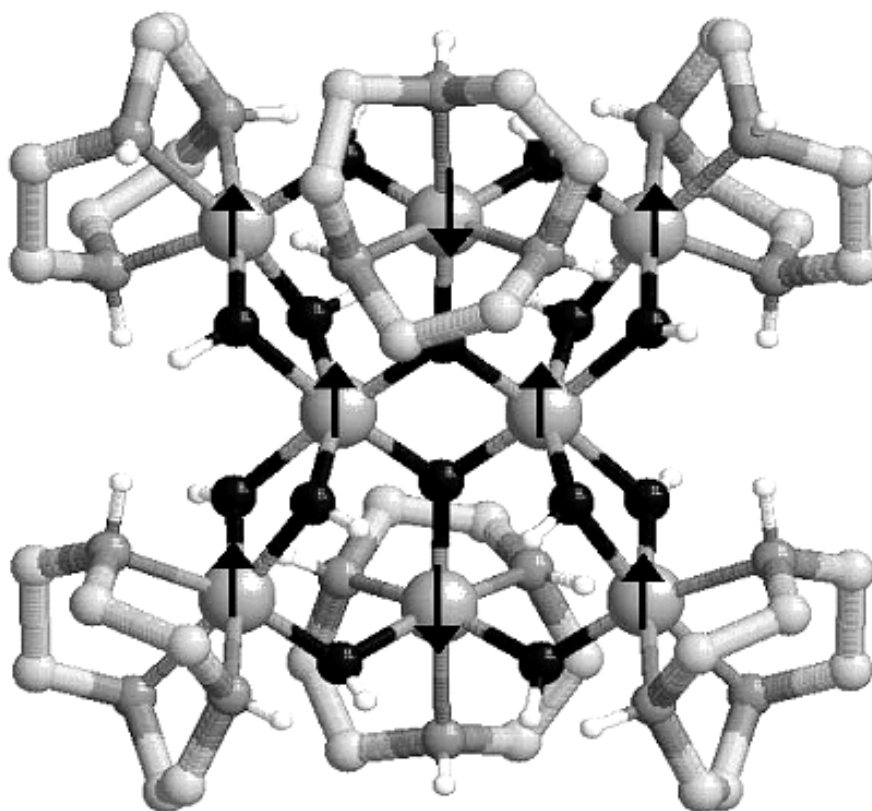


Figure 1.7: Structure of $[\text{Fe}_8\text{O}_2(\text{OH})_{12}(\text{tacn})_6]$ with rationalized spin alignments of the iron centers.

1.1.3.4. The largest iron SMM: A Compound containing $[\text{Fe}_{19}(\text{heidi})_{10}(\text{OH})_4\text{O}_6(\text{H}_2\text{O})_{12}]$, (Figure 1.8) which was made by Powell *et al.* in 1992, is the largest SMM of iron with largest ground spin state.¹⁴ This compound was found to co-crystallize with an Fe_{17} species. Subsequently it was possible to crystallize Fe_{19} species alone (using a substituted heidi ligand) and confirm that the spin state for Fe_{19} is $33/2$.¹⁵ In this compound, it can be seen that the multidentate ligand H_3heidi prevents the formation of an infinite array of $\text{Fe}(\text{OH})_3$. This $\text{Fe}_{19}/\text{Fe}_{17}$ pair has magnetic hysteresis at low temperature. Further EPR studies on this compound revealed the presence of intermolecular antiferromagnetic interactions between the cluster units.

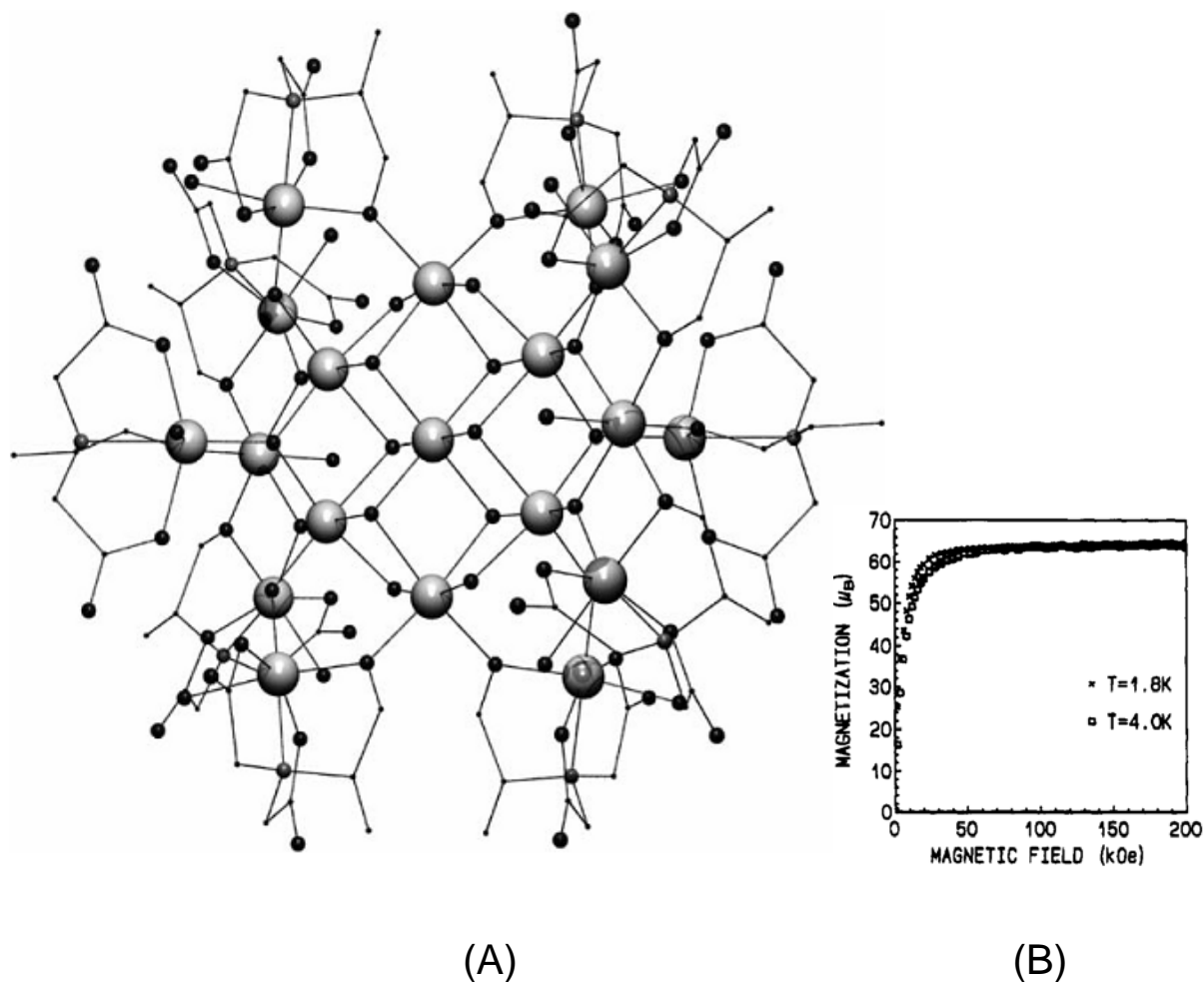


Figure 1.8: (A) Structure of the compound $[\text{Fe}_{19}(\text{heidi})_{10}(\text{OH})_4\text{O}_6(\text{H}_2\text{O})_{12}]^-$ and the (B) magnetization plots at different temperatures

1.1.3.4. The largest SMM: One way of increasing the nuclearity of transition metal clusters is the use of preformed clusters as the starting material. Following this way, a very big cluster of manganese (Figure 1.9) was synthesized by Tasiopoulos *et al.*¹⁶ In this case, using $\text{Mn}_{12}\text{-ac}$ as the starting material, the compound $[\text{Mn}_{84}\text{O}_{72}(\text{O}_2\text{CMe})_{78}(\text{OMe})_{24}(\text{OH})_6(\text{MeOH})_{12}(\text{H}_2\text{O})_{42}]$ (Figure 1.9) was synthesized. The structure consists of a series of Mn_4O_4 cubanes and Mn_3O triangles linked together to form a giant “wheel” or “torus”. Magnetic studies on Mn_{84} indicate a relatively small spin ground state of $S = 6$, but low temperature micro-SQUID measurements confirm the presence of temperature dependent hysteresis loops. This compound is so far the largest SMM made with a diameter of about 4.2 nm.

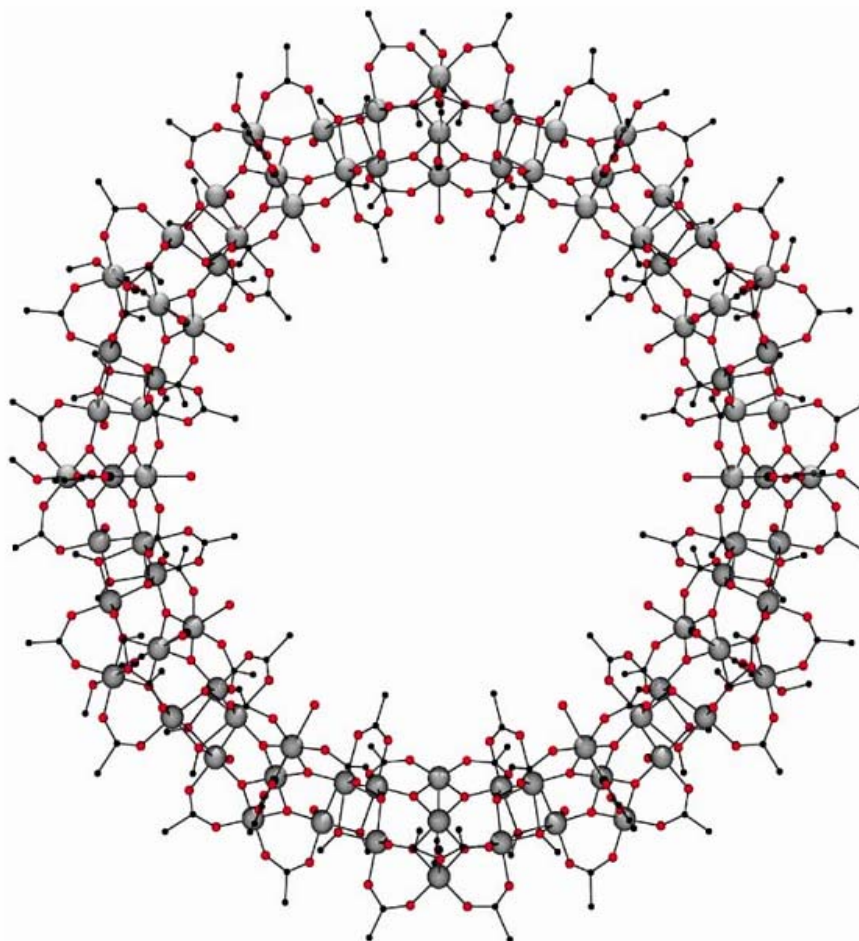


Figure 1.9: Structure of the wheel-shaped compound $[\text{Mn}_{84}\text{O}_{72}(\text{O}_2\text{CMe})_{78}(\text{OMe})_{24}(\text{OH})_6(\text{MeOH})_{12}(\text{H}_2\text{O})_{42}]$. The black, grey and red spheres represent the C, Mn and oxygen atoms, respectively.

1.2. Biomineralization: Biologically controlled growth of minerals

1.2.1. Basic ideas: Mineralization means the formation of inorganic salts. Biomineralization is the formation of inorganic salts by biological organisms.¹⁷ This can be for a variety of purposes, such as providing mechanical strength to bones (calcium phosphate), helping to navigate magnetotactic bacteria (Fe_3O_4), and storing iron (ferritin). There are two biologically distinct biomineralization processes, biologically induced mineralization and biologically controlled mineralization. In the first process, the organism modifies the local environment creating conditions

suitable for chemical precipitation. This process is uncontrolled and irreproducible. This kind of process can be found in pathological mineralization, such as in the formation of kidney and biliary stones and in the deposition of minerals by bacteria. In contrast, biologically controlled mineralization is a well-regulated process that occurs in specific biological sites, such as in bones and teeth. Two main steps are involved in this process: absorption of specific elements from the environment and then the the formation of biominerals in a controlled way. The most important part of the biologically controlled mineralization process is a preformed macromolecular organic matrix which takes part in the mineralization process.¹⁸ Its incorporation provides specific properties like strength to an organism. These kinds of macromolecular organic matrices are found in bones, shells and plants as collagen, chitin and cellulose, respectively. It is of relevance and interest to find a method to mimic natural biomineralization processes and to apply that knowledge in producing materials with novel functionalities. The most common biominerals are calcium carbonate, calcium phosphate and silica. Among these, calcium carbonate is the most abundant and familiar biomineral found in biological systems. It can be found in a number of different forms including amorphous calcium carbonate (ACC), calcite, aragonite and vaterite. ACC is very unstable, and among the three other crystalline polymorphs, calcite is most stable followed by aragonite and vaterite. Many biological systems, such as mollusks,¹⁹ echinoderms,²⁰ corals,²¹ certain algae,²² bird eggs, human ear¹⁸ and other,²³ form their hard parts using calcite and aragonite. Recently, however, studies suggest that in most of the cases of calcium carbonate biomineralization, ACC acts as a precursor to the other polymorphs. This was observed in the formation of the larva of the sea urchin, mollusc shells and corals.^{24, 25} According to Meldrum, this phase is easy to overlook when present in combination with crystalline phases, so it may be more common than is currently believed.²⁶ Figure 1.10 shows some structures of calcium carbonate biominerals.

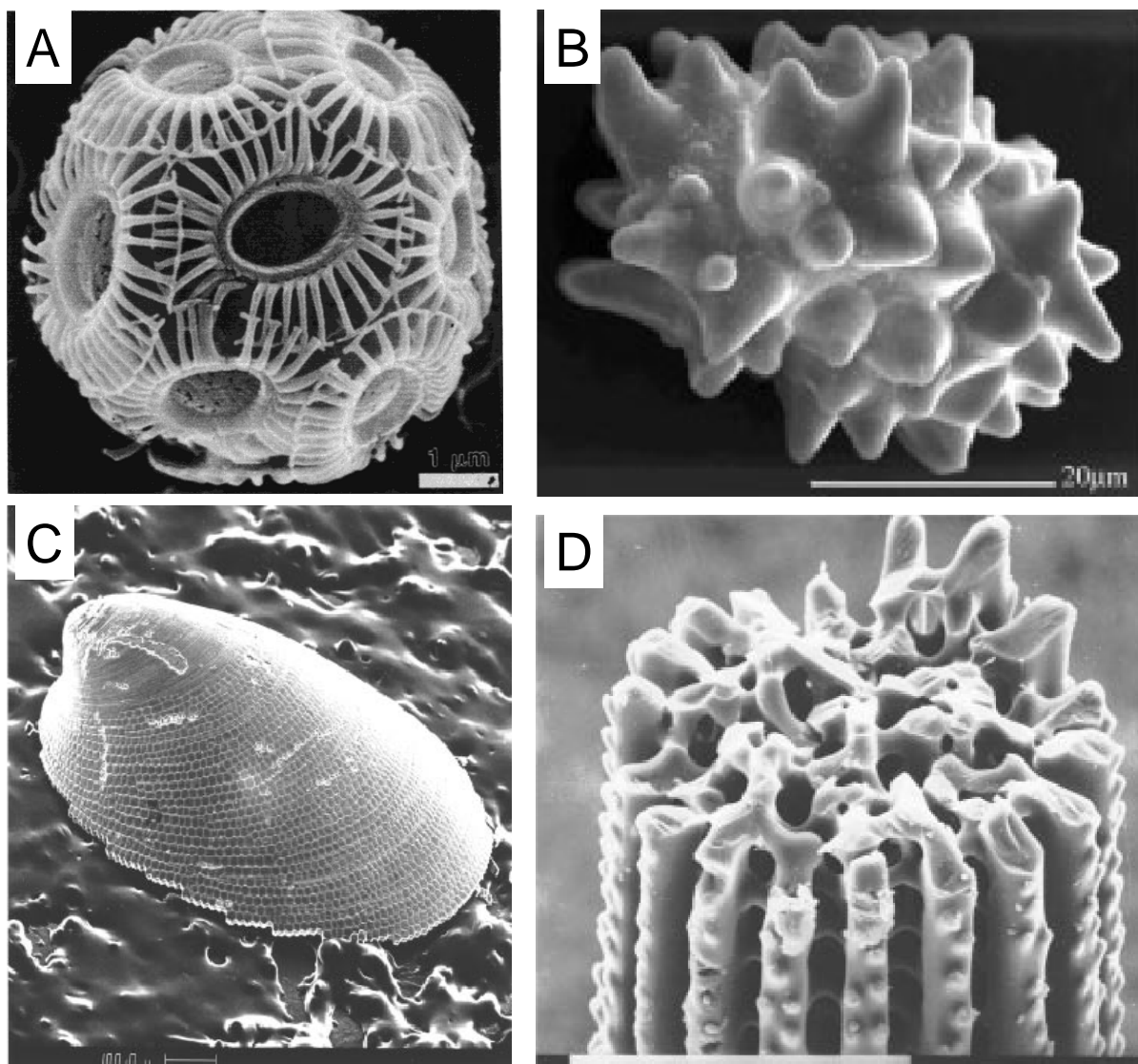


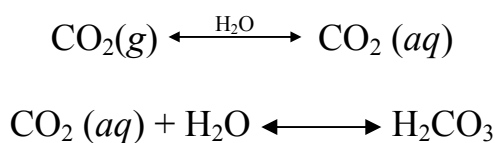
Figure 1.10: Examples of natural biominerals. SEM image of a (A) coccosphere of *Emiliana huxleyi*, (B) cystolith from the leaves of *Ficus Microcarpa*, (C) shell of the primitive mollusc *Neopilina hyaline* and (D) fracture surfaces of immature spines of the sea urchin *Paracentrotus lividus*.

1.2.2. Calcium carbonate mineralization

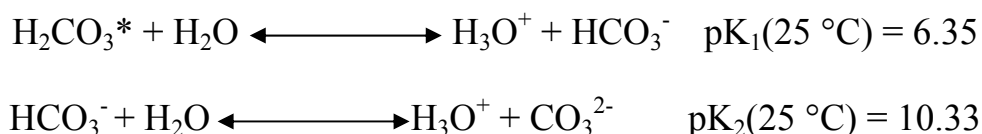
1.2.2.1. The ions involved: (a) **Calcium ion, Ca^{2+} :** Calcium was abundant in the igneous rocks when life originated on earth,²⁷ but it was unavailable for use by living organisms. As the earth cooled, various chemical and biological reactions started and, thus, calcium became the chemical basis of many compounds essential for life.²⁸ Calcium is an alkaline-earth element with the atomic number 20 and a radius of 0.99 Å.

Calcium was discovered in 1808, when Humphry Davy²⁹ isolated this element. Later on, Sydney Ringer first demonstrated the biological significance of calcium; for example, it plays a key role in egg fertilization³⁰ and in the development of bones, teeth and shells.³¹ Furthermore, calcium has been found to be involved in the conduction of nerve impulse³² to muscles, in the growth of plants³³ and in maintaining the cytoskeletal architecture of all cells.³⁴ Calcium also forms part of the biogeochemical compounds, which include carbonates (calcite, aragonite and vaterite), sulphates (gypsum), phosphates (apatite) and silicates. The wide-range of calcium's roles lies in the diverse chemistry of this element. Its chemical properties are similar to barium and strontium which can be substituted for Ca^{2+} ions, as can be observed in regulating enzyme activity.^{35, 36}

(b) Carbonate ion, CO_3^{2-} : The carbonate ion is an anion consisting of one central carbon atom surrounded by three identical oxygen atoms in a trigonal planar arrangement with a O–C–O bond angle of 120° . It can be formed by dissolving carbon dioxide in water. Carbon dioxide ($\text{CO}_2(\text{g})$) dissolves in water and further reacts with water forming carbonic acid³⁷, H_2CO_3 . Carbonic acid is a metastable intermediate.³⁸ Only a small amount of the dissolved $\text{CO}_2(\text{aq})$ exists as H_2CO_3 .



In aqueous solutions, carbonic acid is in equilibrium with hydrated carbon dioxide³⁹, H_2CO_3 and dissociates in two steps:



1.2.2.2. Morphology and polymorph selection in CaCO₃ mineralization: It is of particular interest to understand how nature selects some particular crystalline phase of CaCO₃ from the three available, to fulfill particular functionalities. Significant research efforts have been applied to mimic this process and to control the formed phase. The formation of a certain polymorph is kinetically controlled by changing the external parameters, such as temperature, pressure and also by adding organic and/or inorganic additives. Different kinds of unstable polymorphs have been stabilized in this way.

(a) Amorphous calcium carbonate: As mentioned earlier, ACC is the most unstable polymorph of CaCO₃ and readily transforms into one of the crystalline polymorphs, most commonly to calcite. It was also mentioned that this form plays a very important role as a precursor in the formation of most of the CaCO₃ biominerals. A detailed study of this phase, however, is difficult due to its short life time. Although many efforts have been made, few were successful in stabilizing this unstable ACC form. Incorporation of certain organic and inorganic additives can stabilize ACC. For example, Loste *et al.*, reported that incorporation of Mg within the ACC retards its transformation to crystalline polymorphs⁴⁰. Polyacrylic acid was also found to be efficient in stabilizing this amorphous phase by sequestering the Ca²⁺ ions.^{41, 42} The addition of EDTMP, ethylenediamine-*N,N,N',N'*-tetrakis(methylenephosphonic acid)^{43, 44}, phosphorus-containing compounds⁴⁵ or poly(propylenimine)-dendrimers⁴⁶ also retards the ACC transition. Donners *et al.* have reported that the use of an assembly of a poly(propylene imine) dendrimer together with a long chain hydrocarbon can stabilize ACC for 14 days⁴⁷. More recently, however, the stabilization was prolonged to 3 months by using phytic acid as an additive.⁴⁸

(b) Crystalline polymorphs:

The influence of temperature and pressure: It has been found that at low temperature ($T < 20\text{ }^{\circ}\text{C}$), calcite is the most dominant polymorph; however, at moderate temperature ($T = 40\text{-}50\text{ }^{\circ}\text{C}$), all three polymorphs form, and at higher temperature ($T > 60\text{ }^{\circ}\text{C}$), aragonite is the most dominant polymorph.⁴⁹ The effect of pressure has also been studied, and it has been found that calcite is the most dominant polymorph at low pressure whereas aragonite is dominant at higher pressure.

The effect of inorganic and organic additives: It has been realized following extensive research that the additives mostly take part in directing the polymorph selection by being adsorbed on some specific crystal face. In this way, they induce some specific character in the crystal growth pattern and thus control the evolved shapes.

The effect of inorganic additives: It has been found that the presence of alkali metal ions (Li^+ , Na^+ , K^+ , Rb^+) has considerable influence on the formation of calcite and aragonite. Inhibition of the transformation of aragonite to calcite was observed when the addition of alkali metal ions resulted in the substitution of a few calcium ions in aragonite.^{50, 51} The Li^+ ion has also been

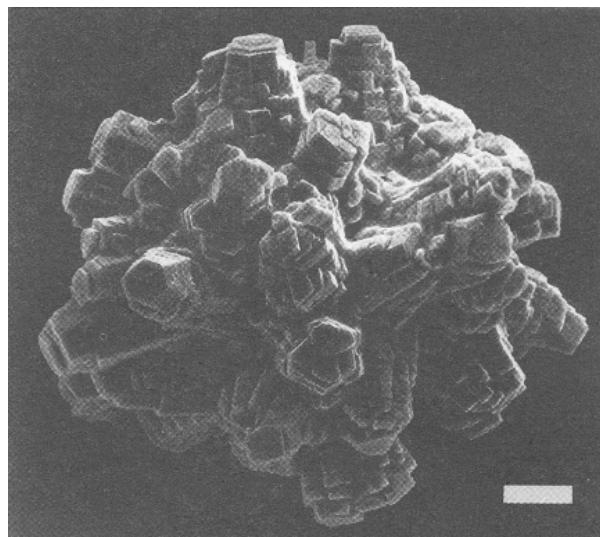


Figure 1.11: Scanning electron micrograph showing the expression of (001) tabular faces in aragonite crystals grown in the presence of Li^+ . Scale bar = $10\text{ }\mu\text{m}$.

reported to have a great influence on the polymorph selection of the CaCO_3 structures.⁵² A large amount of lithium ions, which are of small ionic radius, can be incorporated into calcite causing lattice distortion on the surface.⁵³ For example, Sims et al.⁵⁴ reported that the addition of lithium to a supersaturated calcium bicarbonate solutions results

in the preferential growth of the (001) faces of aragonite (Figure 1.11). The resulting morphology mimics the aragonite morphology observed in the nacreous shells of many molluscs. Polyvalent ions, such as Fe^{3+} , Cr^{3+} , Al^{3+} , or WO_4^{2-} , MoO_4^{2-} , PO_4^{2-} , have also been found to exert characteristic influences on the size and the type of polymorph.⁵⁵⁻⁵⁷

The effect of organic additives: Two main directions are being pursued when organic additives are applied in biomineralization of calcium carbonate.⁵⁸

In the first, the organic additives used are mostly rich in carboxylate groups which can replace some carbonate ions and bind to the Ca^{2+} ions. Because of this, they impart some specific structural properties in the evolved morphologies. Although the understanding of the control over morphology is still not well-understood at the molecular level, extensive research is going on in this field.⁵⁹ In the second case, to control the pattern of CaCO_3 deposition, some pre-designed substrates or conditions are imposed. For example, different kinds of templated substrates, such as self-assembled monolayers and Langmuir-films, have been used for patterned CaCO_3 deposition.

Various kinds of organic additives form a wide range of biomimetic calcium carbonate materials. For example, complex cake-like vaterite superstructures⁶⁰ composed of stacked porous multilayers have been reported to form in an ethanol/water mixed solution. Hexagonal vaterite mesocrystals have been synthesized in the presence of a *N*-trimethylammonium derivate of hydroxyethyl cellulose *via* aggregation-mediated mineralization.⁶¹ Double hydrophilic block copolymers⁶² with monophosphate ester have been used as a template for the precipitation of

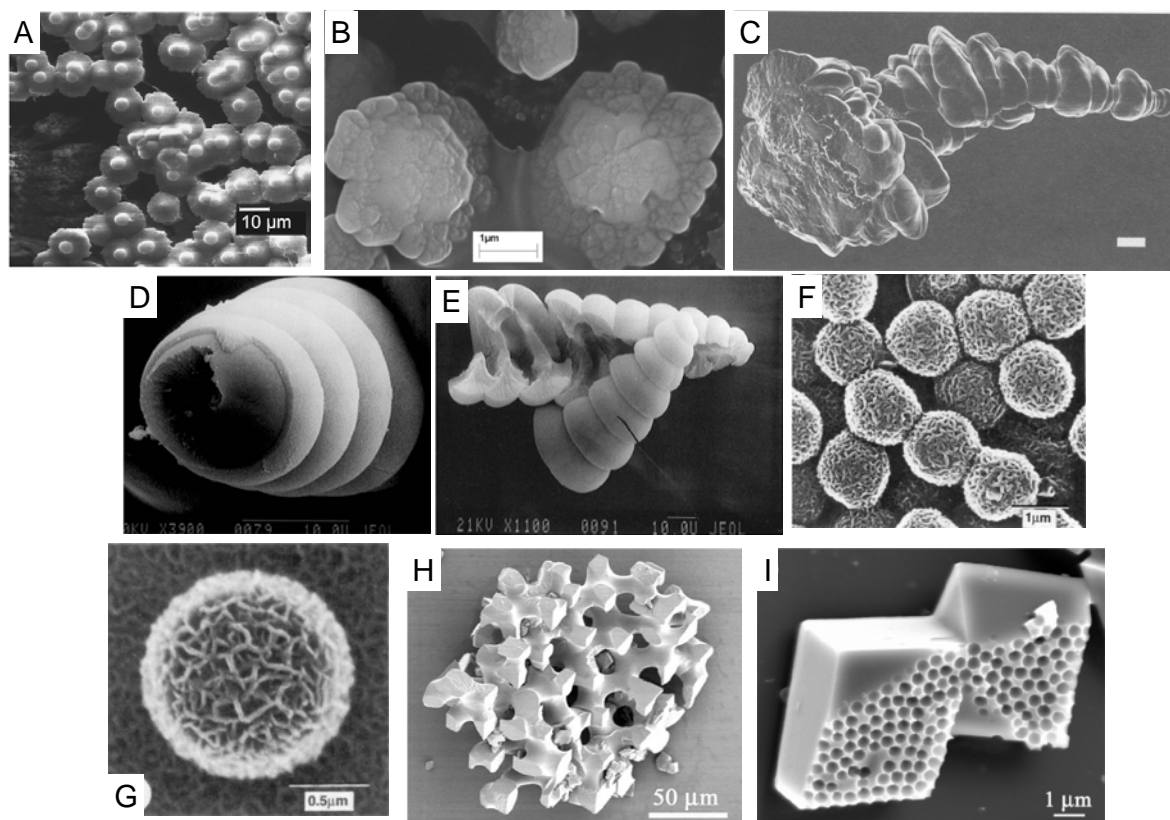


Figure 1.12: Various morphologies of calcium carbonate. (A) Complex CaCO_3 superstructure with block copolymers. (B) SEM image of vaterite flower-like shape. (C) SEM images showing helicoids outgrowth of stacked vaterite disks grown in the presence of linear poly α,β -aspartate. (D, E) Hollow helix fractured by micro-manipulation. (F) Cellular film of aragonite synthesized by using a biliquid foam as template. (G) Hollow spheres of aragonite with cellular substrate synthesized by using both a biliquid foam and microbeads as templates. (H) Templated single crystal of calcite precipitated in the polymeric replica of a sea urchin skeletal plate. (I) Calcite crystals grown on colloidal polystyrene monolayer after dissolution of polystyrene spheres, showing the crystal phase growing in contact with the monolayer.

complex superstructures (Figure 1.12 A) of calcium carbonate. Another example of a biomimetic structure is the flower-like vaterite structure (Figure 1.12 B), which was synthesized through a sonochemical process under higher acoustic amplitude.⁶³ Addition of charged poly(aspartate) to a supersaturated solution of calcium carbonate resulted in vaterite nucleation and the formation of helicoid morphologies (Figure 1.12 C-E).^{54, 64} Porous calcium carbonate in the form of aragonite has been prepared from oil-water-surfactant microemulsions supersaturated with calcium bicarbonate and magnesium chloride. The latter is added to promote the growth of the aragonite polymorph (Figure 1.12 F). Additionally, using micrometer-sized polystyrene beads as the substrate for a microemulsion, hollow spherical aggregates with cellular substructure, referred to as ‘biomimetic

cocoliths', are formed (Figure 1.12 G).⁶⁵ Single crystals of calcite with a sponge-like shape (Figure 1.12 H) have been produced either using a polymer membrane, which has an identical morphology to a sea urchin skeletal plate (Figure 1.12 I)^{66, 67} or by simple crystallization on colloidal monolayers of polystyrene and silica spheres.⁶⁸ The organic component acts as a morphology-modifier during the growth of calcium carbonate.

1.3. Thesis overview

The thesis is organized in the following ways. Chapter 3 describes the use of some polyol ligands to synthesize magnetically interesting transition metal (Mn and Fe) clusters. In Chapter 4, the synthesis and magnetic studies are discussed for a family of one dimensional chain of lanthanide chains. Chapter 5 describes the use of some ligands as template for controlled formation and growth of CaCO₃. In a more general way, it can be said that this thesis explains the use of the coordination chemistry to produce interesting structures using a broad range of elements in the periodic table. These are the transition metals (Chapter 3), the lanthanides (Chapter 4) and the alkaline earth metals (Chapter 5).

CHAPTER 2

Research objectives

The overarching aim in the research presented here was to use coordination chemistry principles to control aggregation process of metal ions. Two important areas, which are currently being intensely researched, were chosen. Firstly, controlled aggregation of paramagnetic metal ions to produce cooperatively coupled molecule-based magnets was studied. In Chapter 3, the potential ways of producing single-molecule magnets (SMMs) using polyols as ligands and manganese and iron ions as the paramagnetic centers were investigated. SMMs are molecules which can store magnetic information, which requires both uniaxial anisotropy and non-zero overall spin. In contrast to most Mn and Fe clusters reported in the literature, it was found that the polyols tend to favor the formation of regular polyhedral arrangements of the metal ions. In Chapter 4 one polyol was chosen in order to survey the properties of a family of lanthanide chain compounds. Here the aim was to discover whether single-chain magnets, SCMs, based on $4f$ metals could be produced. In order to produce the chains, benzoate was employed to provide bridges. The $4f$ metal ions were chosen because of their inherent spins and anisotropies. As is becoming increasingly clear from the literature, Dy^{III} seems to be the most promising choice for attaining exotic magnetic properties.

The second area of study chosen aimed to investigate the utility of using the sort of small ligand molecules usually employed in constructing coordination compounds to mimic biomineralization processes. Biominerals are minerals utilized by biological systems to fulfill a variety of functions, and thus can be described as functional materials. Their specific shapes, phases and functions result in the majority of cases through the interaction of complicated, templating biomolecules, such as polysaccharides or proteins, with the growing surfaces of the minerals. Most research aiming to reproduce the fascinating shapes and properties of such materials *in vitro* uses

correspondingly complicated templating molecules and systems, such as block copolymers, Langmuir-Blodgett films and inverse micelles. Previous research in our group using a simple polycarboxylate demonstrated that highly complex calcium carbonate structure could be produced such as micro-trumpets constructed from bundles of high-aspect ratio nanocrystallites. In Chapter 5 the formation of these structures was investigated further as well as the influence of some rigid polycarboxylates on calcium carbonate structures. In all cases, these additives appear to stabilize an initial phase of amorphous calcium carbonate which then evolves into one of the three crystalline phases of calcium carbonate in a range of topologies.

CHAPTER 3

High-nuclearity aggregates of manganese and iron using polyols: Clusters with polyhedral cores

General Introduction

The first evidence of a single-molecule magnet (SMM) was found in the early 1990s with the discovery of slow relaxation of magnetization at low temperatures in a mixed-valent Mn_{12} cluster.⁶⁹ It has been observed that this molecule can be magnetized at 2 K by applying a magnetic field, and that 40% of the magnetization is retained even after 2 months, if it is kept at the same temperature.⁷⁰ This fact encouraged the idea of using single-molecule magnets in magnetic data storage.^{71, 72} According to this concept, a single molecule can act like a bulk-magnet showing magnetic hysteresis with an energy barrier ΔE (or U_{eff}) for the spin reversal. This energy is proportional to $S_T^2|D|$ (for integer spin) or $(S_T^2 - 1/4)|D|$ (for half-integer spin).⁶ As a result of this energy barrier for the spin reversal, such a single molecule can be used to store a byte of data, and thus the smallest magnetic devices for data storage may be built. Since the discovery of this fact, huge efforts⁷³⁻⁷⁶ have been made to increase the ground spin state (S) and the zero-field splitting parameter (D) to obtain better energy barriers, and thus better SMMs.

Compared to other transition metal clusters, manganese clusters often possess higher ground state spin values.⁷⁷⁻⁸⁰ Moreover, the inherent Jahn-Teller deformation in Mn^{III} complexes makes this transition metal a favorable choice for synthesizing SMMs by inducing uniaxial anisotropy in the compound. Although there are many high-nuclearity manganese clusters reported to date, much more investigation is required to synthesize SMMs which can be used for practical applications.⁶ In the hope of improving the ground spin state (S) and magnetic anisotropy of the molecular clusters, research efforts have targeted the synthesis of high-nuclearity, mixed-valance manganese clusters

via self-assembly techniques. Although different kinds of ligands have been used in the synthesis of high-nuclearity manganese clusters, it has been observed that alkoxy ligands are very efficient in producing a variety of high-nuclearity manganese clusters because they can make different kinds of bridges between the metal centers.^{9, 81-83} To expand upon these investigations, several new poly-alkoxy ligands were introduced for the synthesis of polynuclear manganese and iron clusters. Special attention was paid in selecting the ligands (Figure 3.1) to ensure that the ligands are flexible, multi-dentate and capable of forming μ -oxo bridges between different metal centers. It was found that these ligands are appropriate candidates for the synthesis of polynuclear transition-metal clusters.

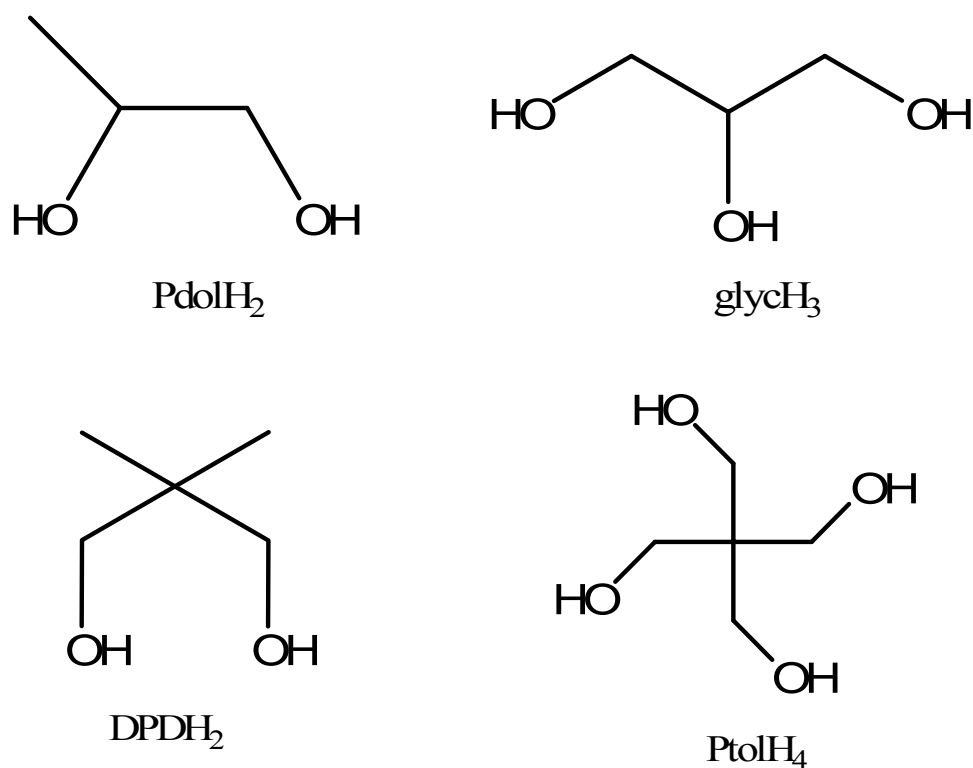


Figure 3.1: Poly-alkoxy ligands used in the synthesis of manganese and iron clusters. PdolH₂, glycH₃, DPPH₂, and PtolH₄ represent Propan-1,2-diol, propan-1,2,3-triol (glycerol), 2,2-dimethyl propane-1,3-diol, and 2,2-di(methyl hydroxyl) propane-1,3-diol (pentaerythritol).

3.1. A hexanuclear manganese cluster, [(PtolH)₄(O₂CMe)₆(μ₆-O)Mn^{III}₆]**·1.5en**, **3.1**, showing SMM behavior

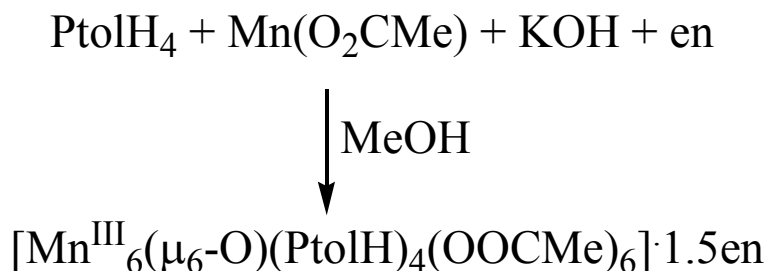
3.1.1. Introduction

Although many hexanuclear manganese complexes are reported to date, only a few of those behave like a single-molecule magnet.¹⁰ Pentaerythritol (PtolH₄) is a poly-alkoxy ligand containing four alcohol groups. The flexibility and proximity of the alkoxy arms (Figure 3.1) are in favor of forming μ-oxo bridges connecting multiple metal ions. With this in mind, PtolH₄ was used to synthesize a high-nuclearity manganese cluster. Although this ligand, having four potential coordinating alkoxy groups, has already been used in synthesizing manganese clusters,⁸⁴ the new hexanuclear Mn^{III} cluster [(PtolH)₄(O₂CMe)₆(μ₆-O)Mn^{III}₆]**·1.5en** (**3.1**, en = ethylenediamine) was synthesized during the course of this study.

3.1.2. Results and discussion

3.1.2.1. Description of the structure: The reaction of Mn(O₂CCH₃)₂·4H₂O, pentaerythritol (PtolH₄), ethylenediamine and KOH in methanol, resulted in a dark brown solution from which black-brown, rectangular crystals of [(PtolH)₄(O₂CMe)₆(μ₆-O)Mn^{III}₆]**·1.5en**, **3.1** (see Scheme 3.1) were isolated in 42% of yield. Manganese(II) acetate was used as the source of Mn. Since Mn^{III} is more magnetically desirable, due to the presence of the Jahn-Teller distortion, the Mn^{II} starting material was oxidized and stabilized by adding KOH and ethylenediamine to the reaction mixture. Addition of the bases also favored the deprotonation of PtolH₄. Single-crystal X-ray diffraction revealed six manganese centers in each molecule of compound **3.1** (Figure 3.2A).⁸⁵ Based on bond valence sum calculations and from the presence of Jahn-Teller distortions, all the manganese centers were found to be trivalent.⁸⁶ All metal ions are six-coordinate with nearly octahedral coordination geometries. The compound crystallizes in the triclinic space group *P* $\bar{1}$. From the

crystal structure, it can be seen that the core of the Mn₆ cluster consists of six Mn^{III} ions, twelve μ₂-O (from four ptolH), six acetates and one μ₆-oxo group. The six Mn^{III} ions can be described as defining the six vertices of an octahedron. A central μ₆-O²⁻ group bridges the six Mn^{III} ions. With three of the possible four alcohol groups, each PtolH³⁻ coordinates to three different



Scheme 3.1: Synthesis of compound **3.1** is shown. PtolH₄ and en represent pentaerythritol and ethylenediamine, respectively.

Mn^{III} ions (Figure 3.2C). In this way, each PtolH³⁻ ligand caps alternating triangular faces of the Mn₆ octahedron. Each acetate group is coordinated to one Mn^{III} ion and acts as a terminal ligand. Surprisingly it was found that among the all six Jahn-Teller axes, five are directed towards the central μ₆-oxo group, whereas one (Mn8) is along a different direction which is parallel to other two (Mn7, Mn12) J-T axes. The packing diagram of **3.1** is shown in Figure 3.2D. It can be seen that the clusters are separated from each other. The ethylenediamine molecules play a vital role in the packing pattern by making hydrogen bonds between the alkoxy and acetate oxygen atoms and the amine hydrogen atoms. As a result, the ethylenediamine molecules link the isolated Mn₆ cluster units. The presence of a strong hydrogen bond was also evident from the presence of a very broad and strong band in the infrared spectrum around 3300 cm⁻¹.

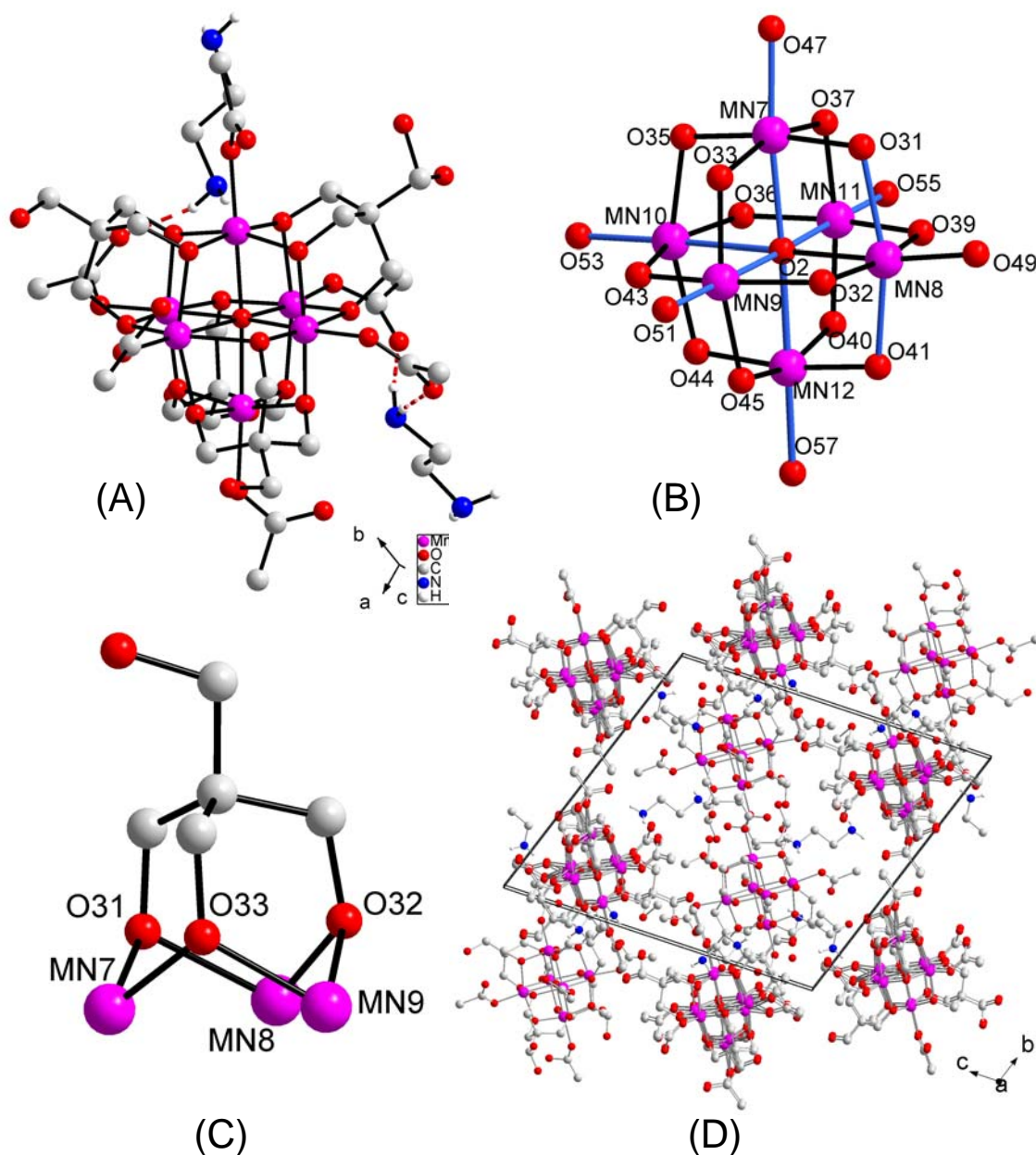


Figure 3.2: (A) Molecular view of **3.1**. (B) Presentation of the Jahn-Teller axes for all the six MnIII ions shown in blue color. (C) Coordination mode of the ptolH ligands and (D) packing diagram for compound **3.1**. Blue, gray, purple, and red spheres represent N, C, Mn, and O atoms, respectively. Red dotted lines in (A) show the presence of hydrogen bonding between hydroxyl and carboxyl oxygen atoms and the hydrogen atoms from the neighboring ethylenediamine molecules.

3.1.2.2. Magnetic properties: The temperature dependence of the susceptibility was measured for compound **3.1** (Figure 3.3A). From the χT versus T plot it can be seen that the χT value at room temperature is $15.45 \text{ cm}^3\text{K/mol}$ which is slightly less than the expected value of 18

$\text{cm}^3\text{K/mol}$ calculated for six isolated Mn^{III} ions. This observation suggests the presence of dominant antiferromagnetic coupling between the Mn^{III} centers. This can also be rationalized from the

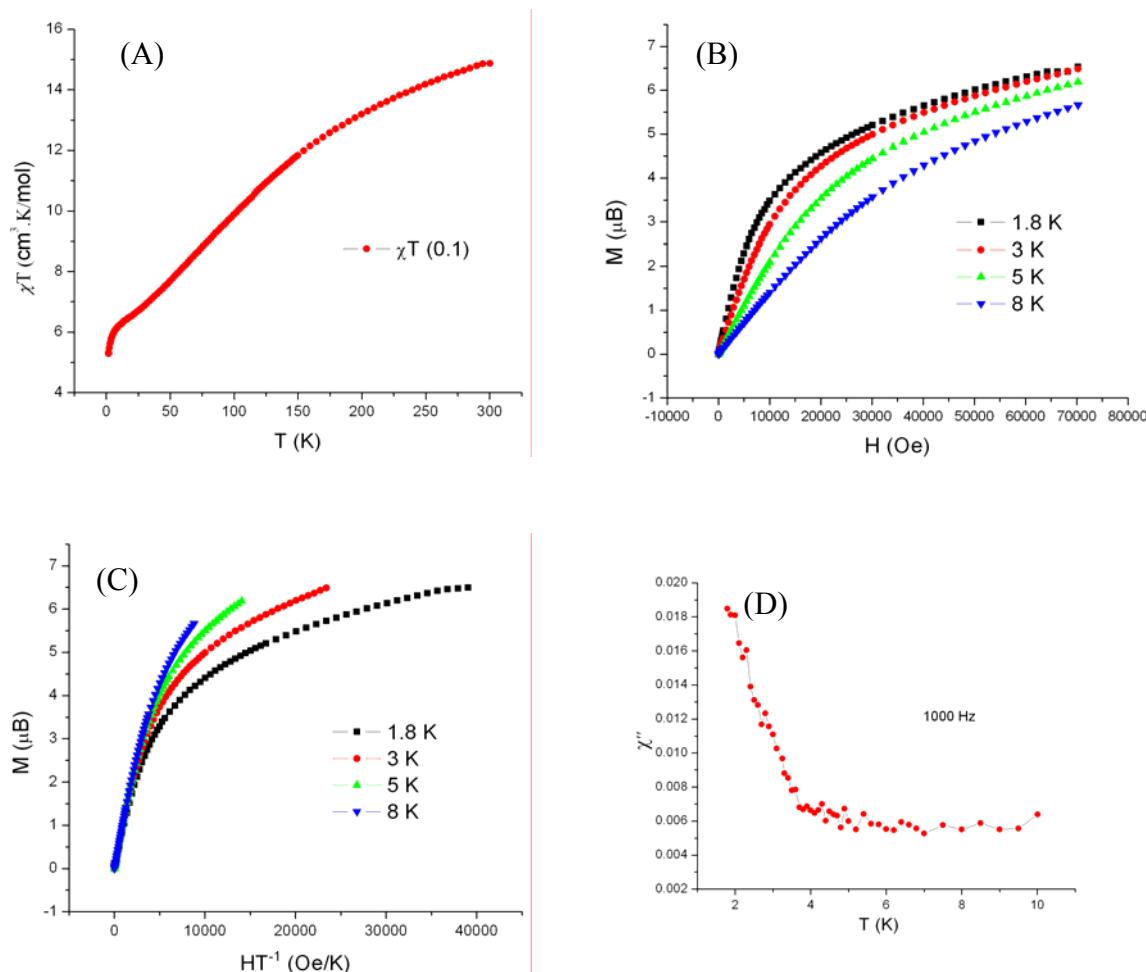


Figure 3.3: Magnetic data for **3.1**. The χT versus T plot is shown (A) at an applied field of 1000 Oe. The magnetization plot at different temperatures is shown (B). The M versus H/T plot is shown (C). The non-overlapping character of the curves found at different temperatures indicates the presence of magnetic anisotropy in the structure. The χ'' vs. T plot shows a peak around 2 K (D).

structural point of view. All the $\text{Mn}^{\text{III}}\text{-O-Mn}^{\text{III}}$ angles around the central $\mu_6\text{-O}^{2-}$ are close to 90° , whereas all the $\text{Mn}^{\text{III}}\text{-O-Mn}^{\text{III}}$ angles around the other alkoxy-oxygen atoms are close to 105° . The first type of oxo-bridging favors ferromagnetic coupling, whereas the latter type often induces antiferromagnetic coupling between metal centers.^{87, 88} In compound **3.1**, the latter type of bridging dominates, and as a result, the cluster shows overall antiferromagnetic behavior. The magnetization

was measured within an applied magnetic field range of 0 Oe to 70000 Oe at various temperatures (Figure 3.3B). At a very low temperature (1.8 K) and high field (70000 Oe), the magnetization reaches a value of about $6.5 \mu_B$ with a slight slope at the higher end of the curve. This kind of behavior often indicates the presence of magnetic anisotropy in a compound. To justify this point, magnetization data were collected at different temperatures. The non-superimposable character of the M versus H/T data sets (Figure 3.3C) supports the presence of magnetic anisotropy. The presence of intermolecular interaction cannot be totally neglected as a possible origin of this anisotropy. An ac-susceptibility measurement was carried out, and an out of phase signal was found near 2 K (Figure 3.3D). Further low-temperature study of this compound may reveal interesting properties like single molecular magnetic behavior.

3.2. Structure and magnetic properties of a Mn_{17} cluster compound $[Mn^{III}_{11}Mn^{II}_6(\mu_4-O)_8(\mu_3-Cl)_4(\mu_5-O_2CMe)_2(DPD)_{10}Cl_{2.34}(O_2CMe)_{0.66}(py)_3(MeCN)_2] \cdot 7MeCN$, 3.2

3.2.1. Introduction

Although there are many examples of mixed-valance Mn^{II}/Mn^{III} clusters, and the Mn^{III} centers induce a local anisotropy through Jahn-Teller distortions, only a few clusters possess a resultant anisotropy. This is because in most of the compounds, the Jahn-Teller axes cancel each other out due to the molecular symmetry. For example, it has been observed that a Mn_{10} “supertetrahedron”, which is composed of a $Mn^{II}_4Mn^{III}_6$ core and possesses a ground state spin of $S_T = 22$, has no significant anisotropy.⁸⁹ More recently, a Mn_{19} cluster complex, which derives from two such tetrahedral units sharing a vertex, has a record ground spin state of $^{83}/_2$, also not shows any significant anisotropy.⁹

In the previous section and in the literature, it had been observed that poly-alkoxy ligands are very efficient in synthesizing high-nuclearity manganese clusters *via* a self-assembly process. When 2,2-dimethyl-1,3-propanediol (DPDH₂) was used in the self-assembly of manganese metal ions, a mixed-valence Mn₁₇ cluster with a molecular formula of [Mn^{III}₁₁Mn^{II}₆(μ₄-O)₈(μ₃-Cl)₄(μ₅-O₂CMe)₂(DPD)₁₀Cl_{2.34}(O₂CMe)_{0.66}(py)₃(MeCN)₂]₇MeCN, **3.2**, with a ground state spin of $S_T = 28 \pm 1$, was obtained. As in Mn₁₉, the cluster contains two tetrahedral Mn₁₀ units, which share an edge. Investigating the magnetic properties of this compound was of interest because it allowed a comparison with the other clusters containing the Mn₁₀ unit.

3.2.2. Results and discussion

3.2.2.1. Description of the structure: The reaction of MnCl₂·4H₂O, 2,2-dimethyl-1,3-propanediol (DPDH₂), sodium acetate and pyridine in acetonitrile, resulted in a light brown solution from which reddish-brown, rod-shaped crystals of **3.2** were isolated. Single-crystal X-ray diffraction revealed 17 manganese centers in each molecule of compound **3.2** (Figure 3.4). Based on bond valence sum calculations, 11 manganese centers were found to be trivalent, while the remaining six are divalent.⁸⁶ All metal ions are six-coordinate with octahedral coordination geometries.

The core of the complex can be described as two edge-sharing Mn^{II}₄Mn^{III}₆ tetrahedra in which a Mn^{II} ion is located at each vertex resulting in edge lengths between 6.4 and 6.6 Å (Figure 3.5). At the center of each edge is a Mn^{III} ion positioned such that the ∠Mn^{II}-Mn^{III}-Mn^{II} is nearly linear (173.8-178.8°). With the exception of the shared edge, each set of manganese ions are linked by two μ₂-alkoxo bridges originating from one DPD²⁻ ligand. Two different types of faces exist for the tetrahedra: the four faces adjacent to the shared edge (**X**) and the remaining four faces (**Y**) (Figure 3.5A). The five Mn^{III} ions that are present on two adjoining **X** faces are coordinated to an acetate ligand *via* one μ₃-O and one μ₂-O bridge. As a result, the two tetrahedra are linked not only by their

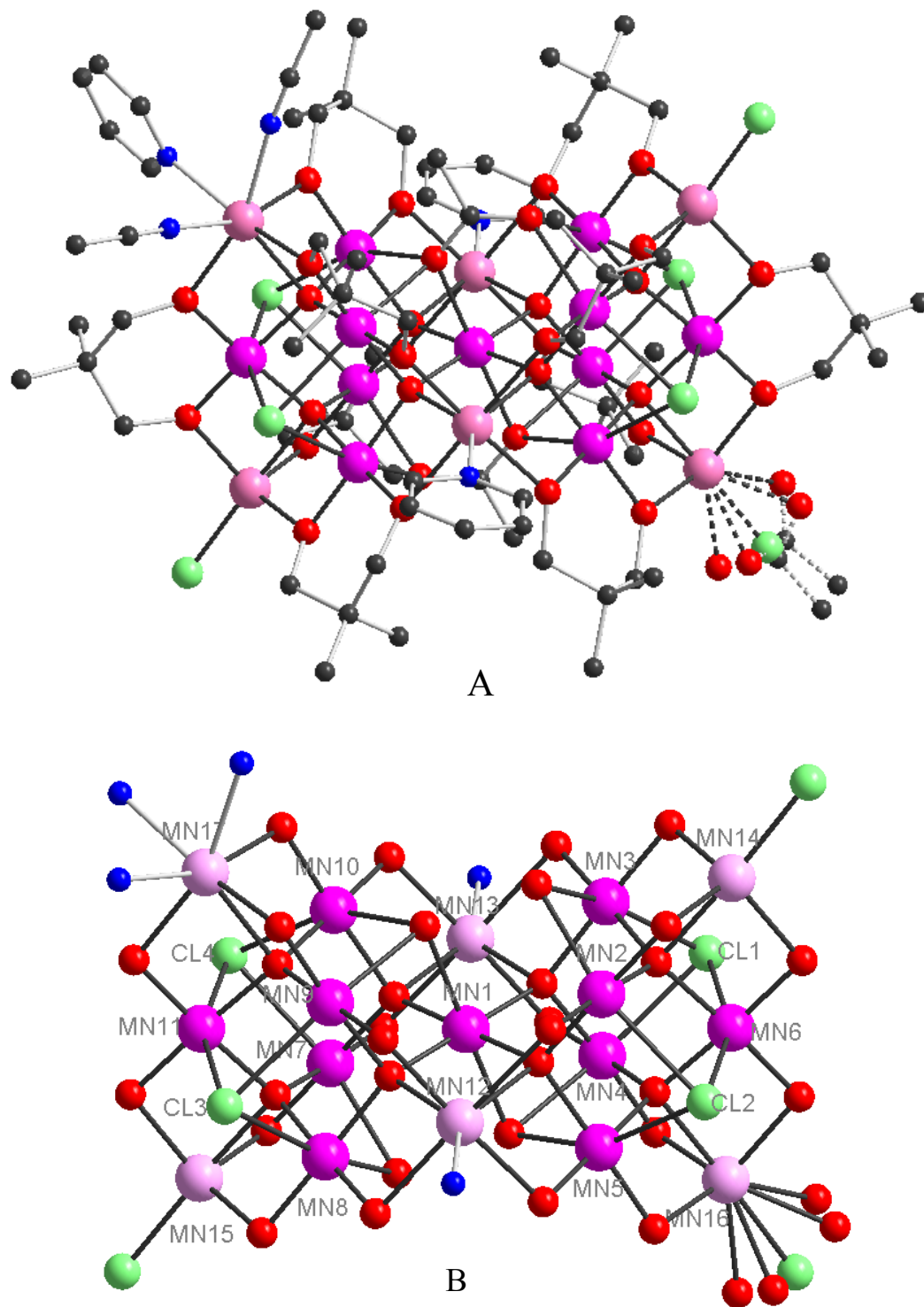


Figure 3.4: The structure of $[\text{Mn}^{\text{III}}_{11}\text{Mn}^{\text{II}}_6(\mu_4\text{-O})_8(\mu_3\text{-Cl})_4(\mu_5\text{-O}_2\text{CMe})_2(\text{DPD})_{10}\text{Cl}_{2.34}(\text{O}_2\text{CMe})_{0.66}(\text{py})_3(\text{MeCN})_2]\cdot 7\text{MeCN}$ in **3.2** (A) and a view of its core, presented with only the Mn-coordinated atoms (B). Dark purple, light purple, green, red, black, and blue spheres represent Mn^{III}, Mn^{II}, Cl, O, C and N atoms, respectively. Hydrogen atoms are omitted for clarity.

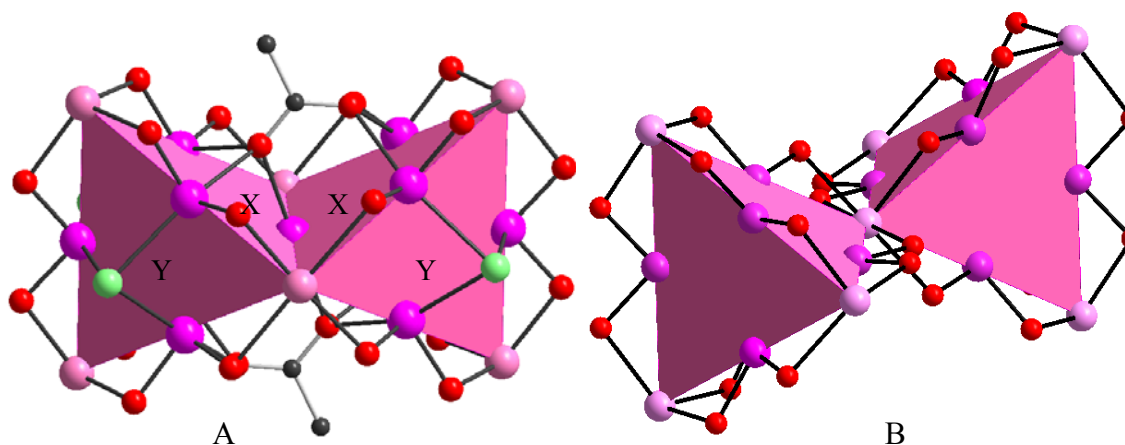


Figure 3.5: Polyhedral representations of the cores of the Mn_{17} cluster of **3.2** (A) and the Mn_{19} (B) clusters¹⁴ illustrating the edge-sharing and corner-sharing tetrahedra. Dark purple, light purple, green, and red spheres represent Mn^{III} , Mn^{II} , Cl, and O atoms, respectively. In Figure (A), X and Y represent the two kinds of faces.

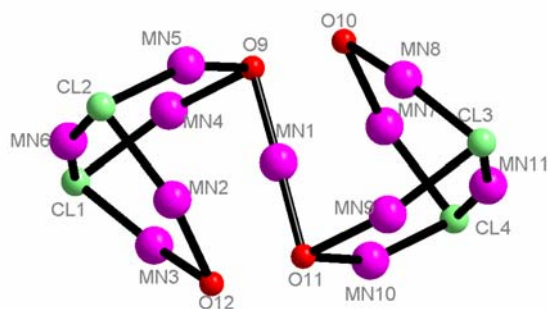


Figure 3.6: The Jahn-Teller elongations are shown along corresponding Mn^{III} -X (X= O or Cl) bonds. All other atoms and bonds are excluded for clarity. The nearly orthogonal (angles within the range of 73.34° to 88.67°) Jahn-Teller axes can be clearly seen in the picture.

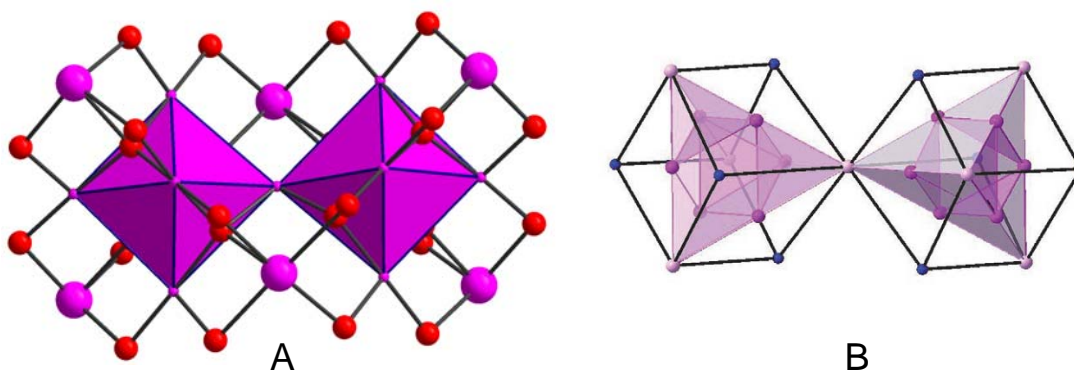


Figure 3.7: Polyhedral representation of octahedral Mn^{III}_6 units in compound **3.2** (A) and in Mn_{19} cluster. (B).

shared edge, but also *via* the acetate ligands. Just above each **Y** face, a μ_3 -bridging chloride ion caps three Mn^{III} ions. From within each tetrahedral unit, the Mn^{II} and Mn^{III} centers are further held together by one μ_3 -bridging and two μ_4 -bridging oxo ligands. The remaining chloride, acetate, pyridine, and acetonitrile ligands, are terminally bound to the Mn^{II} centers. In the previously reported (Mn_{19}) complex, $[\text{Mn}^{\text{III}}_{12}\text{Mn}^{\text{II}}_7(\mu_4\text{-O})_8(\mu_3, \eta^1\text{-N}_3)_8(\text{HL})_{12}(\text{MeCN})_6]\text{Cl}_2 \cdot 10\text{MeOH} \cdot \text{MeCN}$ where H_3L is 2,6-bis(hydroxymethyl)-4-methylphenol, the two tetrahedra share a vertex (Figure 3.5B), whereas in **3.2** two such tetrahedra share an edge.⁹ At this point it can be noted that in the previous section, compound **3.1** contains a Mn^{III}_6 octahedra which is quite similar to the octahedra made by six Mn^{III} in **3.2**. The Jahn-Teller axes in **3.2** are shown in Figure 3.6. Thus, among the eleven Jahn-Teller axes, ten are directed towards the four Cl^- ions and are nearly orthogonal to each other leaving one Jahn-Teller axis through the central Mn^{III} ion different from others. This aspect leads to an overall magnetic anisotropy in the structure.

3.2.2.2. Magnetic properties. Magnetic measurements were performed on a polycrystalline sample maintained in its mother liquor in order to avoid any solvent loss or decomposition of the compound. At room temperature, the χT product is $61.0 \text{ cm}^3 \cdot \text{K} \cdot \text{mol}^{-1}$ (Figure 3.8) which is slightly higher in comparison to the expected value ($59.25 \text{ cm}^3 \cdot \text{K} \cdot \text{mol}^{-1}$ with $g_{\text{av}} = 2$) for eleven Mn^{III} ($S = 2$) and six Mn^{II} ($S = 5/2$) isolated metal centers. Upon decreasing the temperature, the χT product at 500 Oe increases to a maximum of approximately $390 \text{ cm}^3 \cdot \text{K} \cdot \text{mol}^{-1}$ at 11 K before a final decrease down to $219 \text{ cm}^3 \cdot \text{K} \cdot \text{mol}^{-1}$ at 1.8 K. The initial increase of χT with decreasing temperature clearly indicates that dominating ferromagnetic interactions are present in **3.2**, which has been similarly observed for other previously reported related systems.^{9, 89} The decrease of the χT product below 11 K, suggests that additional effects such as intermolecular antiferromagnetic interactions and/or zero-field splitting (ZFS) are present.

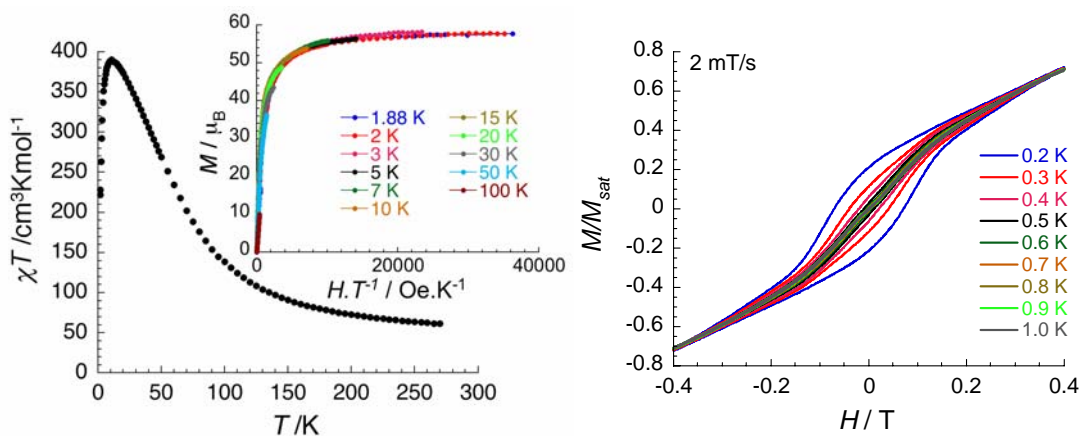


Figure 3.8: (A) Temperature dependence of the χT product of **1** (where $\chi = M/H$) measured in $H_{\text{dc}} = 500$ Oe; (inset) M versus H/T plot from 1.8 K to 100 K. (B) Field hysteresis loops of the normalized magnetization at a field scan rate of 2 mT/s in the temperature range 1-0.2 K for a single crystal of complex **3.2** oriented in its easy direction of magnetization. The magnetization has been normalized to the saturation value at 1.4 T.

At 1.8 K and 7 T, the magnetization increases very fast with increasing field, and it is almost saturated near $58 \mu_B$ (inset Figure 3.8A). Only a slight residual slope is observed at high field for the M versus H data, suggesting the presence of small magnetic anisotropy in the complex, which is expected due to the Mn^{III} metal ions present. When the magnetization is plotted against H/T at various temperatures (inset Figure 3.8A), however, the nearly superimposed curves confirm that the anisotropy is weak in **3.2**. Attempts to fit the M versus H/T data with Brillouin functions, even after introducing S_T and D as adjustable parameters, were unsuccessful probably due to the presence of intermolecular magnetic interactions. Considering the near-saturation of the magnetization at $58 \mu_B$, a ground state spin of $S_T = 29$ can be expected with a g -value near 2. This can be rationalized by a situation in which the spins of two Mn^{III} ions are antiparallel to all Mn^{II} ions and the remaining nine Mn^{III} ions. Extrapolating the χT value to very low temperatures where only the ground state would be expected to be populated, provides an experimental value close to $400 \text{ cm}^3 \cdot \text{K/mol}$, which in turn suggests a slightly lower spin ground state nearer to $S_T = 28$ ($406 \text{ cm}^3 \cdot \text{K/mol}$ with $g_{\text{av}} = 2.00$). This low observed value may be due to some intermolecular interactions as has been observed for an Fe_{19} compound where theoretically $S = 35/2$, however intermolecular interaction lower the value to

$^{33}/_2$. Since this is only an estimate, a ground state spin of $S_T = 27$ may also be possible (378 $\text{cm}^3\cdot\text{K}/\text{mol}$ with $g_{\text{av}} = 2.00$) and would result from a situation where the spins of two Mn^{II} are antiparallel to the spins of all of the Mn^{III} ions and the remaining four Mn^{II} ions. Although the spin ground state of **3.2** is not precisely determined yet, measurements clearly indicate a spin value of $S_T = 28 \pm 1$, which is quantitatively in agreement with both the low temperature χT product and the magnetization saturation value obtained from the M versus H data.

In hope of obtaining more information regarding the nature of the anisotropy, the field dependence of magnetization of **3.2** was studied below 1.8 K using a micro-SQUID.⁹⁰ Below 1 K, magnetic hysteresis (*i.e.* slow relaxation of the magnetization) was observed and the coercivity was found to be approximately 1500 Oe at 0.2 K (Figure 3.8B). Although the hysteresis could arise from either magnetic anisotropy and/or intermolecular interactions, it is likely that magnetic anisotropy results from from the non compensated J-T distortions as discussed earlier (Section 3.2.2.1).

3.3. A three dimensional network: $[\{\text{Mn}^{\text{III}}_{12}\text{Mn}^{\text{II}}_9(\mu_4\text{-O})_8(\text{glycH})_{12}(\mu\text{-1,1-N}_3)_6(\text{OH}_2)_6(\text{N}_3)_{1.5}\}\{\text{Mn}^{\text{II}}(\mu\text{-1,3-N}_3)_{4.5}(\text{OH}_2)_{1.5}\}]\text{Cl}_4\cdot\text{ca.7.5H}_2\text{O}$, **3.3**

3.3.1. Introduction

In the course of investigations into the synthesis of high-spin $\text{Mn}^{\text{II}}/\text{Mn}^{\text{III}}$ clusters, it was found that using propan-1,2,3-triol (glycH_3 ; glycerol) as a ligand with azide as coligand led to the formation of a manganese cluster $[\{\text{Mn}^{\text{III}}_{12}\text{Mn}^{\text{II}}_9(\mu_4\text{-O})_8(\text{glycH})_{12}(\mu\text{-1,1-N}_3)_6(\text{OH}_2)_6(\text{N}_3)_{1.5}\}\{\text{Mn}^{\text{II}}(\mu\text{-1,3-N}_3)_{4.5}(\text{OH}_2)_{1.5}\}]\text{Cl}_4\cdot\text{ca.7.5H}_2\text{O}$, (**3.3**, where glycH^{2-} is the dianion of propan-1,2,3-triol) in which the manganese centers can be described as a set of concentric Archimedean polyhedra. These clusters are linked into a 3D network isotypic to the iron pyrites structure. Upon heating, the porous compound undergoes a subtle structural rearrangement with the loss of some lattice waters. To date, this system represents the highest nuclearity manganese cluster which is linked into a 3D network.⁹¹

3.3.2. Results and discussion

3.3.2.1. Description of the structure: The structures of a fresh (as-prepared) crystal of **3.3** and a crystal that had been heated to 120 °C overnight (**3.3a**) were both determined at 100 K. Compound **3.3** was formulated as $[\{\text{Mn}^{\text{III}}_{12}\text{Mn}^{\text{II}}_9(\mu_4\text{-O})_8(\text{glycH})_{12}(\mu\text{-}1,1\text{-N}_3)_6(\text{OH}_2)_6(\text{N}_3)_{1.5}\}\{\text{Mn}^{\text{II}}(\mu\text{-}1,3\text{-N}_3)_{4.5}(\text{OH}_2)_{1.5}\}]\text{Cl}_4 \cdot \text{ca.}7.5\text{H}_2\text{O}$. The oxidation states of the all manganese were determined using bond valence sum calculations and based on the presence of Jahn-Teller axes through the Mn^{III} centers.²¹ The chloride anions and lattice waters were not directly observable in the structure and are presumably heavily disordered, but they could be inferred from microanalytical data.

Both the as-prepared (**3.3**) and heated (**3.3a**) samples crystallize in the cubic space group $\text{Pa}\bar{3}$. For **3.3a**, the reflections were, as expected, broader and the diffraction intensity fell away sharply at $2\theta > 45^\circ$. Fortunately, however, the crystal quality was still sufficient for the structure to be determined and refined, albeit with significantly higher *R*-factors. No great differences from the structure of **3.3** could be found, but heating the crystals causes a slight reduction in the unit cell volume, with *a* decreasing from 21.6500(7) to 21.5248(12) Å and the volume decreasing by 1.72 % from 10147.8(6) to 9972.8(1) Å³. The structural description given below is based on the data set obtained for **3.3**.

The structure of the $\text{Mn}^{\text{III}}_{12}\text{Mn}^{\text{II}}_9$ aggregate can be regarded as a series of concentric Archimedean polyhedra (Figure 3.9). At the center is a Mn^{II} cation, Mn(1), which lies on a site of crystallographic $\bar{3}$ symmetry (Wyckoff site *a*). This is surrounded by eight oxo ligands, with Mn(1)-O = 2.333(3) or 2.371(5) Å. These oxygens lie on the vertices of an almost perfect cube, with O··O in the range of 2.700-2.709 Å and the $\angle\text{O}\cdots\text{O}\cdots\text{O}$ angles all between 89.0 and 90.8°. These oxygens are further surrounded by a slightly distorted icosahedron of twelve Mn^{III} cations (Mn(2), Mn(3) and their symmetry-equivalents), with each oxygen forming a $\mu_4\text{-O}$ bridge between

Mn(1) and three of the Mn^{III} centers. The O-Mn^{III} distances are all in the range of 1.932-1.937 Å, and the \angle Mn^{II}-O-Mn^{III} and \angle Mn^{III}-O-Mn^{III} are in the range of 98.22-99.44° and 115.76-120.38°. These twelve Mn^{III} centers are all also linked pairwise by six (μ -1,1-N₃)⁻ ligands, with \angle Mn(2)-N(11)-Mn(3) = 127.08(17)°.

The eight triangular faces of the Mn^{III}₁₂ icosahedron that are bridged by one of the oxo ligands are capped by a Mn^{II} center (Mn(4), Mn(5) or their symmetry-equivalents), which are each linked *via* three deprotonated oxygens to the Mn^{III} centers at the vertices of the respective triangles. These eight Mn^{II} cations thus form a second larger cube surrounding the Mn^{III}₁₂ icosahedron (Figure 3.10).

Each of the twelve (glycH)²⁻ ligands provides two μ ₂-alkoxo bridges, with the third hydroxyl group of each ligand coordinating as a terminal ligand to a capping Mn^{II}. In the **3.3**, both these ligands are partly disordered as shown in Figure 3.11. Two of the oxygens are fixed, as are the carbons to which they are bonded. The remaining -CH₂OH group can be attached to either of those carbons resulting into disorder in the terminal ligand. In the case of the ligand involving oxygens O(3) and O(4), the hydroxymethyl group O(5A) is coordinated to Mn(4) as the major component (67%), while an aqua ligand O(9A) is coordinated to Mn(5). In the corresponding minor component, O(5B) is coordinated to Mn(5), while an azide is coordinated to Mn(4). This behavior is more important with the second independent (glycH)²⁻ ligand. In this case, the major (75%) component O(8A) is coordinated to Mn(5') while the azide nitrogen N(21A) occupies a coordination site of Mn(5). In the minor component, this is reversed and O(8B) coordinates to Mn(5) and N(21B) to Mn(5'). The result of this is that N(23A) is also coordinated to the mononuclear Mn^{II} cation Mn(6), forming a μ -1,3-N₃ bridge, while N(23B) is not coordinated giving disorder

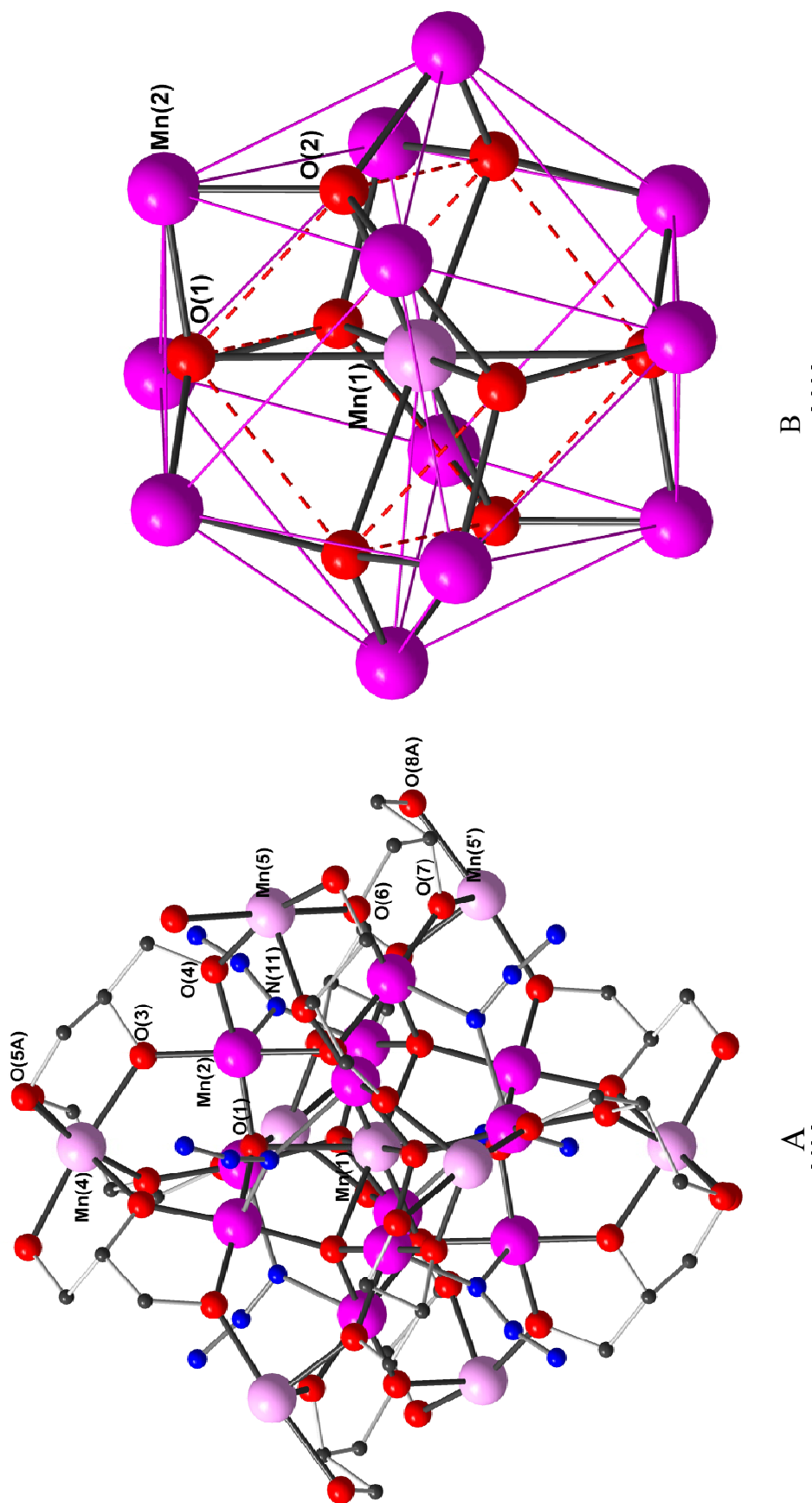


Figure 3.9: The core of the Mn₂₁ aggregate in 3.3 (A). For clarity, terminal ligands and minor disorder components of the organic ligands are omitted. (Mn^{III} purple, Mn^{II} pink). The Mn^{III}₁₂Mn^{II}(μ₄-O)₈ core of the Mn₂₁ aggregate in 3.3. (B) Mn(1) lies on $\bar{3}$ site and O(1) resides on a three-fold axis (B). To guide the eye, the red dashed lines emphasize the cubic array of eight oxo ligands about Mn(1), while the purple lines show the icosahedron of twelve Mn^{II} centers.

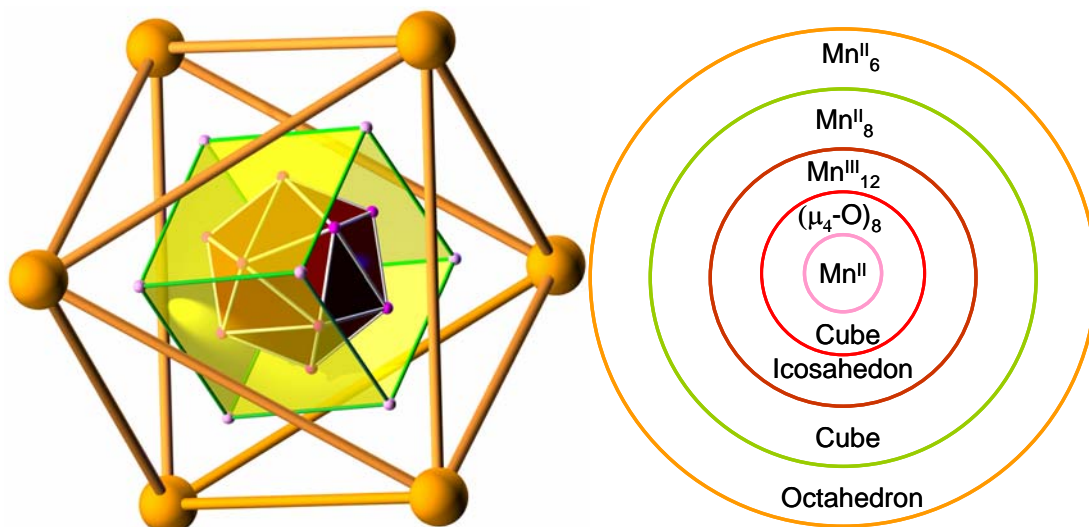


Figure 3.10. Representation of the concentric polyhedra present in compound **3.3** (left). The central Mn^{II} and its surrounding oxo-cube are omitted for clarity. Schematic diagram showing different concentric polyhedra (right).

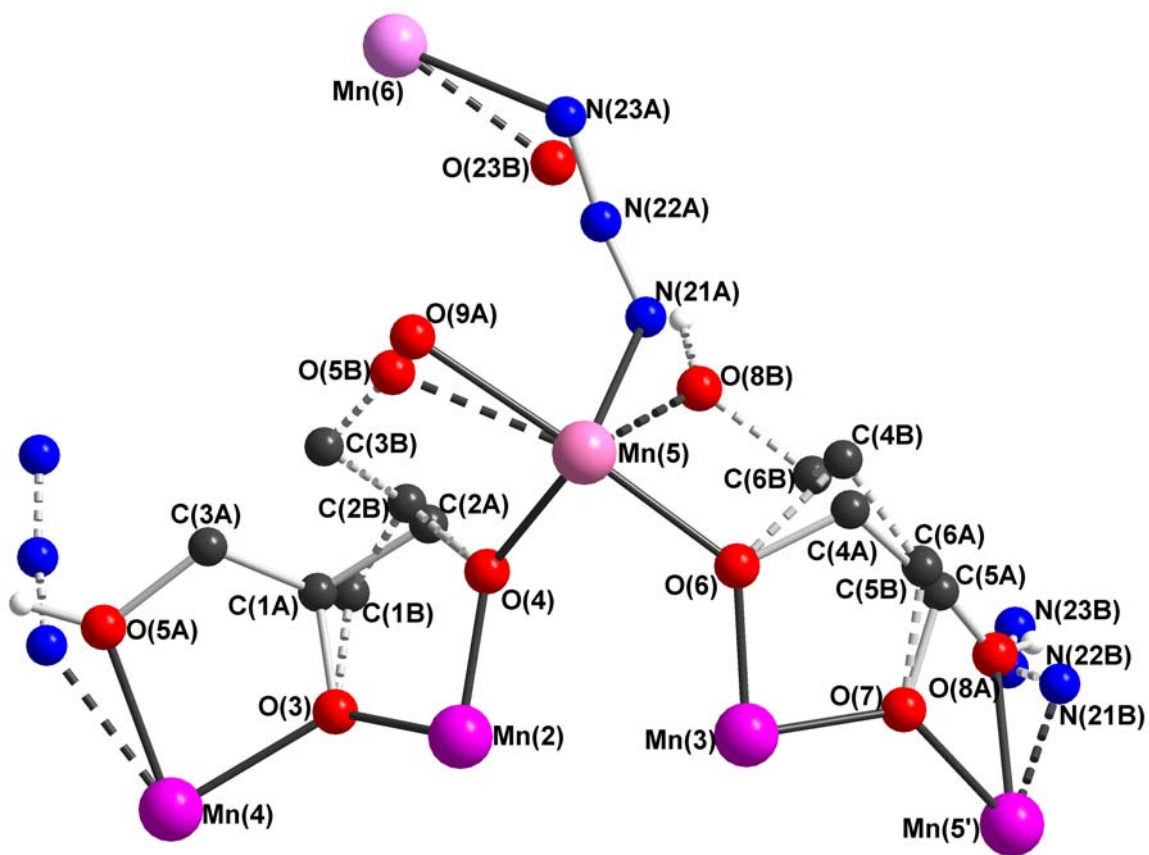


Figure 3.11: The disorder of the organic and terminal ligands in the structure of **3.3**. Minor disorder components are shown with dotted bonds.

in the octahedral coordination sphere of Mn(6), which also lies on a $\bar{3}$ symmetry site (Wyckoff site *b*). On average within the crystal structure, 75% of the coordination sites of Mn(6) are occupied by azides bridging from Mn₂₁ aggregates, and 25% by aqua ligands, O(21B). Each cluster unit is thus further surrounded by six different Mn^{II} mononuclear units which define the vertices of an octahedron, giving the last of the concentric polyhedra (Figure 3.10). With its cubic array of alternating cationic and anionic species with coordination numbers {6:6}, the structure is strongly reminiscent of that of NaCl. A more appropriate structural type, however, would be that of iron pyrites (FeS₂), which can be derived from a symmetry-lowering of the NaCl structure to space group $Pa\bar{3}$. In the present case, the Mn₂₁ units in occupy the of $\bar{3}$ symmetry sites corresponding to the positions of the disulfide dianions in FeS₂ (Figure 3.12 and 3.12).

3.3.2.2. Magnetic properties: Since the compound easily loses some lattice waters when isolated from the mother liquor, magnetic measurements were performed on a polycrystalline sample maintained in its mother liquor. For compound **3.3**, the χT product (Figure 3.13) at room temperature is 51.4 cm³Kmol⁻¹ which is lower than the value (79.75 cm³Kmol⁻¹) expected for the presence of ten Mn^{II} metal ions ($S = 5/2$, $g = 2$: $C = 4.375$ cm³Kmol⁻¹) and twelve Mn^{III} ions ($S = 2$, $g = 2$: $C = 3$ cm³Kmol⁻¹). On lowering the temperature, the χT product at 1000 Oe steadily decreases to reach a minimum value of 9.2 cm³Kmol⁻¹ at 1.8 K, indicating dominant antiferromagnetic interactions. The χT product showed no clear plateau at low temperatures. The magnetization as a function of field at low temperatures was measured up to 7 T between 1.8 and 8 K. Even at 7 T and

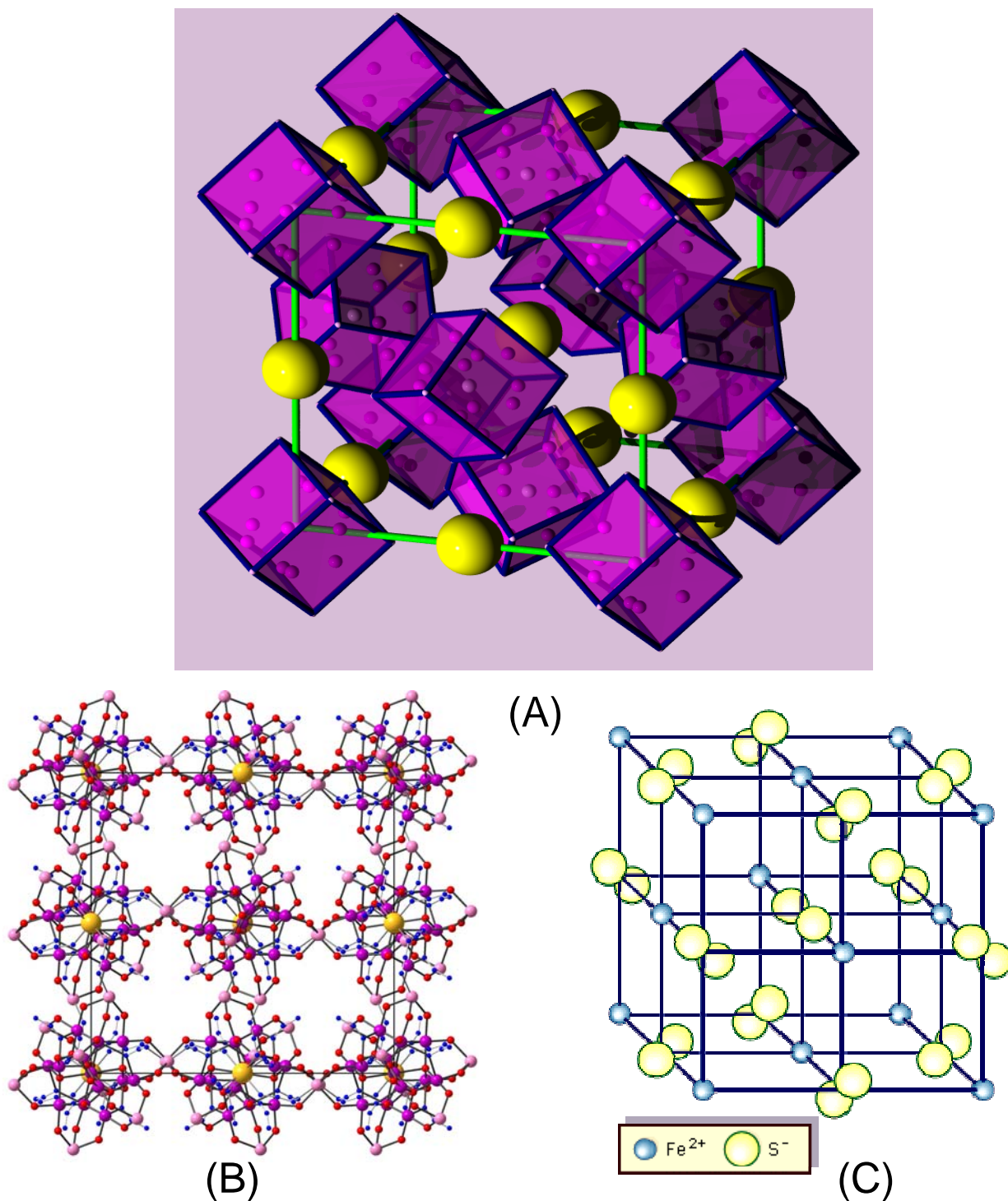


Figure 3.12: (A) POV-Ray representation of **3.3**. (B) The unit cell of **3.3** with the cationic cluster-units (cube) and anionic Mn^{II} linkers (yellow spheres) in the 3D network which resembles iron pyrites lattice-type (bottom). (C) Lattice of iron pyrite is shown.

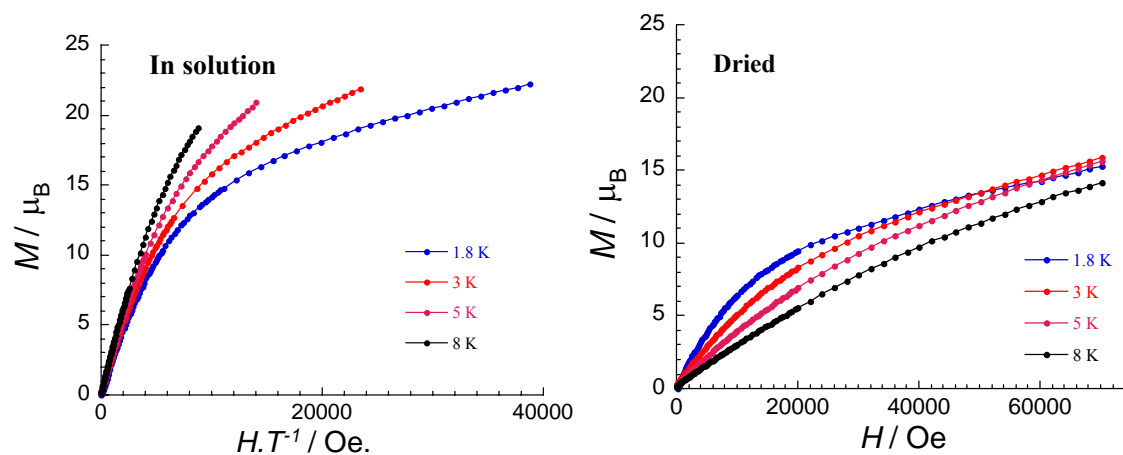
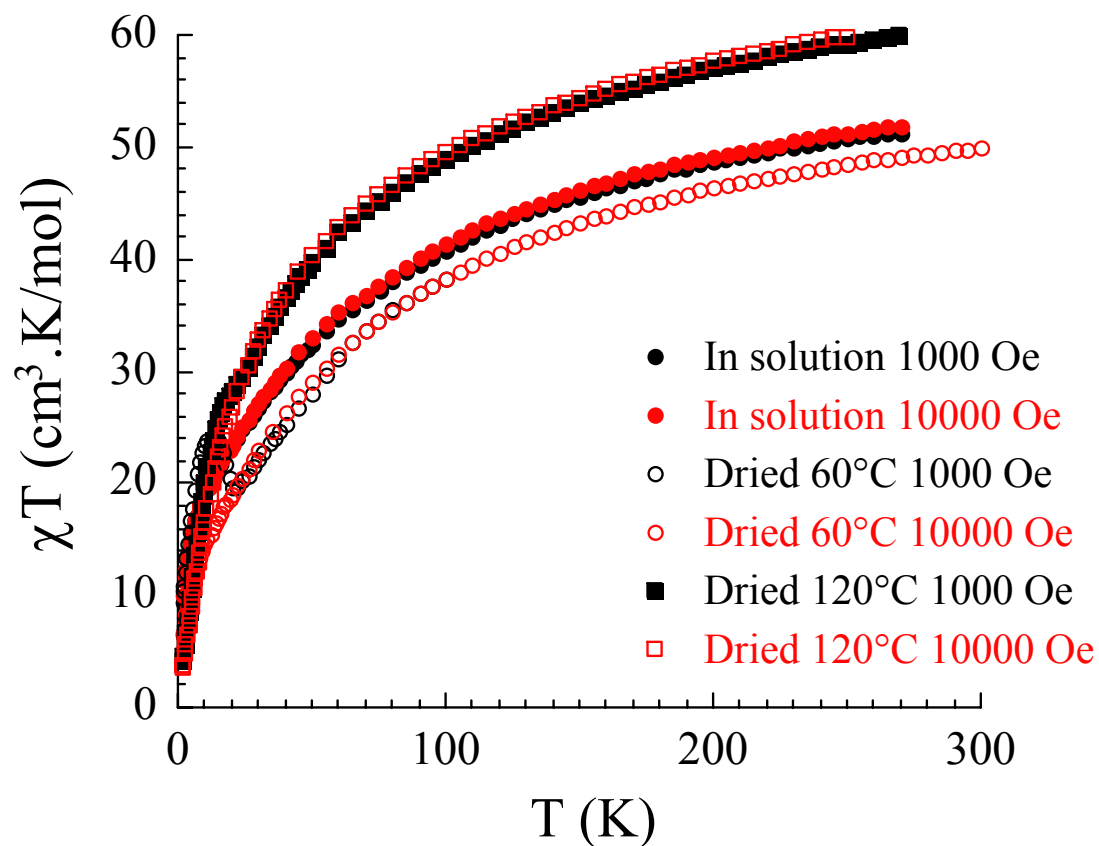


Figure 3.13: The magnetic susceptibility (top) and the magnetization (bottom) study for the fresh compound (3.3) and the dried compound (3.3a).

1.8 K, the magnetic moment, that reaches $22.2 \mu_B$, is not saturated. These results suggest the presence of magnetic anisotropy or a field-induced population of low-lying excited states in the Mn_{21} units, or (most likely) a combination of these. The M versus H/T plot confirmed that these effects are relevant, as the data are not superposed on a single master-curve as would be expected for a system with isotropic and well-defined spin ground states. Antiferromagnetic interactions between the Mn_{21} aggregates and the surrounding mononuclear Mn^{II} centers through the azide bridges are also possible. The susceptibility was also measured for the dried sample **3.3a** (Figure 3.13), and an increase in χT at room temperature was observed from $51.4 \text{ cm}^3\text{K/mol}$ to $60 \text{ cm}^3\text{Kmol}^{-1}$. The magnetization curve (Figure 3.13) for **3.3a** also varies from the original compound. This fact can be explained in terms of the disorder present in the structure. The fresh compound is more disordered and after heating, the disorder is minimized, and thus the magnetic coupling between the metal centers changes to some extent. This small change in the magnetic behavior is, therefore, assumed to be a consequence of the removal of structural disorder. Overall, the interpretation of the magnetic behavior is complicated by these effects, although the data do suggest that the Mn_{21} aggregates should have non-zero ground spin states.

3.3.3. Pyrolysis and degassing of the Mn_{21} network:

Thermogravimetric analysis of compound **3.3** was carried out. It was observed that the compound is thermally stable up to approximately $200 \text{ }^\circ\text{C}$ after which it decomposes very fast to MnO_2 . A systematic study was carried out on the pyrolysis and

solid state transformation of the Mn_{21} network, which leads to the formation of manganese dioxide with a sponge-like morphology.

3.3.3.1. Thermogravimetric analysis:

The thermogravimetric analysis (TGA) diagram (Figure 3.14) indicates the loss of lattice water molecules after 100 °C. Together with powder XRD, (Figure 3.15) this suggests that the structure still remains crystalline after heating at 100 °C. The single-crystal structure determination after heating at 120 °C suggested the formula $[\text{Mn}^{\text{III}}_{12}\text{Mn}^{\text{II}}_9(\mu_4\text{-O})_8(\text{glycH})_{12}(\mu\text{-}1,1\text{-N}_3)_6(\text{OH}_2)_4(\text{N}_3)_2]\{\text{Mn}^{\text{II}}(\mu\text{-}1,3\text{-N}_3)_6\}\cdot ca.4\text{H}_2\text{O}$ (**3.3a**), with a loss of *ca.* three water molecules. The compound starts to decompose around 200 °C resulting in manganese dioxide. The residual mass after the experiment was consistent with the value expected for all Mn being incorporated into MnO_2 .

3.3.3.2. Powder XRD analysis:

A systematic XRD study was performed on the compound after heating at different temperatures (Figure 3.15). The powder pattern indicates the decomposition of the crystalline compound around 200 °C, which is in agreement with the TGA data. The compound then goes through some amorphous transition state to finally produce MnO_2 at higher temperature. The powder XRD data taken after heating at 500 °C suggested the presence of the $\beta\text{-MnO}_2$ phase with an intense peak around $2\theta = 33$ corresponding to the 110 reflections.⁹²

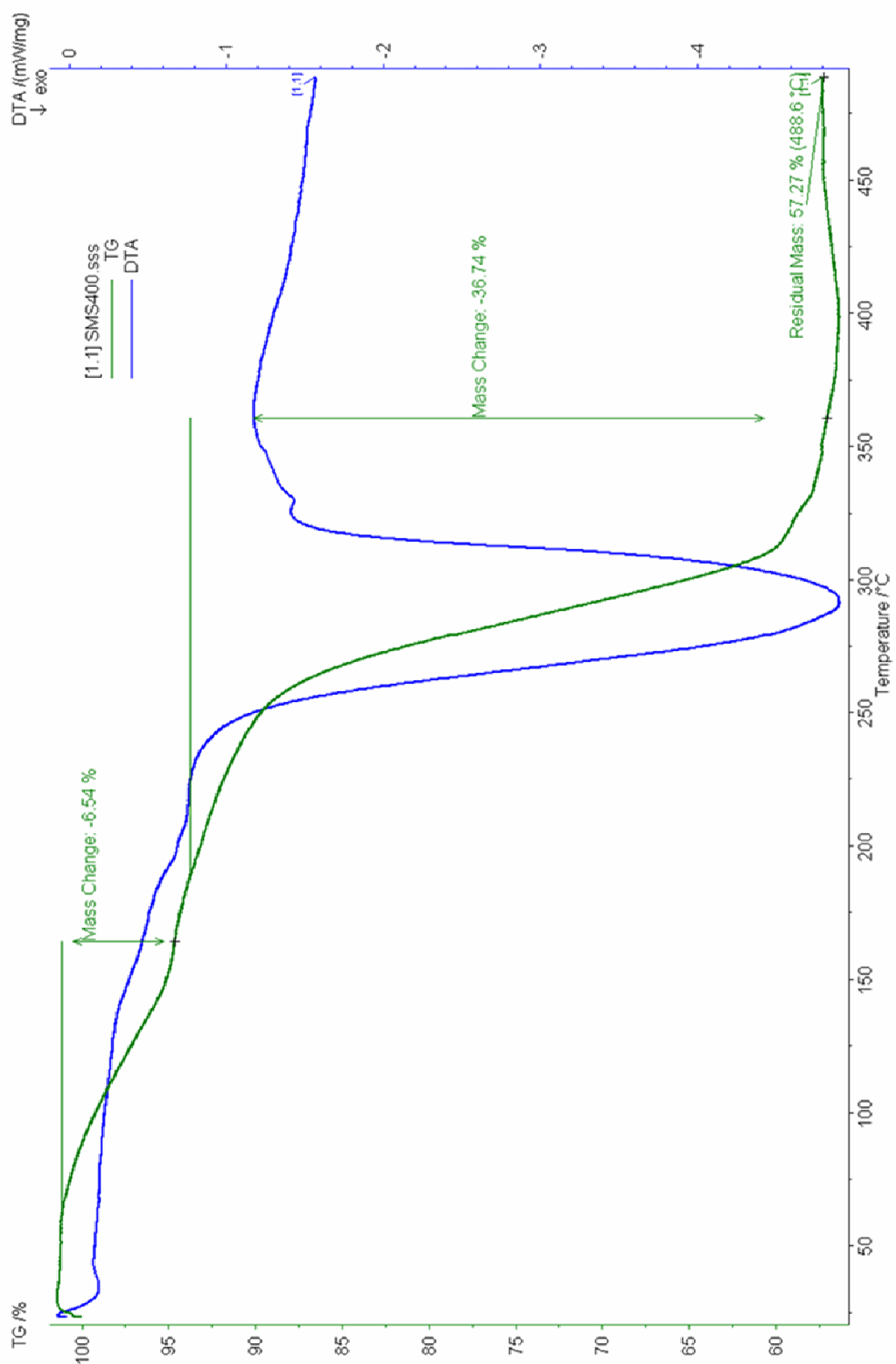


Figure 3.14: TGA of compound 3.3 indicating decomposition after 200 °C leading to the formation of MnO₂.

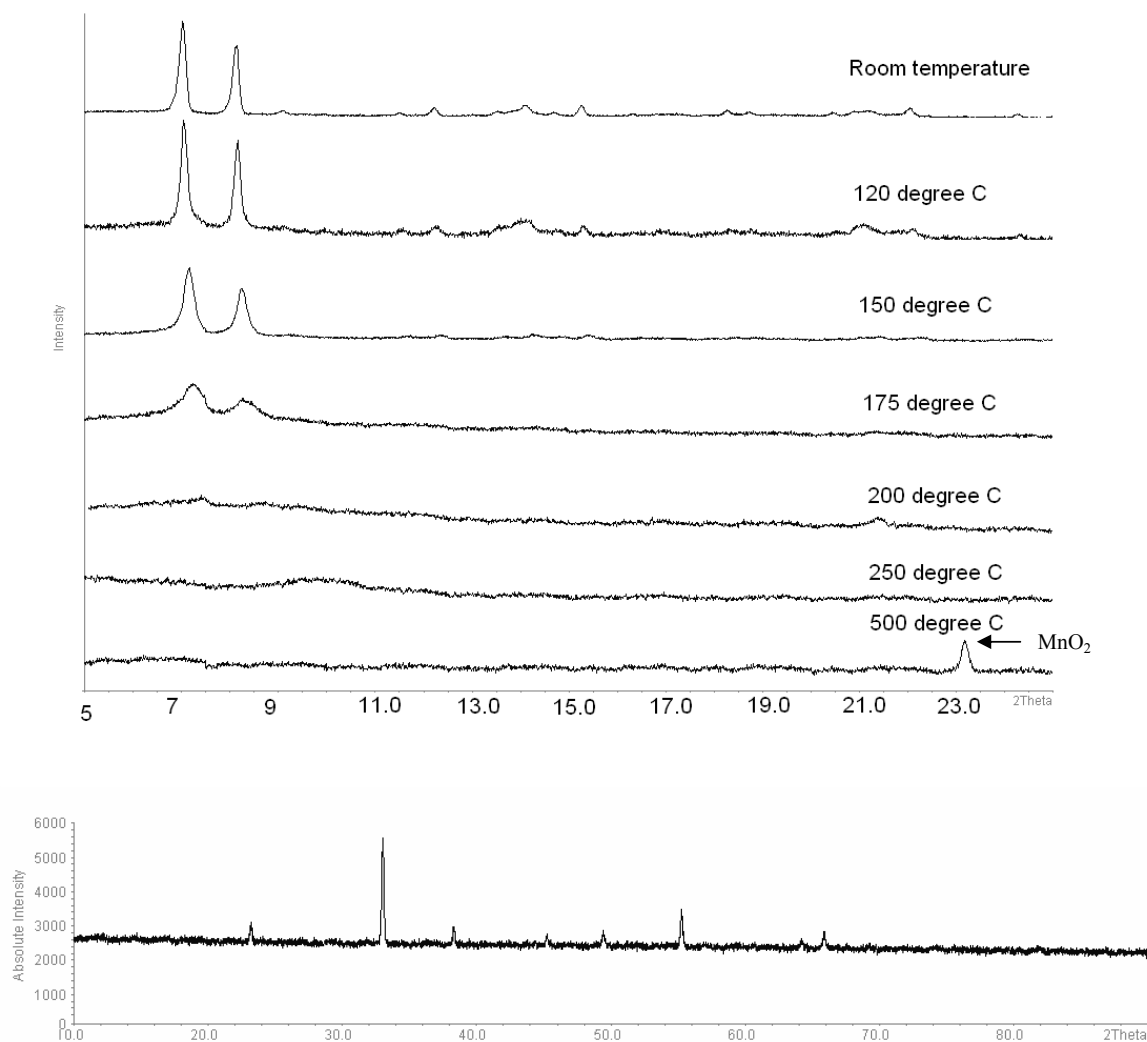


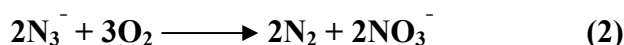
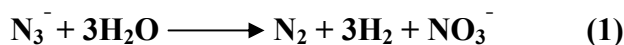
Figure 3.15: Powder XRD shows the loss of crystallinity at higher temperature (top). At 500 °C, the peak at $2\theta = 33$ indicates the presence of β -MnO₂. The full range of powder XRD pattern for the MnO₂ is shown at the bottom.

3.3.3.3. Infrared spectroscopy study:

From the infrared spectra of samples heated at different temperatures, loss of lattice water (1630 cm^{-1}) was evident at higher temperatures (Figure 3.16). A peak at 1384 cm^{-1} , characteristic of the symmetric stretch of $(\text{NO}_3)^-$, appears at higher temperature (120 °C). The broad peak around 1590 cm^{-1} can be assigned to the asymmetric stretch of the $(\text{NO}_3)^-$ group. The formula, together with the TGA analysis, suggests that there is a possibility of nitrate formation from the reaction between

the lattice waters and the azide ions. Another possibility is the aerial oxidation of azide at higher temperature.

The two possible reactions are given below:



Scheme 3.1: Proposed reaction mechanism for nitrate formation.

The sample was heated in a nitrogen atmosphere and checked using infrared spectroscopy. The characteristic peak for nitrate, however, was still present. This suggests that the azide is in fact oxidized by the lattice water according to reaction 1.

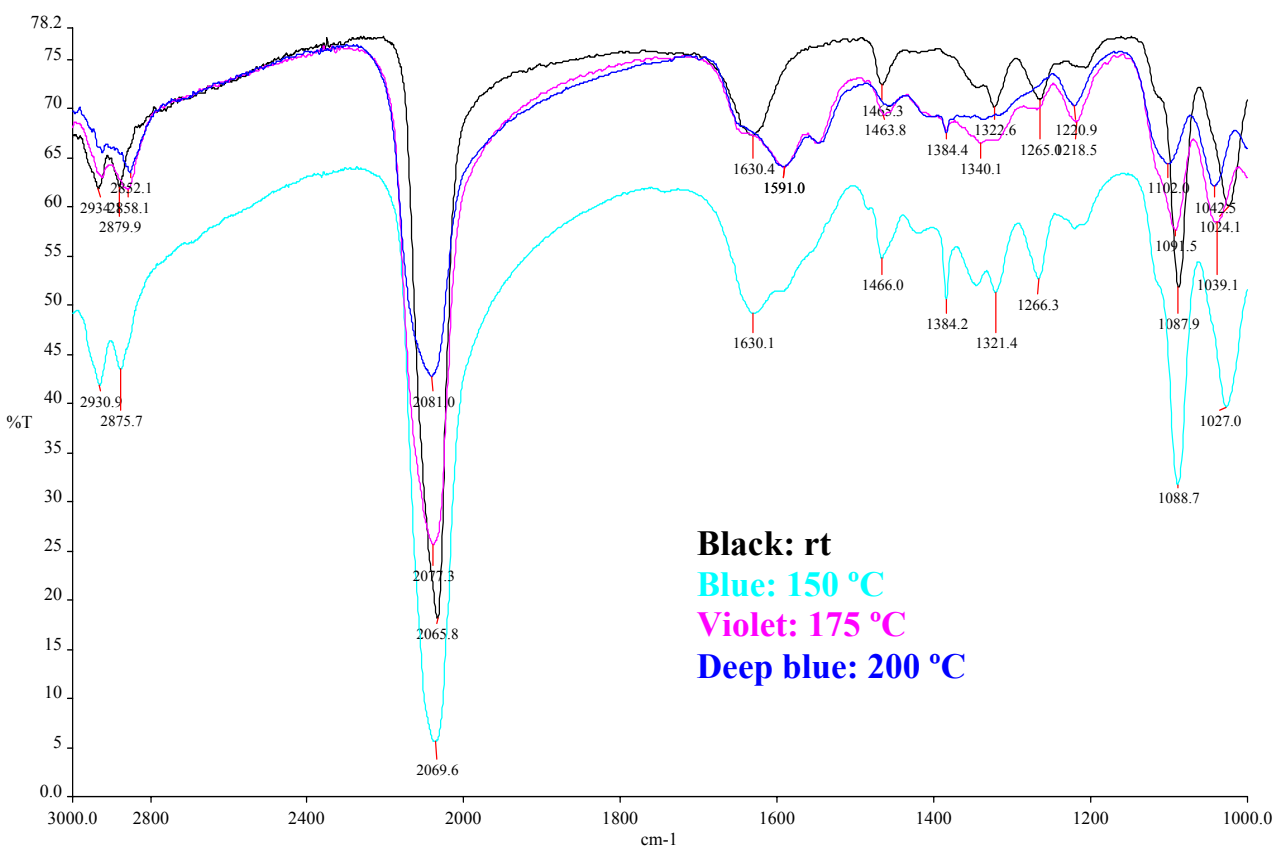


Figure 3.16: Presence of the characteristic peak for nitrate group can be observed in the IR spectra of the heated sample.

3.3.3.4. Scanning electron microscopy:

A systematic SEM investigation on the heated compound was done. For a fresh sample, the smooth crystal-faces were clearly observed (Figure 3.17). SEM images were taken after heating the compound at different temperatures. The smoothness of the surface disappeared when the compound was heated at higher temperature. Holes were observed on the surface (Figure 3.18) when it was heated at 190 °C, which seems to be the result of the interaction of the crystal waters with the azide to give N₂, H₂ and nitrate. Heating at higher temperature shows many cracks and bubbles on the surface. The heated material was cut with a focused ion beam (FIB) and micrometer-sized sponge-like compartments were found inside the structure. Some intruding structures were also found on the surfaces which were full of hollow bubbles likely due to the degassing of H₂, N₂, CO₂, H₂O etc. during the pyrolysis.

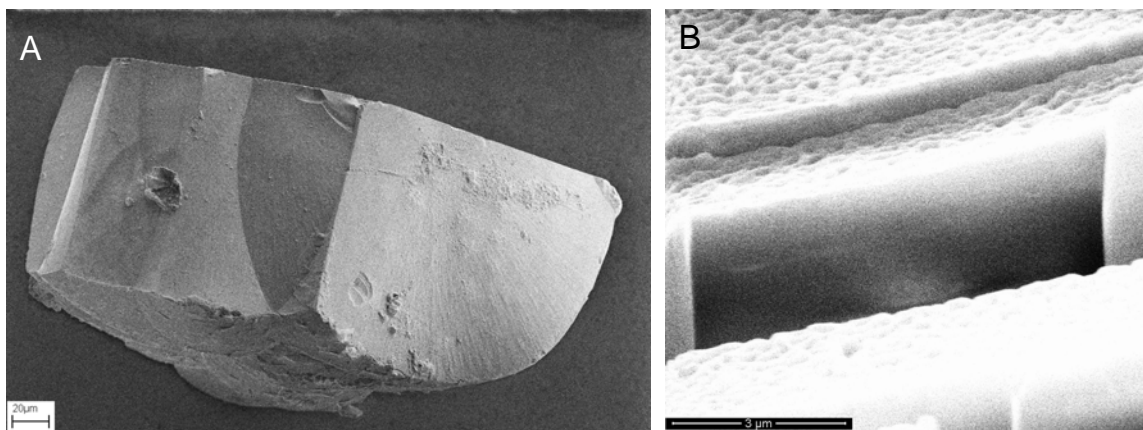


Figure 3.17: Smooth crystal faces were observed before heating (A). A part of the crystal was dissected using a focused ion beam. It shows that the fresh crystal is solid, without any pores(B). (Scale bars 20 (left) μm and 3 μm (right))

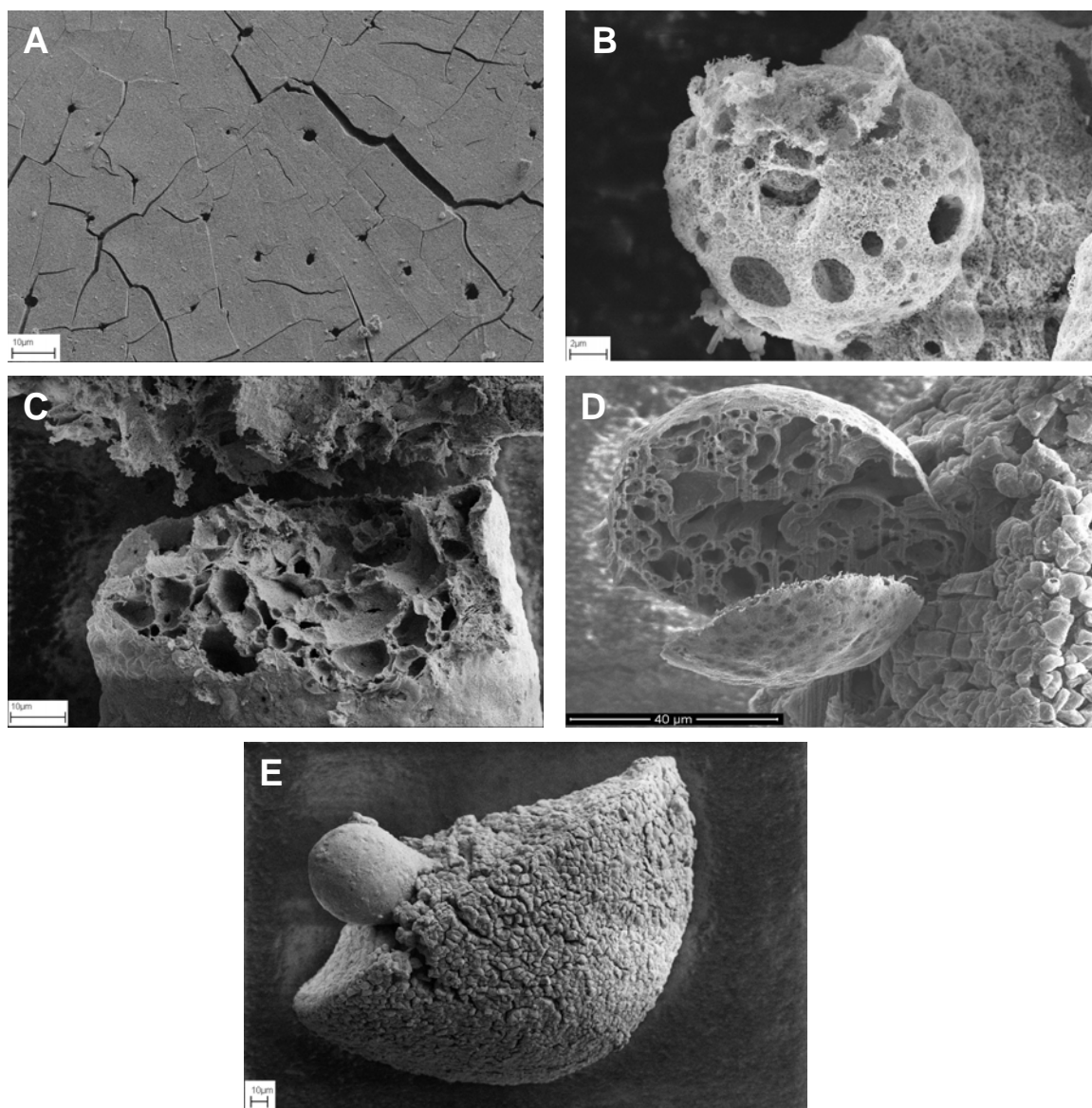


Figure 3.18: Pores on the crystal surface observed after heating at 200 °C (A). Heating the crystal at 500 °C produced porous MnO₂ (B, C). The formed MnO₂, cut using a FIB, shows that the morphology is very porous. Intrusions due to degassing (N₂, H₂, CO₂, H₂O, CO) during pyrolysis (E). Scale bars for A, B, C, D and E are 10 μm, 2 μm, 10 μm, 40 μm, 10 μm, respectively.

3.3.3.5. Capacitance measurements:

Observing the high surface area of the β-MnO₂ produced by the pyrolysis of **3.3**, it was expected that the compound may show high capacitance and could be used as an anode in a Li-ion battery. The porous β-MnO₂ was cycled against a Li metal counter electrode between 4.15 V and

0.3 V. In the first discharge a plateau was found at about 0.35 V, which translates to a capacity of about 760 mAh/g (Figure 3.19), which is higher than the usual graphite anodes used in battery. However, unfortunately after 10 cycles, the capacity decreases to values around 20 mAh/g .

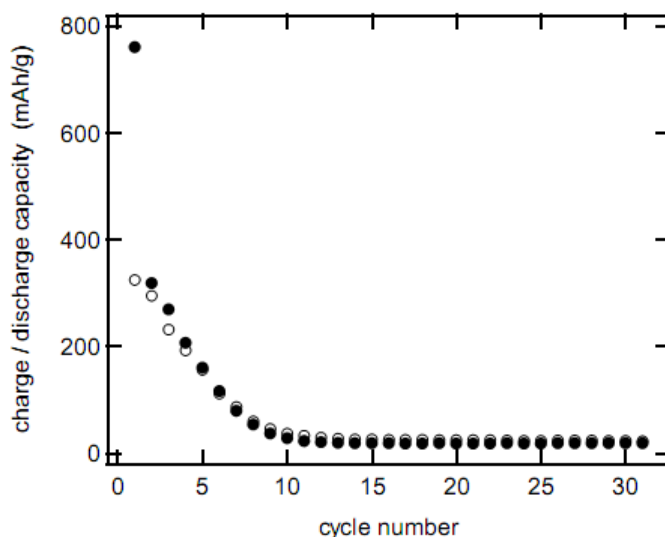


Figure 3.19: Capacitance measurements for the porous β -MnO₂ obtained from pyrolysis of **3.3**. Solid and empty dots represent measurements using 4.15 V and 0.3 V, respectively

3.4. An Fe₆ cluster: [Fe₆O₂(Piv)₆(PdolH)₆](NO₃)₂·2CH₃CN (**3.4**), connecting two Fe₃-triangles

3.4.1. Introduction:

Iron coordination clusters constitute the second largest family of single-molecule magnets. The synthesis and characterization of iron clusters started long before the magnetic bistability of SMMs was discovered. The main purpose was to investigate building blocks for molecular magnetic materials, to mimic the iron-containing active sites of different metallo-enzymes, and to model and investigate the iron-storage protein, ferritin, which itself can be considered as a nano-

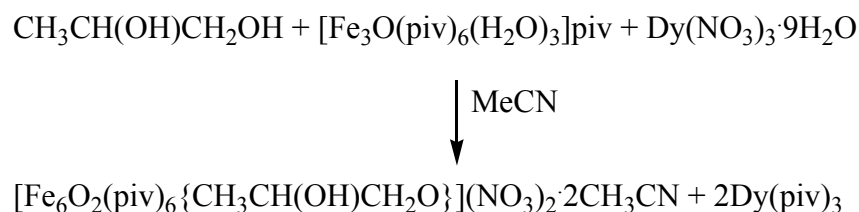
sized magnet. Iron can be used as building units of SMMs because it can possess high ground state spins. Use of high-spin metal ions is a convenient way of synthesizing SMMs because a few ferromagnetically coupled metal centers can give a high-spin cluster. For example, following a recent review by Sessoli *et al.*, we can say, “Two ions with $S = 5/2$ ferromagnetically coupled have a ground state with $S = 5$, while it is necessary to assemble a cluster of ten $S = 1/2$ ions in order to achieve the same result”.³² This is the reason why the high spin metal ions, like Fe^{III} ($S = 5/2$), Mn^{III} ($S = 5/2$) and Fe^{II} ($S = 2$) have been largely used in the synthesis of SMMs. During the last few years, many iron clusters have been synthesized and studied magnetically.³²⁻³⁵ Most of the clusters though have been made by serendipitous self-assembly. In this work, the self-assembly technique is used in a controlled way to synthesize a high-nuclearity iron cluster.

As part of the investigation of the use of poly-alkoxy ligands, attempts were made to connect Fe_3 clusters by ligand substitution. $[\text{Fe}_3(\mu_3\text{-O})(\text{piv})_6(\text{H}_2\text{O})_3]\text{piv}$ (pivH = pivalic acid) was used as a starting material. Propane-1,2-diol (PdolH_2) was used to replace some of the pivalates. This approach was successful and two trinuclear units were connected to give a Fe_6 cluster, $[\text{Fe}_6\text{O}_2(\text{Piv})_6(\text{PdolH})_6](\text{NO}_3)_2 \cdot 2\text{CH}_3\text{CN}$ (**3.4**).

3.4.2. Results and discussions

3.4.2.1. Description of the structure: The compound crystallizes in the triclinic space group $P\bar{1}$ (Figure 3.20) according to Scheme 3.2. The starting compound $[\text{Fe}_3(\mu_3\text{-O})(\text{piv})_6(\text{H}_2\text{O})_3]\text{piv}$ was synthesized following a reported procedure.³⁶ All the irons are in +3 oxidation state. The oxidation states of the iron were determined by BVS calculations and by observing the crystallographic Fe-O bond lengths.¹⁹ Interestingly, $\text{Dy}(\text{NO}_3)_3 \cdot 9\text{H}_2\text{O}$ plays a vital role in this synthesis. Being a hard acid, Dy^{3+} attracts the carboxylate (piv^-) ligands from the Fe_3 cluster and thus following replacement of the pivalates by the di-alkoxy ligand. This mechanism is

supported by the fact that the presence of Dy(piv)₃ was detected at the end of the synthesis. The white precipitate was analyzed with oxalic acid and white insoluble dysprosium complex found as a test for dysprosium. The characteristic band of carboxylic group was found in IR spectra which supports the formation of Dy(piv)₃.



Scheme 3.2: Synthesis of compound **3.4** is shown.

It can be seen that two Fe₃ triangular units are linked in a staggered fashion in compound **3.4**. The outer coordination sites are completed by pivalates whereas PdolH⁻ ligands have replaced the other pivalates and water to link the two units. In both triangular units, three iron centers are linked *via* a μ₃-oxo group as in the original starting Fe₃ cluster. The cluster can be best described as an octahedron, in which six Fe^{III} ions occupy the six vertices (Figure 3.20). An octahedron is a trigonal antiprism. The two Fe₃ triangular units occupy the corner of two staggered opposite triangular faces of the octahedron (Figure 3.20). Another Fe₆ cluster with antiprismatic core was synthesized earlier in our research group by R. K. Henderson.⁹³ The Fe^{III}...Fe^{III} distances in each triangle lie between 3.304 Å and 3.444 Å. The μ₃-O-Fe^{III} distances are in the range of 1.907 Å to 1.917 Å. The Fe^{III}-μ₃-O-Fe^{III} angles are in the range of 118.5° to 121.2°. The di-alkoxy ligand is totally deprotonated, and each ligand makes three coordination bonds to two Fe^{III} ions. One alkoxy group is coordinated to one Fe^{III} ion and another alkoxy group makes a μ₂-bridge between Fe^{III} ions from the two triangular units.

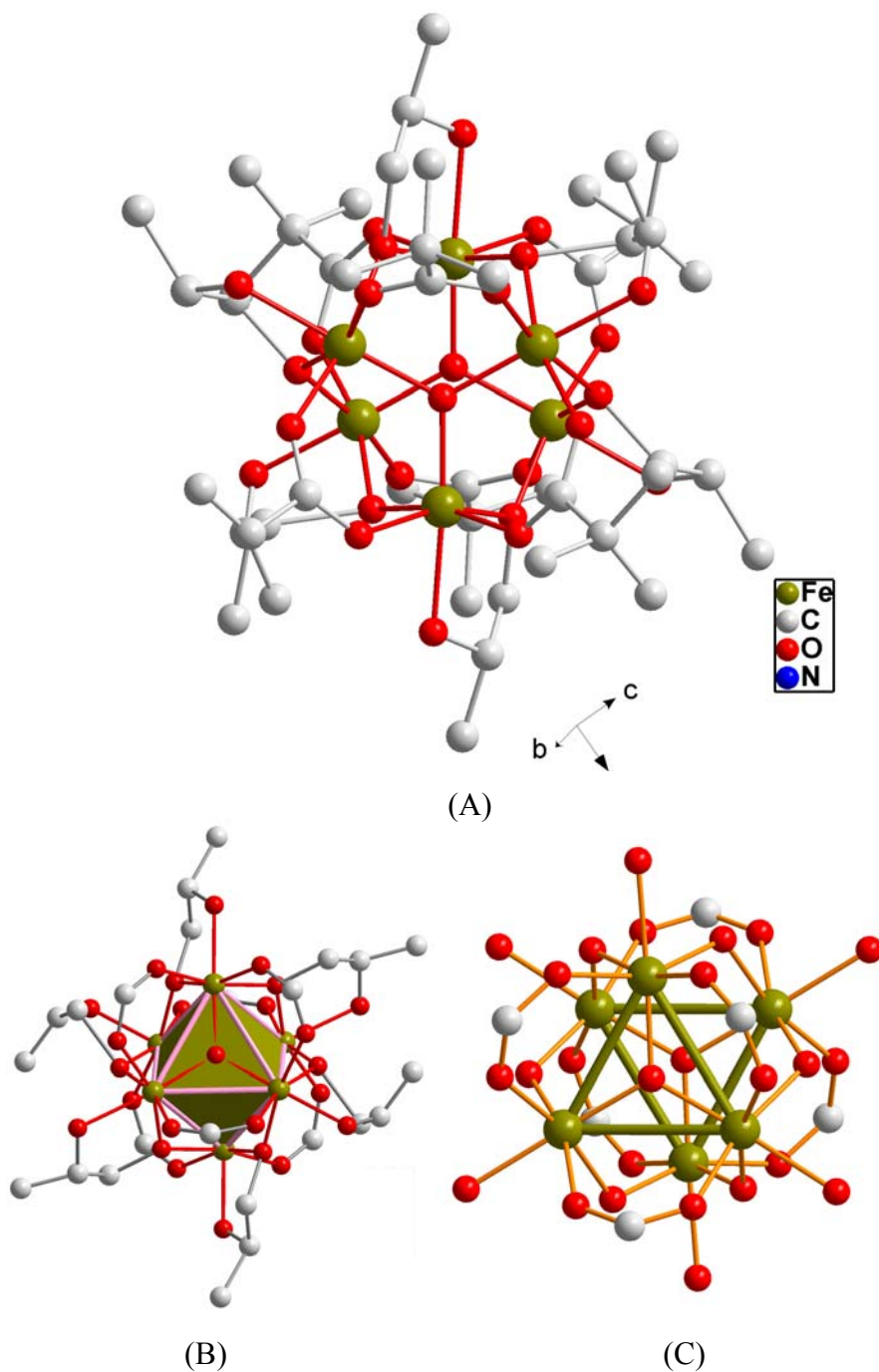


Figure 3.20: Molecular structure of compound 3.4. (A). A polyhedral view of the Fe₆ cluster (B). Two triangular faces of the Fe₆ cluster organized in a staggered fashion. Hydrogen atoms and solvent molecules are not shown for clarity.

3.4.2.2. Magnetic properties. Magnetic susceptibility measurements were carried out for compound **3.4** with an applied field of 1000 Oe (Figure 3.21). At room temperature, the magnetic susceptibility was found to be $6.56 \text{ cm}^3\text{Kmol}^{-1}$ which is very small compared to the expected value of $26.25 \text{ cm}^3\text{Kmol}^{-1}$ for six isolated Fe^{III} ions. This observation, coupled with the steep decrease

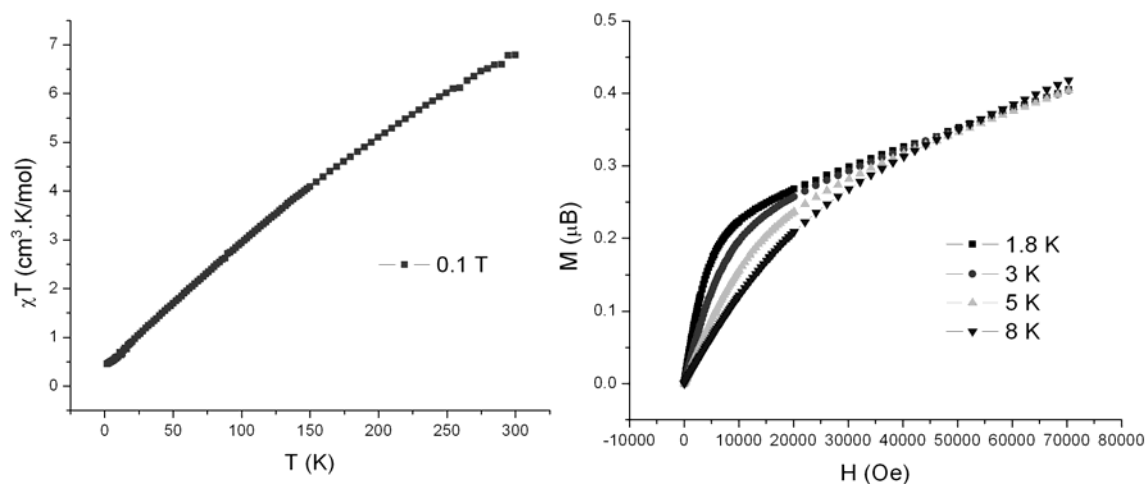


Figure 3.21: Temperature dependence of the magnetic susceptibility of compound **3.4** (left). Magnetization of compound **3.4** (right) is shown.

of χT with temperature, indicates that the metal ions are strongly antiferromagnetically coupled. The magnetization was also studied within a range of 0 to 70000 Oe at different temperatures. The plot indicates that the magnetic moment reaches $0.42 \mu_{\text{B}}$ at 1.8 K in an applied field of 70000 Oe. It further suggests that the spins on the Fe^{III} ions are oriented in such a way that they mostly cancel each other with almost a zero ground spin state.

3.5. Summary

In the course of investigations into new magnetically interesting clusters, three new Mn clusters and a new Fe cluster were synthesized. All display regular geometries for the metal centers which correspond to Archimedean polyhedra or nested version of these.

A new Mn^{III}_6 cluster, **3.1**, containing an octahedral core and a μ_6 -oxo bridging atom, was synthesized using PtolH_4 as a ligand. Acetate was used as a co-ligand to satisfy the terminal coordination sites of Mn^{III} . The clusters were inter-connected *via* the presence of strong hydrogen bonding through the neighboring ethylenediamine molecules. The compound shows a ground spin state of about $S = 3$. The presence of anisotropy and slow relaxation of magnetization indicates that the compound is likely to be a single-molecule magnet.

A Mn_{17} cluster (**3.2**) was synthesized during the course of this investigation. Compound **3.2** possesses an interesting structure with a pair of Mn_{10} supertetrahedra linked via a common edge. Besides its interesting structure, the compound is magnetically very interesting. It was found to be ferromagnetically coupled and to possess a very high ground state spin of approximately 28. The compound also shows magnetic hysteresis and slow relaxation of magnetization at very low temperature. The anisotropy is likely to be coming from the uncompensated Jahn-Teller deformations. In such case, compound **3.2** may be a very high-spin SMM.

A 3D network (**3.3**) was synthesized with Mn_{21} repeating units connected *via* mononuclear $\text{Mn}^{\text{II}}(\text{N})_6$ linkers and with glycerol as the poly-alkoxy ligand. The compound shows overall antiferromagnetic behavior. It was interesting to observe the change of magnetic behavior upon desorption of the crystal waters in this compound. Moreover, the removal of crystal waters by heating brings significant changes in the magnetic properties with an increment in the magnetic susceptibility. Compound **3.3** shows high thermal stability. At very high temperature, the compound decomposes into the porous $\beta\text{-MnO}_2$ morphology, which shows a good capacitance when used as an anode in a Li-ion battery. In this way, the magnetically interesting molecule was found to have an additional application. A nitrate formation reaction mechanism was also discovered during the heat-treatment of compound **3.3**.

The last section demonstrated how the nuclearity of iron clusters can be increased by using smaller units. An Fe₆ cluster was synthesized using Fe₃ building units linked *via* a di-alkoxy ligand. The compound is overall antiferromagnetically coupled, and possesses a nearly zero ground spin state.

Finally, it can be said that in all these molecules, poly-alkoxy ligands play a major role in self-assembly of transition metal clusters. As a result, some high nuclearity Mn and Fe clusters were synthesized. Evidently, these kinds of ligand are useful and have a great prospect in synthesizing magnetically interesting Mn and Fe clusters.

CHAPTER 4

A family of 1D lanthanide chain compounds

4.1. Introduction

Lanthanide compounds are prospective candidates for showing interesting magnetic behavior. In contrast to the *d*-block transition metals, lanthanides possess very similar chemical properties which make it possible to replace the metal centers in a lanthanide compound with different lanthanide ions to result in a family of isostructural compounds. In this way, it is possible to synthesize a class of homologous compounds and to tune their magnetic properties by choosing the appropriate lanthanide metal ions. It is a very common fact and observed very often in a series of lanthanides compounds that there are often changes in structure on moving left to right in the lanthanide series. The magnetic property also shows a great variation depending on the electronic environment of the lanthanides. This fact is the main inspiration behind using lanthanide metal ions to synthesize magnetically interesting compounds.

The most common oxidation state of the lanthanide ions is +3 and they are “hard acids” preferring to coordinate with “hard bases”. This is why lanthanides have a very strong affinity towards coordination with oxygen ligands. The di-alkoxy ligand, ethylene glycol (EtglyH₂), and sodium benzoate were used to synthesize a family of one-dimensional chain complexes of lanthanides, [Ln(PhCOO)₃(EtglyH₂)(MeOH)], where Ln represents Pr, Nd, Gd, Tb, Dy, Ho and Er. The electronic configurations and the radii of the Ln³⁺ ions are given in Table 4.1. Although coupling between lanthanides always seems very small,⁹⁴ the high spins and /or high anisotropies seem to lead to some very unexpected magnetic properties. For example, work from our group has shown (a) adding paramagnetic Ln to a Mn^{III}₄Mn^{IV} motif enhances U_{eff} and (b) exotic SMM behavior originating from excited states is seen for a Dy₃ system.

Element	Ce	Pr	Nd	Pm	Sm	Eu	Gd	Tb	Dy	Ho	Er	Tm	Yb	Lu
Atomic electronic config	4f ¹ 5d ¹ 6s ²	4f ³ 6s ²	4f ⁴ 6s ²	4f ⁵ 6s ²	4f ⁶ 6s ²	4f ⁷ 6s ²	4f ⁷ 5d ¹ 6s ²	4f ⁹ 6s ²	4f ¹⁰ 6s ²	4f ¹¹ 6s ²	4f ¹² 6s ²	4f ¹³ 6s ²	4f ¹⁴ 6s ²	4f ¹⁴ 5d ¹ 6s ²
Ln ³⁺ electron config	4f ¹	4f ²	4f ³	4f ⁴	4f ⁵	4f ⁶	4f ⁷	4f ⁸	4f ⁹	4f ¹⁰	4f ¹¹	4f ¹²	4f ¹³	4f ¹⁴
Ln ³⁺ radius(pm) -6 coord.	102	99	98.3	97	95.8	94.7	93.8	92.3	91.2	90.1	89	88	86.8	86.1

Table 4.1: The electronic configurations and the ionic radii are given for the lanthanide atoms and ions.

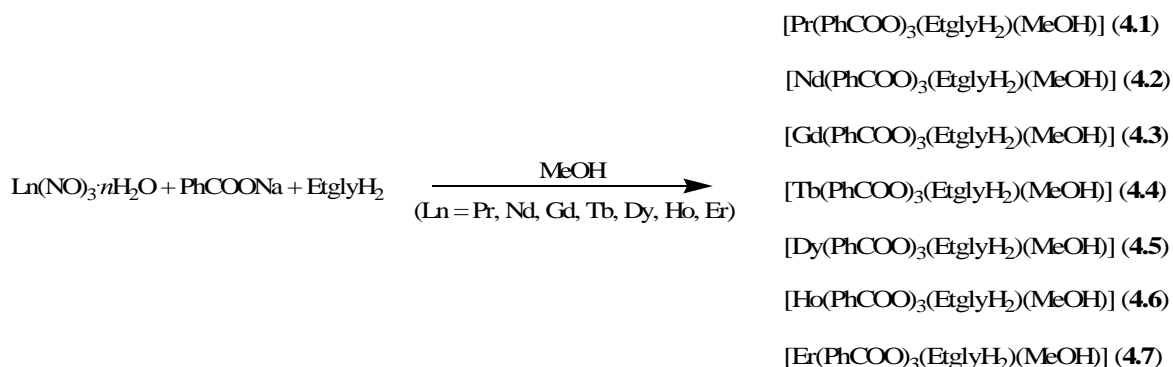
Forty years ago, R. J. Glauber reported that the one-dimensional chain compounds may exhibit slow relaxation of magnetization if two conditions are fulfilled; namely, the compound possesses Ising magnetic anisotropy, and the compound has negligible inter-chain interactions.⁹⁵ In 2001, this phenomenon was discovered in a compound for the first time.⁹⁶ Since then, other compounds have been reported, and they have been called as single chain magnets (SCMs).⁹⁷⁻¹⁰³

The rational design and synthesis of new compounds with unconventional magnetic properties is a considerable challenge for chemists.¹⁰⁴ Using lanthanide ions, it is possible to tune and study the periodic trends of the magnetic properties of an isostructural family. In this investigation, a family of homologous 1D lanthanide chains was synthesized, giving us an opportunity for a detailed study and comparison of their magnetic properties.

4.2. Results and discussion

4.2.1. Synthesis and structural description. As the chemical properties of the lanthanide rare earth metals are strikingly similar, all the above-mentioned compounds were synthesized in the same way (Scheme 4.1).¹⁰⁵ Each Ln(NO₃)₃·nH₂O salt (0.5 mmol) was treated with 1 mmol of EtglyH₂ and PhCOONa in methanol. A series of isostructural compounds, [Ln(PhCOO)₃(EtglyH₂)(MeOH)], was obtained. Single-crystal X-ray analyses were performed only for two compounds (Ln = Gd, **4.3** and Ln = Dy, **4.5**, Figure 4.1). Other compounds were characterized by matching their FT-IR spectra and elemental analysis with

the two structurally characterized compounds. As a further proof of the isostructural nature, the powder diffraction patterns were recorded for **4.1**, **4.2**, **4.4**, **4.6** and **4.7**, and compared with the simulated diffraction patterns of **4.3** and **4.5**. Except for small differences in crystallinity, all the powder XRD patterns were found to be similar (Figure 4.2).



Scheme 4.1: Synthetic scheme for the preparation of $[\text{Ln}(\text{PhCOO})_3(\text{EtglyH}_2)(\text{MeOH})]$ (Ln = Pr, Nd, Gd, Tb, Dy, Ho and Er) chains.

As all compounds are isostructural, only the structural description of **4.3** is given in detail (Figure 4.1). The compound crystallized in the triclinic space group $P\bar{1}$. The structure consists of one-dimensional chains parallel to the crystallographic a axis. The metal ions are connected to two of its neighboring metal ions *via* four carboxylate bridges from the benzoate ligands. Each Gd^{3+} ion is coordinated by eight oxygen atoms, and the coordination geometry around the Gd^{3+} ions can be described as distorted dodecahedral. The eight coordination sites are satisfied by eight oxygen atoms from four bridging carboxylates, one terminal carboxylate, one chelating ethylene glycol and one methanol. There are two different kinds of alternating metal-metal distances, 4.817 Å and 5.028 Å, along the chain. This should satisfy the first criterion for a SCM by leading to different magnitudes for the coupling along the chain. From the packing diagram in Figure 4.2, it can be seen that the chains are parallel to the crystallographic a axis and are separated by the aromatic benzene

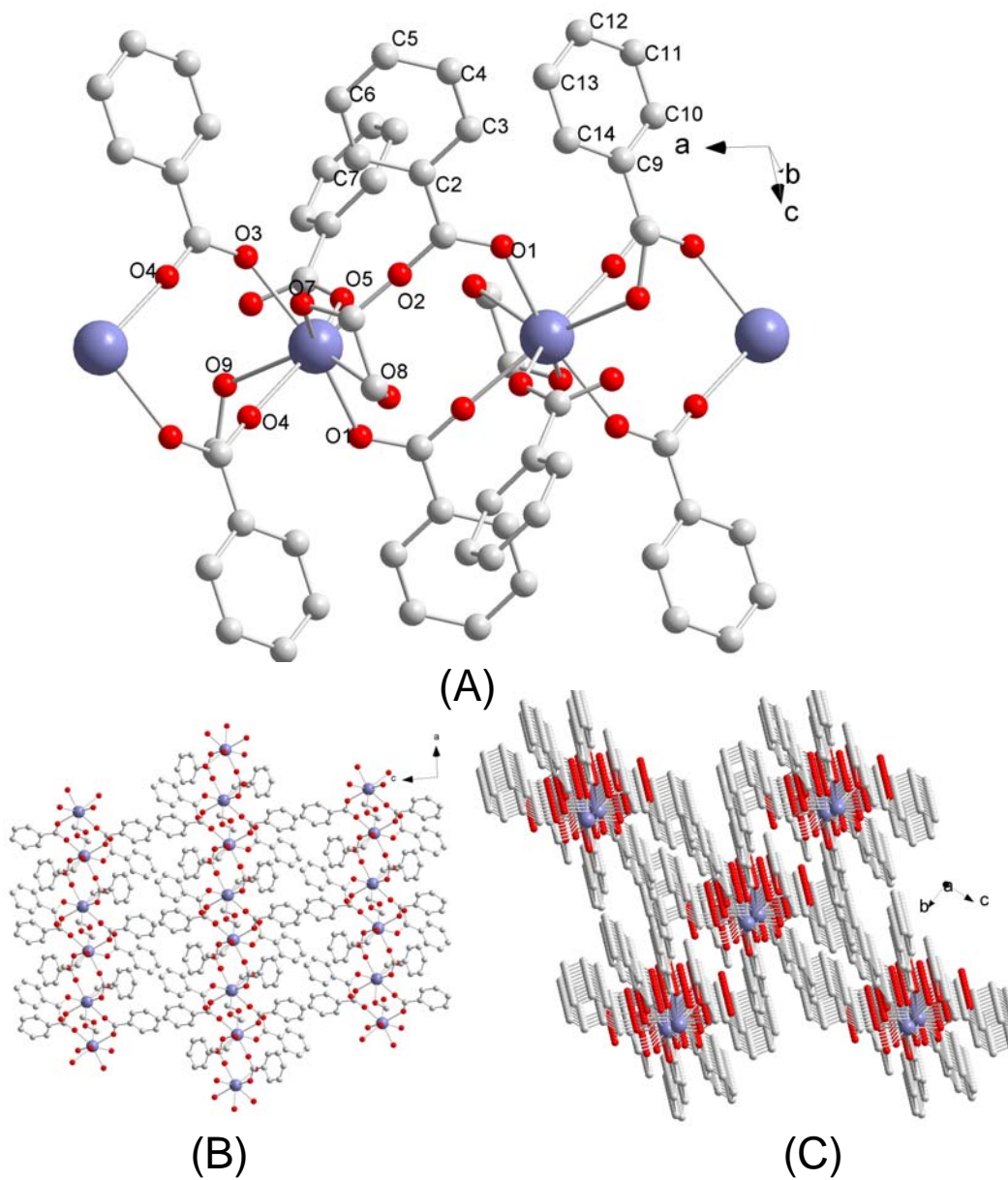


Figure 4.1: Structural view of a fragment of $[\text{Gd}(\text{PhCOO})_3(\text{EtglyH}_2)(\text{MeOH})]$, **4.3** (A). The packing diagram of **4.3** viewed along b axis (B) and along a axis (C) with a slight tilt to clarify π - π stacking. Blue, red and grey spheres represent Gd, O, and C atoms, respectively. Hydrogen atoms are not shown for clarity.

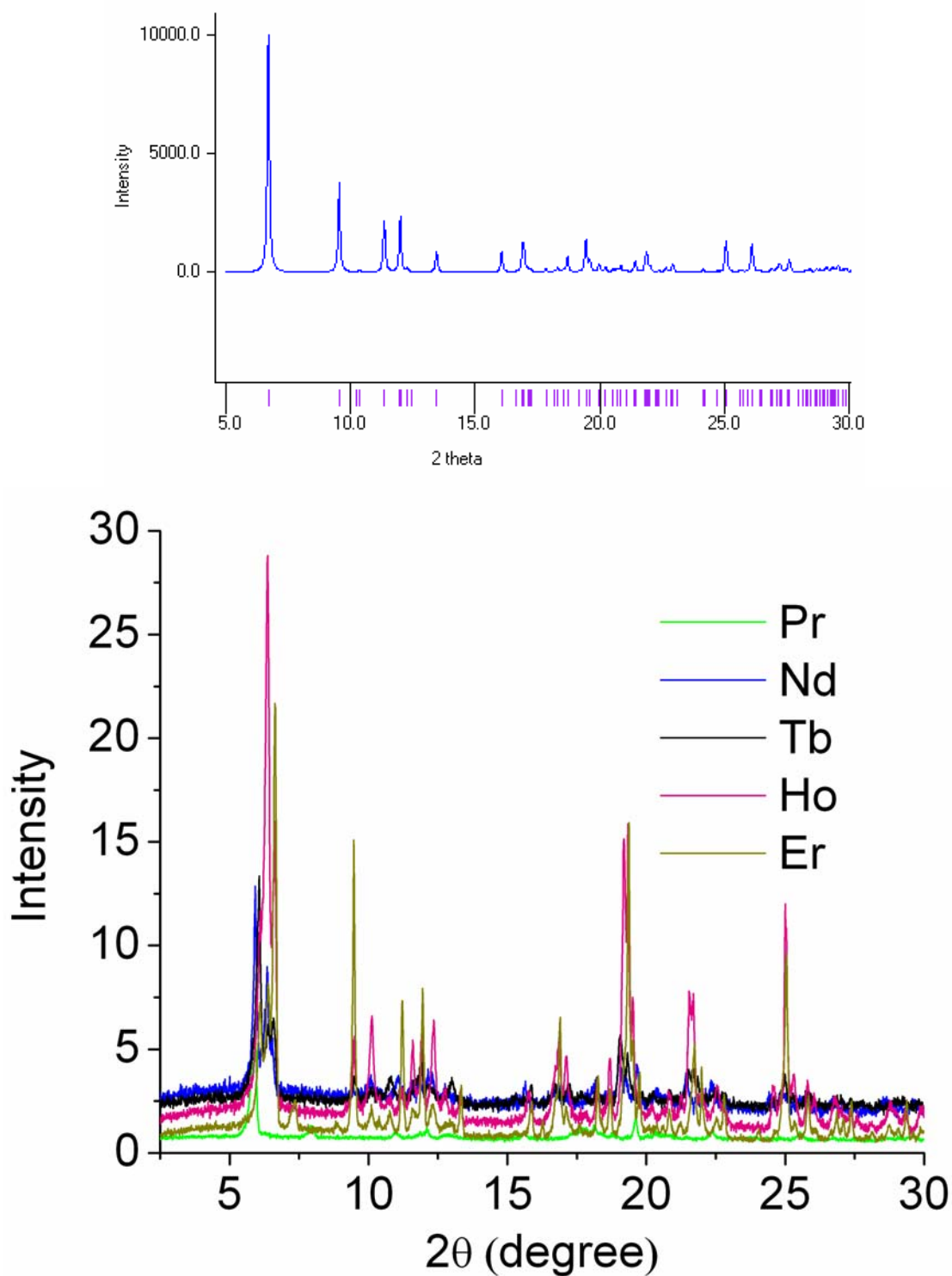


Figure 4.2: The calculated powder XRD pattern for **4.3**. (top) and the powder XRD pattern obtained for **4.1**, **4.2**, **4.4**, **4.6** and **4.7** (bottom). Except for a small difference due to the decrease of ionic radius along the series and/or crystallinity, it can be seen that all compounds are isostructural.

rings of the bridging benzoate ligands. The inter-chain distances between two metal centers were found to be 13.173 Å along the *ac*-plane, and 10.376 Å along the *ab*-plane. These large inter-chain distances should result in minimal inter-chain magnetic interaction and thus to satisfy the second criterion of a SCM.¹⁰⁶

4.2.2. Magnetic properties. Magnetic measurements were carried out on polycrystalline samples for all of the compounds using a SQUID MPMS instrument which operates between 1.8 and 300 K with a magnetic field range up to 70 kOe.

The magnetic behavior of each of the compounds is very similar, but the Dy compound (4.5) exhibits slow relaxation.

4.2.2.1. Temperature dependence of susceptibility. The temperature dependences of the magnetic susceptibilities of these compounds have the same thermal evolution in the range of 1.8-300 K. On decreasing the temperature, the χT product at 1000 Oe continuously decreases from room temperature till 1.8 K. In transition metal compounds, such behavior is typically due to dominant AF interactions. Because these are lanthanide compounds, the Stark sublevels must be taken into account. These sublevels of the anisotropic Ln^{III} (Pr, Nd, Dy, Tb, Ho and Er) ions are thermally depopulated when the temperature is lowered resulting in a decrease of the χT product.¹⁰⁷ As a result, it is not possible to determine whether the decreasing in χT with decreasing T is associated with dominant antiferromagnetic interactions between the Ln^{III} ions within the complexes or with the Ln^{III} ions themselves.

[Pr(PhCOO)₃(EtglyH₂)(MeOH)], 4.1: At 300 K, the χT value is about 1.42 cm³Kmol⁻¹ (Figure 4.3), which is close to the expected value of 1.60 cm³Kmol⁻¹ ($g = 4/5$) for a Pr³⁺ metal ion with a $4f^2$ electronic configuration and a ³H₄ ground state term symbol.¹⁰⁸ With decreasing temperature, the χT product at 1000 Oe continuously decreases to reach 0.05 cm³Kmol⁻¹ at 1.8 K.

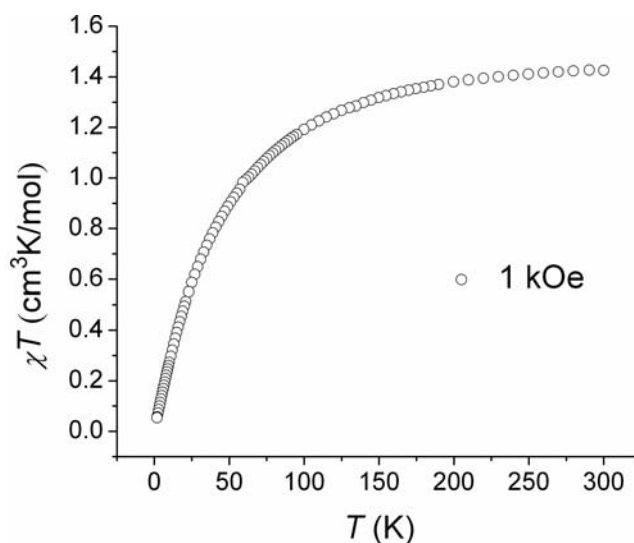


Figure 4.3: χT versus T plot for $[\text{Pr}(\text{PhCOO})_3(\text{EtglyH}_2)(\text{MeOH})]$ chain **4.1** using an applied field of 1 kOe.

$[\text{Nd}(\text{PhCOO})_3(\text{EtglyH}_2)(\text{MeOH})]$, **4.2:**

From the susceptibility measurements (Figure 4.4), it can be observed that at the room temperature the χT value is $1.64 \text{ cm}^3\text{Kmol}^{-1}$, which matches the expected value ($g = 8/11$) for an ion with a $4f^3$ electronic configuration and a $^4I_{9/2}$ ground state term symbol.¹⁰⁸ With decreasing the temperature, the χT product at 1000 Oe continuously decreases to reach $0.62 \text{ cm}^3\text{Kmol}^{-1}$ at 1.8 K.

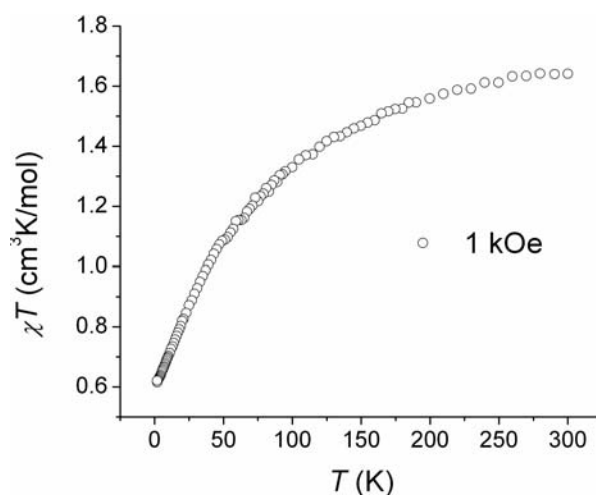


Figure 4.4: χT versus T plot for $[\text{Nd}(\text{PhCOO})_3(\text{EtglyH}_2)(\text{MeOH})]$ chain, **4.2**, using an applied field of 1 kOe.

$[\text{Gd}(\text{PhCOO})_3(\text{EtglyH}_2)(\text{MeOH})]$, **4.3:**

At room temperature, the susceptibility measurements show (Figure 4.5) a χT value of $7.83 \text{ cm}^3\text{Kmol}^{-1}$ which is in good agreement

with the expected value for non-interacting Gd^{3+} ions ($7.94 \text{ cm}^3\text{Kmol}^{-1}$), which has a $4f^7$ electronic configuration and an $^8S_{7/2}$ ground state.¹⁰⁸ The value remains roughly constant until 5 K where an abrupt decrease in χT is observed. It reaches a value of $5.2 \text{ cm}^3\text{Kmol}^{-1}$ at 1.8 K.

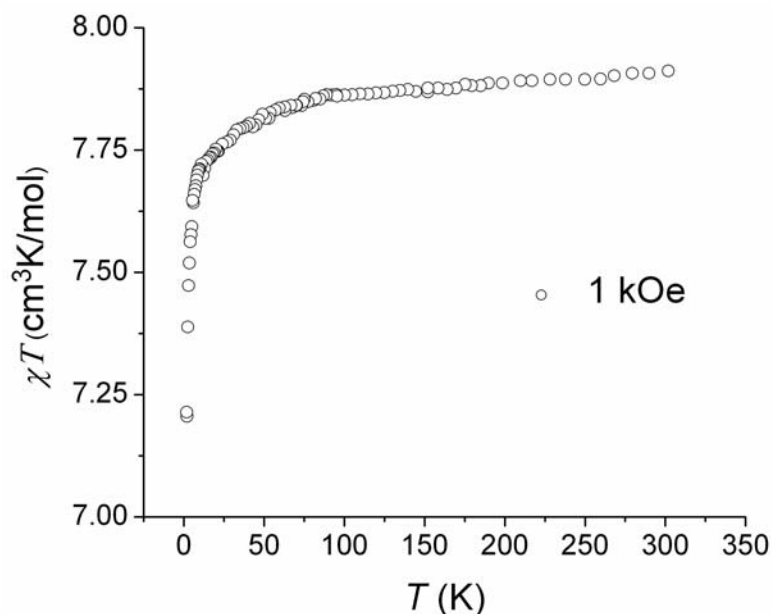


Figure 4.5: χT versus T plot for $[\text{Gd}(\text{PhCOO})_3(\text{EtglyH}_2)(\text{MeOH})]$ chain, **4.3**, at the magnetic field of 1 kOe.

$[\text{Tb}(\text{PhCOO})_3(\text{EtglyH}_2)(\text{MeOH})]$, **4.4:** The susceptibility measurement shows a χT value of $11.74 \text{ cm}^3\text{Kmol}^{-1}$ at room temperature (Figure 4.6). This is in close agreement with the expected value of $11.82 \text{ cm}^3\text{Kmol}^{-1}$ ($g = 3/2$) for an isolated Tb^{3+} metal ion with a $4f^8$ spin configuration and a ground-state term symbol 7F_6 .¹⁰⁸ The χT value remains roughly constant for a long temperature range, and then it starts to drop down around 100 K. At 1.8 K, the large χT product reaches the value of $5.79 \text{ cm}^3\text{Kmol}^{-1}$.

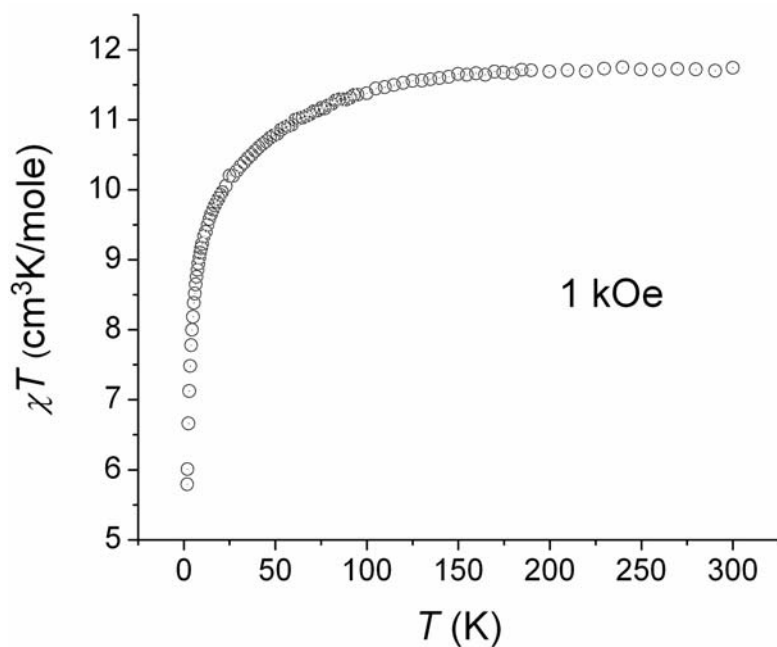


Figure 4.6: χT versus T plot for $[\text{Tb}(\text{PhCOO})_3(\text{EtglyH}_2)(\text{MeOH})]$ chain, **4.4**, at the magnetic field of 1 kOe.

$[\text{Dy}(\text{PhCOO})_3(\text{EtglyH}_2)(\text{MeOH})]$, **4.5:** The χT versus T data for **4.5** were collected with an applied field of 1 kOe (Figure 4.7, A). At room temperature, the χT value was found to be $14.64 \text{ cm}^3\text{Kmol}^{-1}$, which is almost in agreement with the expected value for magnetically non-interacting Dy^{3+} ions ($14.17 \text{ cm}^3\text{Kmol}^{-1}$) with a ${}^6H_{5/2}$ ground state and a $4f^9$ electronic configuration.¹⁰⁸ The value remains roughly constant until approximately 100 K reaching a minima at 12.32 before it starts to drop down around 100 K to reach the minima at $12.32 \text{ cm}^3\text{Kmol}^{-1}$ at 12 K. The χT value then increases abruptly reaching $14.6 \text{ cm}^3\text{Kmol}^{-1}$ at 1.8 K. This increase in the χT value indicates the presence of some ferrimagnetic interaction between the metal centers below 12 K.

The temperature dependence of the imaginary χ'' and real χ' components of the ac-susceptibility were measured at various frequencies between 100 Hz and 1500 Hz. Although the intensity-ratio is quite high, the frequency dependence of the χ'' (Figure 4.7, B) indicates slow relaxation of magnetization. Compound **4.5** may, therefore, be a SCM because it fulfils

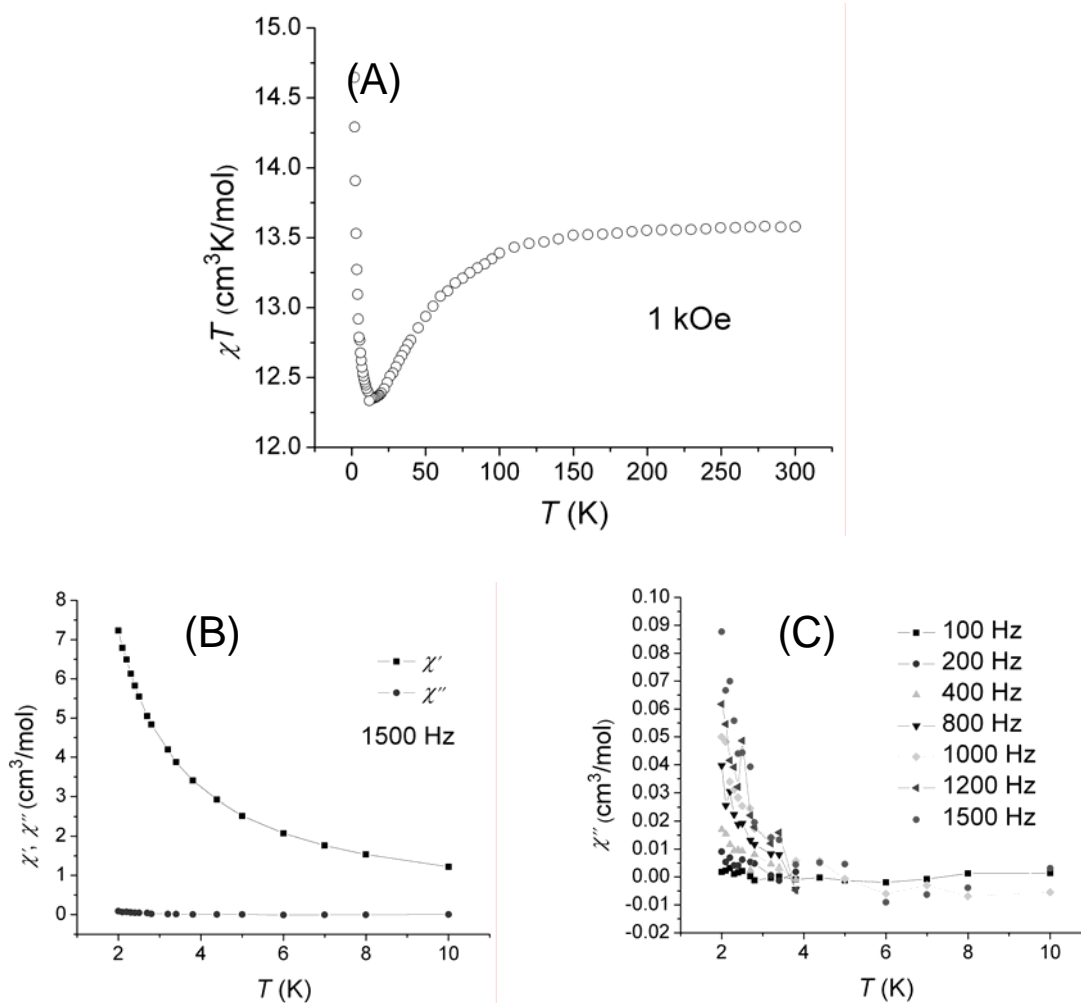


Figure 4.7: Magnetic data recorded for $[\text{Dy}(\text{PhCOO})_3(\text{EtglyH}_2)(\text{MeOH})]$ chain **4.5**, on a polycrystalline sample. (A) χT versus T plot at the magnetic field 1 kOe. (B) temperature dependent ac and dc susceptibility plot. (C) Frequency dependence out of phase ac susceptibility is shown.

both of the following criteria. Firstly, it has some Ising anisotropy of the magnetic center, and secondly, the inter-chain distances are very large (more than 10 Å) due to the presence of aromatic layers between the chains. This helps to reduce the inter-chain magnetic interaction which is a main requirement of a SCM.

$[\text{Ho}(\text{PhCOO})_3(\text{EtglyH}_2)(\text{MeOH})]$, **4.6:** The χT versus T data for **4.6** was collected with an applied field of 1 kOe (Figure 4.8). At room temperature the, χT value was found to be 13.25 cm³Kmol⁻¹ which is less than the expected value (14.07 cm³Kmol⁻¹, $g = 5/4$) for

magnetically non-interacting Ho^{3+} ions with a $4f^{10}$ electronic configuration and a ground-state term symbol of 5I_8 .¹⁰⁸ This value does not change significantly until 140 K where the curve starts to drop slowly. This is followed by a steep decrease around 15 K, and at 1.8 K it reaches a value of $8.61 \text{ cm}^3\text{Kmol}^{-1}$.

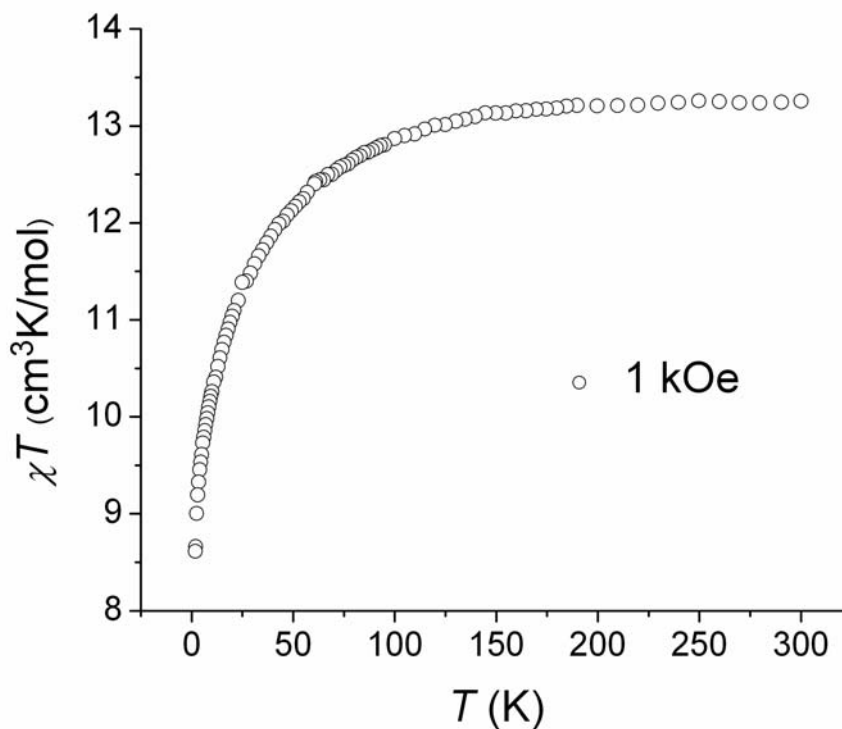


Figure 4.8: χT versus T plot for $[\text{Ho}(\text{PhCOO})_3(\text{EtglyH}_2)(\text{MeOH})]$ chain, **4.6**, at the magnetic field 1 kOe.

$[\text{Er}(\text{PhCOO})_3(\text{EtglyH}_2)(\text{MeOH})]$, **4.7:** The susceptibility was measured using an applied field of 1 kOe. From the χT versus T plot (Figure 4.9), it can be seen that at room temperature the χT value is about $11.47 \text{ cm}^3\text{Kmol}^{-1}$, which is almost in agreement with the expected value for an isolated Er^{3+} ion ($11.48 \text{ cm}^3\text{Kmol}^{-1}$, $g = 6/5$) which has an electronic configuration of $4f^{11}$ and a ground-state term symbol $^4I_{15/2}$.¹⁰⁸ From the plot, it can be seen

that after reaching the minima at 5 K ($8 \text{ cm}^3\text{Kmol}^{-1}$), the χT value starts to increase sharply and it reaches about $9.3 \text{ cm}^3\text{Kmol}^{-1}$ at 1.85 K. This increase may come from some ferromagnetic interaction at very low temperature range and/or from some untraceable impurities.

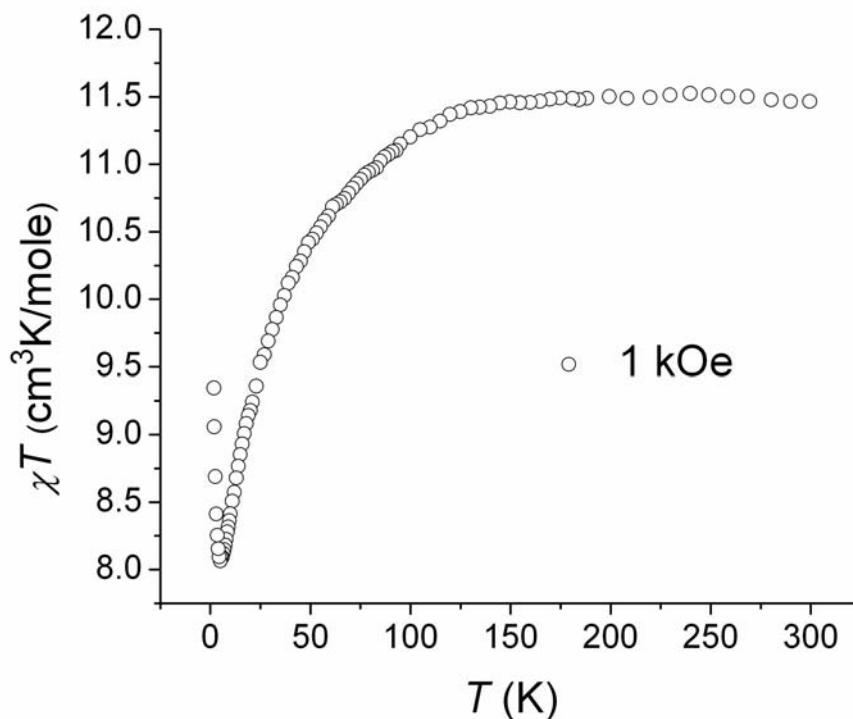


Figure 4.9: χT versus T plot at a magnetic field of 1 kOe for $[\text{Er}(\text{PhCOO})_3(\text{EtglyH}_2)(\text{MeOH})]$ chain, **4.7**.

Magnetic susceptibilities of all the compounds are summarized in table 4.2. It can be seen that the experimental values are in close agreement with the expected values. The χT values of the isolated ions and that expected for the corresponding compounds are similar because of the mononuclear repeating unit of the chain. This observation is in good agreement with the very weak magnetic coupling between the metal centers which are separated by more than 5.5 \AA .

Compounds	χT (cm ³ K/mol) expected for each Ln ³⁺ at RT	χT (cm ³ K/mol) expected for compounds at RT	χT (cm ³ K/mol) measured for compounds at RT	Ground state term symbols for the Ln ³⁺ ions
[Pr(PhCOO) ₃ (EtglyH ₂)(MeOH)], 4.1	1.60	1.60	1.42	³ H ₄
[Nd(PhCOO) ₃ (EtglyH ₂)(MeOH)], 4.2	1.64	1.64	1.64	⁴ I _{9/2}
[Gd(PhCOO) ₃ (EtglyH ₂)(MeOH)], 4.3	7.94	7.94	7.83	⁸ S _{7/2}
[Tb(PhCOO) ₃ (EtglyH ₂)(MeOH)], 4.4	11.81	11.81	11.74	⁷ F ₆
[Dy(PhCOO) ₃ (EtglyH ₂)(MeOH)], 4.5	14.18	14.18	14.64	⁶ H _{5/2}
[Ho(PhCOO) ₃ (EtglyH ₂)(MeOH)], 4.6	14.05	14.05	13.25	⁵ I ₈
[Er(PhCOO) ₃ (EtglyH ₂)(MeOH)], 4.7	11.47	11.47	11.47	⁴ I _{15/2}

Table 4.2: A comparison of the susceptibility data for the isostructural chain compounds is shown.¹⁰⁸

4.2.2.2. Field dependence of magnetization. The field dependence of the magnetization at low temperatures shows that the magnetization smoothly increases with the applied dc field, and at 7 kOe it reaches the value of 0.35, 1.43, 7.121, 4.87, 6.36, 5.35 and 6.26 μ_B , for **4.1**, **4.2**, **4.3**, **4.4**, **4.5**, **4.6** and **4.7**, respectively (Figure 4.10). In only the Gd and Tb chains (**4.3** and **4.4**) does the magnetization reach complete saturation. In all other compounds, a slight slope was observed in each temperature at a high field of 7 kOe. This indicates that compounds **4.1**, **4.2**, **4.5**, **4.6** and **4.7** possess some magnetic anisotropy and/or low-lying excited states. For further information, M versus H/T (Figure 4.11) were plotted. Superposed curves were observed for **4.3** and **4.4**, confirming their isotropic nature. In the other compounds (**4.1**, **4.2**, **4.5**, **4.6** and **4.7**), the curves at different temperatures are not superposed. This also indicates that these compounds are anisotropic and/or they have low-lying excited states which are easily populated at higher fields.

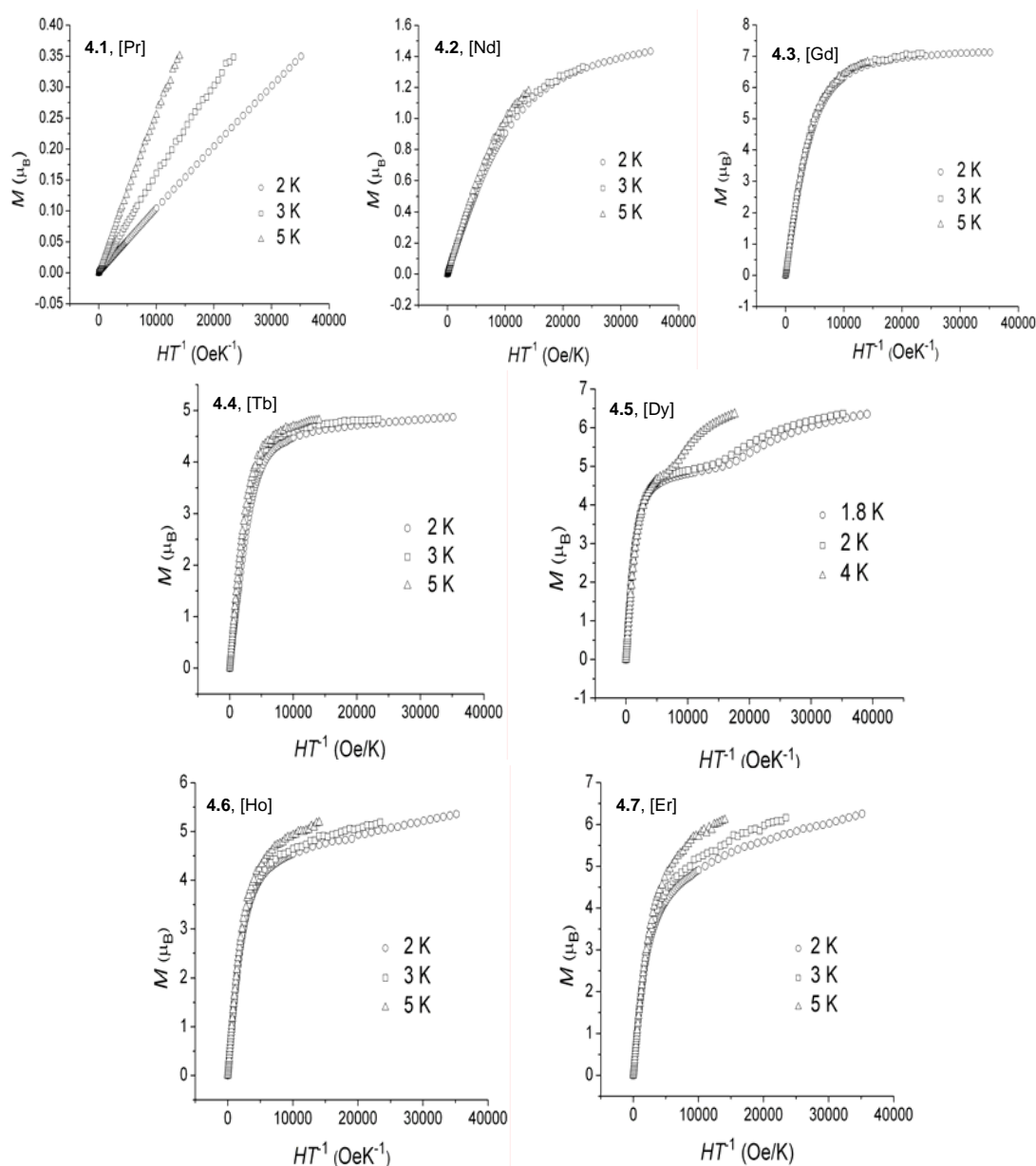


Figure 4.11: The M versus HT^{-1} plots for 4.1 - 4.7.

4.2.2.3. Fitting of the magnetic data for 4.3. Gadolinium(III), with a ground $^8S_{7/2}$ term, has no orbital contribution and therefore can be considered to have an isotropic $S = 7/2$ spin. Based on the structure, therefore, the compound can be viewed as a Gd^{III} ($S = 7/2$) chain with interactions mediated by *syn-anti* carboxylate bridge. A regular antiferromagnetic spin ($S =$

$7/2$) chain model was used to fit the magnetic susceptibility and to obtain the magnetic interaction, J , between the Gd^{III} sites through the *syn-anti* carboxylate bridge. The Hamiltonian used was

$$H = -2J \sum_i S_i S_{i+1}$$

where S_i and S_{i+1} are the spins of two interacting metal ions respectively.¹⁰⁹

Fitting of the data gives $g = 2.00(1)$ and $J/k_B = -0.0156(2)$ K (Figure 4.17), in which the data are well reproduced down to 1.8 K.

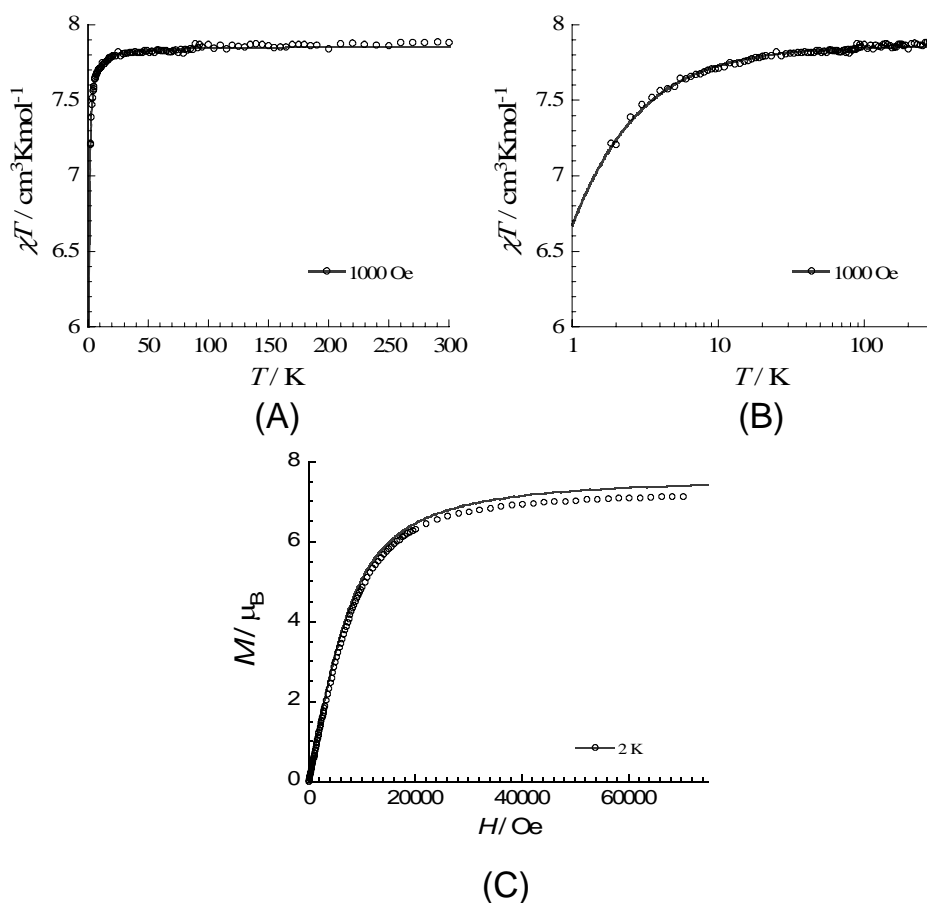


Figure 4.12: (A, B) Magnetic susceptibility data (circles) of compound **4.3** and the best fits (solid lines). Plot of the calculated Brillouin function (solid curve) and experimental magnetization data for compound **4.3**.

The Brillouin function ($g = 2$ and $S = 7/2$) was calculated as the solid line in the plot above (Figure 4.18). Magnetization data was also compared to the calculated Brillouin

function for $g = 2$ and $S = 7/2$. Since the experimental curve is very similar to the calculated curve, the interactions between the metal centers must be very weak. The slight low values of M indicate very weak antiferromagnetic coupling and smaller J value though. Since all the compounds are isostructural, the magnetic interactions between the metal ions in other compounds are also likely to be very weak. This is often the case for lanthanide systems as has recently been shown for an isostructural series of the lanthanides dimmers.

4.3. Summary

From this work, it has been shown that poly-alkoxy ligands can be used to design lanthanide compounds that may be magnetically interesting as seen for the transition metal compounds in the Chapter 3. Carboxylate moieties together with poly-alkoxy ligands gave rise to several new lanthanide compounds resulting in a new class of 1D chain compounds. The very similar chemical properties of the lanthanides made it possible to incorporate various metal centers into a specific type of 1D compound. This made it possible to tune their magnetic properties, which were in close agreement with the expected behavior. A brief comparison of the susceptibility studies is summarized in Table 4.2. Compound **4.3**, which exhibits slow relaxation of magnetization at very low temperature and has a large inter-chain distance, may be a SCM and will be the subject of further study.

CHAPTER 5

Control over biomineralization of CaCO_3 using simple organic templates

General Introduction:

The high degree of control over form and function observed in biominerals is a source of wonder and inspiration to biologists and materials scientists' alike.¹¹⁰ Calcium carbonate is one such biomineral ubiquitous in Nature. The large amounts of calcium carbonate found in coccolithophoridae, mollusc shells and corals in aquatic environments represent a major means of fixing and storing carbon dioxide. Hence, the formation and utilization of calcium carbonate are not only important in biology but also in environmental and industrial contexts.^{111, 112, 113, 114} There are three main kinds of crystalline polymorphs of CaCO_3 , viz. calcite, aragonite and vaterite.¹¹⁵ Among these three crystalline polymorphs, calcite is the most thermodynamically stable and most abundant in nature, whereas vaterite is the most unstable and rarely found.¹¹⁶ Biological systems deposit calcium carbonate in the presence of different kinds of organic substrates. It has been widely investigated and accepted that in cases where organisms produce highly specific structures, such as shells, teeth and bones, complicated templating organic molecules, such as polysaccharides and protein matrices, play very important roles.¹¹⁷⁻¹¹⁹

In the case of calcium carbonate biominerals, compounds with carboxylic acid groups are likely to direct the mineralization process through the carboxylate moieties occupying carbonate sites during crystal growth. By doing this, they direct the evolving morphology to produce a desired phase, shape and functionality. Understanding how these processes operate is important not only

from the biological perspective, but also in the context of preparing synthetic biomaterials with desired shapes and functions. The effects of a few amino acids on biomineralization of CaCO_3 have also been studied.¹¹⁹ For example, in a recent study on calcium carbonate formation in the presence of aspartic acid, it was shown that the amino acid chirality has an enormous effect on how the calcite morphology evolves, starting at the atomic level leading to the chiral modification of step edges of crystal faces at the mesoscopic level.¹²¹ The biominerals generally form in an organic matrix assisted by the presence of proteins rich in aspartic acid and glutamic acid. To mimic such process, recently, polymer molecules containing amino acids are being used in biomineralization research. Addadi *et al.* have shown that the formation of a specific polymorph of CaCO_3 in mollusc shells depends on the macromolecular microenvironment and on the amino acid sequences and conformations of the polypeptides.^{122, 123} When designed α -helical peptides with an array of aspartyl residues were applied in biomineralization of CaCO_3 , selective recognition and binding to the prism faces of the calcite had been observed to produce crystals with characteristic shapes.¹²⁴ For example, sponge-like morphologies of calcite crystals have been obtained by using sponge-like polymer membranes as templates.¹²⁵ The effects of polysaccharides and collagen over the modification of calcite growth have also been studied.^{126, 127} The incorporation of polysaccharide produced round and smooth-surfaced calcite crystals, but, in contrast, incorporation of collagen hampered the growth of any particular face. Recently, it has also been observed that the acid concentration can influence directly the produced crystal phase. When malonate, succinate, glutarate, and adipate were used as templating agents, the variation of temperature and concentration gave rise to different polymorphs of CaCO_3 .¹²⁸ Biomineralization of CaCO_3 has also been studied with more complicated template systems, such as mixture of dendrimers and surfactants.¹²⁹ In this case, deposition of the CaCO_3 was controlled by the addition of different surfactants. Recently, synthetic polymers are receiving much attention for their characteristic

influence over the CaCO_3 crystal growth. Much more complicated systems like, “double hydrophilic block copolymer”, “Langmuir-monolayer”, and “polymerized Langmuir-Blodgett film” have been also applied for control over CaCO_3 crystal growth.¹³⁰⁻¹³³

The aim of this work was to apply simple carboxyl-rich templates rather than the usual complex organic templates in the biomineralization of calcium carbonate to understand and rationalize the structure-controlling factors. Most of the templates used in this investigation already have well-established coordination chemistry.¹³⁴ The aim was to get some clues from coordination chemistry about the templated growth of CaCO_3 to rationalize the controlled formation of biominerals. Unfortunately, the very low concentration of the templates in the biomineralization process becomes a major problem in such a goal. On the other hand, the rigid geometry of the benzene polycarboxylic acids (BDC; benzene dicarboxylic acid and BTC; benzene tricarboxylic acid, Figure 5.1) was helpful in rationalizing the shapes of the evolved morphology of the CaCO_3 . In another case, we used the rather flexible hpdtaH₅ (1,3-diamino-2-hydroxypropane-*N,N,N',N'*-tetraacetic acid, Figure 5.1) and the formation pathway of the CaCO_3 morphologies was successfully established using various spectroscopic techniques. It might be noteworthy to mention at this point that the polyalkoxy ligands which were used for the synthesis of high nuclear aggregates of Mn and Fe, were also applied in mineralization of CaCO_3 , but no significant changes were found. Uncontrolled growth of usual calcites was observed.

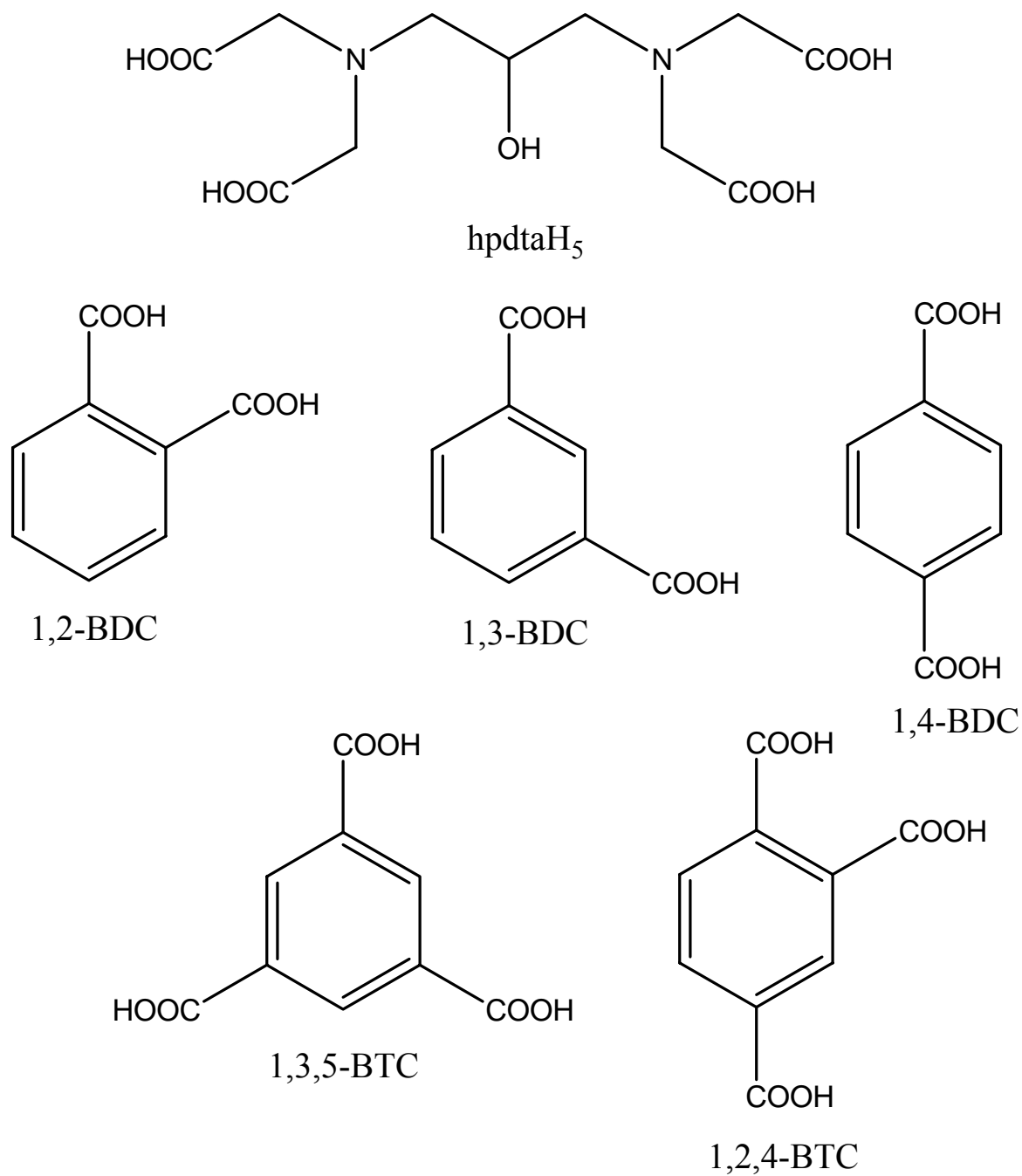


Figure 5.1: Templates used in biomineralization of CaCO_3 : 1,3-diamino-2-hydroxypropane-*N,N,N',N'*-tetraacetic acid (hpdaH₅), 1,2-benzenedicarboxylic acid (1,2-BDC), 1,3-benzenedicarboxylic acid (1,3-BDC), 1,4-benzenedicarboxylic acid (1,4-BDC), 1,3,5-Benzenetricarboxylic acid (1,3,5-BTC), 1,2,4-Benzenetricarboxylic acid (1,2,4-BTC).

5.1. Control over calcite crystal growth using 1,3-diamino-2-hydroxypropane- N,N,N',N' -tetraacetic acid, hpdtAH_5

5.1.1. Introduction

Nature uses various organic substrates as templates for the nucleation and growth of different kinds of inorganic biomaterials.¹¹⁰ Organic substrates with carboxylate groups play an important role in the nucleation of these materials. It was observed that hpdtAH_5 (1,3-diamino-2-hydroxypropane- N,N,N',N' -tetraacetic acid) is an important template for CaCO_3 mineralization. It produces a microtrumpet-like morphology (Figure 5.2) which is very similar to the structural unit found in biological coccolithophore *Discosphaera Tubifera* (Figure 5.3). The system was studied in detail to determine the probable pathway for the formation of these microtrumpet structures. The nucleation pattern of CaCO_3 was studied also by varying pH in the presence of hpdtAH_5 . Being a heptadentate ligand and having different functional groups, hpdtAH_5 is an appropriate candidate for playing with the functionality of its different groups by varying the pH factor. More clearly, the carboxylate and the hydroxyl groups in hpdtAH_5 play different roles at different pHs of the medium. The biomineralization process was also investigated using various surfaces.

When calcium carbonate was allowed to precipitate in the presence of small amounts of the polycarboxylate at a pH value of 7.9, the formation of microtrumpets of calcite (**5.1**, Figure 5.2), bearing a striking resemblance to the trumpet-like structures found on the coccolithophore *Discosphaera Tubifera* (Figure 5.3) occurred.¹³⁵ This finding raised a number of questions regarding the important parameters governing the growth process of these structures. The polycarboxylate used here, is a much simpler molecule than the additives usually studied in mimicking biomineralization processes found in literature.^{122-125, 129-133} Moreover, a much simpler procedure was followed compared to that used for the templating molecules or matrix environments regarded

as the key to stabilizing the kinetic crystal growth found throughout nature. This poses the question as to how hpdtaH₅ interacts at the phase boundary between solid-state calcium carbonate and the aqueous solution. After the polycarboxylate-to-calcium ratio for the microtrumpet formation was optimized, the system was examined by varying the concentration, the pH, and the surface types. This is the first time the effect of surface type over biomineralization has been systematically investigated.

5.1.2. Results and discussion

The time-dependent study of the microtrumpet formation is shown in Figure 5.2. The SEM image of the calcium carbonate deposited after 6 hours is shown in Figure 5.2A. The phase was

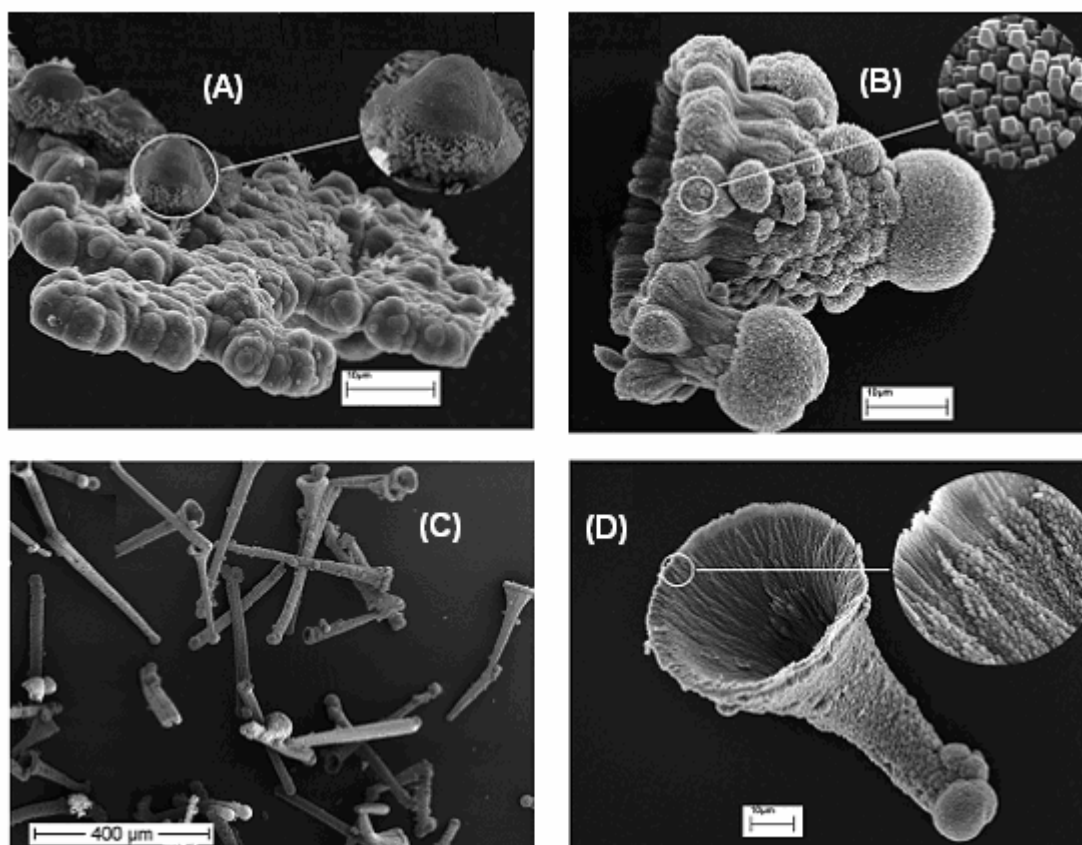


Figure 5.2: SEM images of calcite formation (A) after 6 h, (B) after 12 h, (C) after 24 h, (D) close-up of a microtrumpet (5.1) formed after 24 h.¹⁹ Scale bar: A, B, D (10 μm), C (400 μm).

characterized as amorphous calcium carbonate (ACC) by infrared spectra and powder XRD (Figure 5.4) with the presence of characteristic IR peaks of ACC at 873, 1074, 1418 and 1474 cm^{-1} and the high baseline of the XRD spectra respectively.¹³⁶ This indicates the presence of ACC at the early stage of microtrumpet formation. ACC plays an important role as a precursor in most of the biological CaCO_3 deposition. With time, the growth of the trumpet-wall was observed with dumbbell-shaped building units (Figure 5.2B) organizing into a bobble-hat motif. It takes about 24 hours to form a complete microtrumpet (Figure 5.2D).

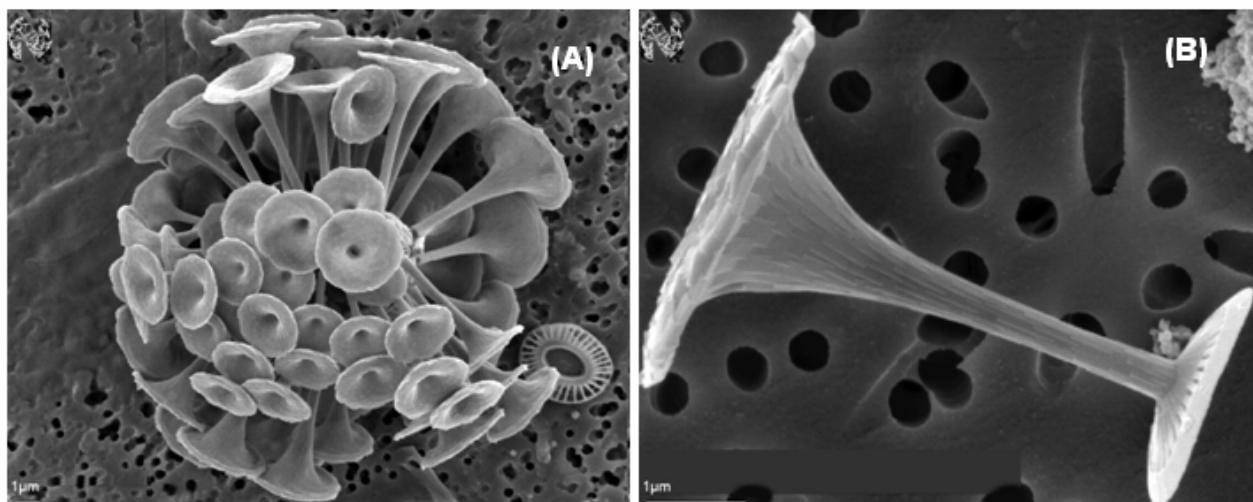


Figure 5.3: (A) A complete view of *Discophaera Tubifera*. (B) The trumpet-like unit of the *Discophaera Tubifera*.

The surface-dependence of these structures has unraveled a new insight into the biomineralization process. From the pH dependence and concentration dependence studies it has been observed that small change in these parameters bring considerable changes in the evolved morphology of calcium carbonate mesostructures.

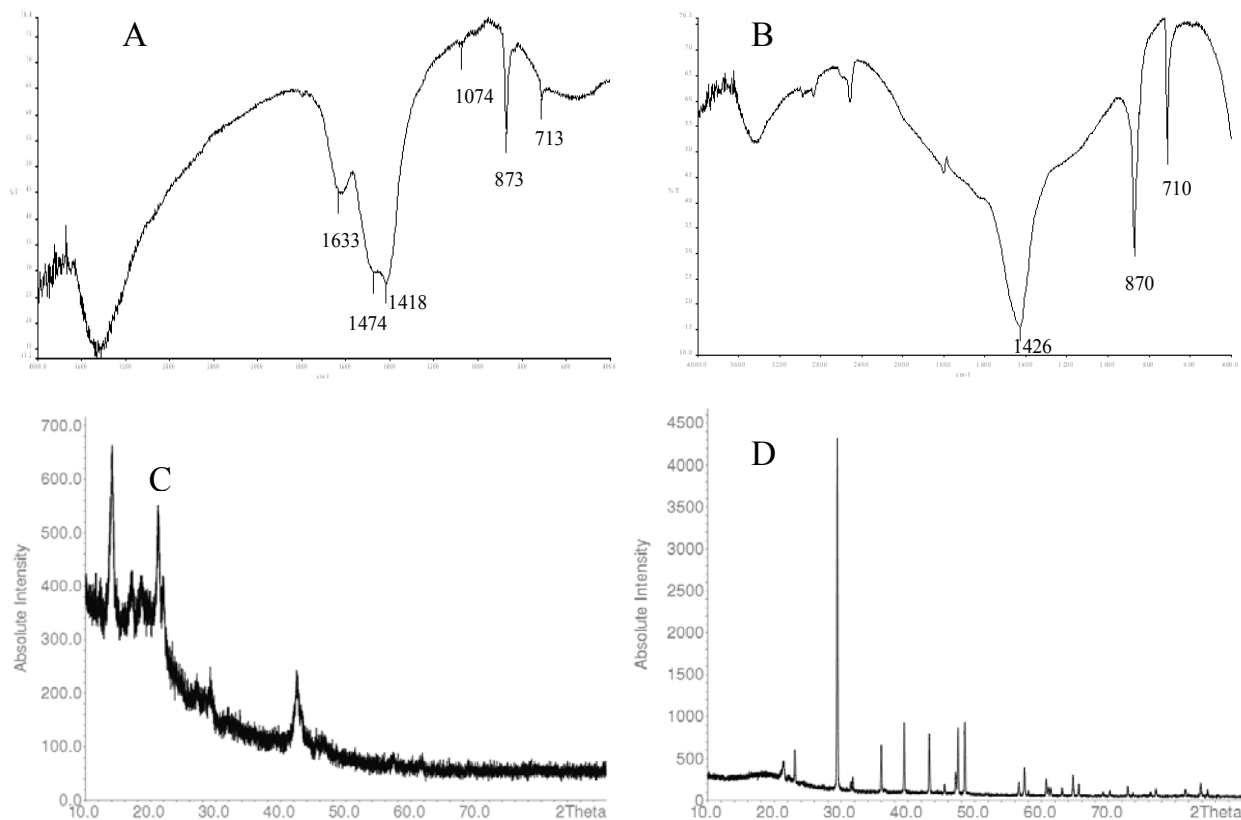


Figure 5.4: (A) The IR spectra of the precursor of the microtrumpets collected after 1 hour is shows the characteristic peaks of ACC (873, 1074, 1418 and 1474 cm^{-1}). (B) Characteristic IR peaks of calcite(710, 870 and 1426 cm^{-1}) obtained from the sample collected after 24 hours. (C) The powder XRD pattern obtained from the precursor of the trumpets (after 6 hours of reaction time). Height of the baseline indicates the presence of ACC. (D) Represents characteristic peaks (at 2θ values of 30, 36, 40, 44, 48, 50) of calcite in powder XRD pattern after formation of the complete trumpets (24 hours).

5.1.2.1. Surface dependence:

The mineralization process was studied on different kinds of surfaces *viz.* glass, silicon, plastic, and quartz. Interestingly, it was found that the microtrumpet-like structure forms exclusively on glass. Maintaining all the same conditions, dumbbell-shaped structures (5.2) were found on the other kinds of surfaces (Figure 5.5C). From a close-up view of the calcite microtrumpets, it can be seen that the wall of the microtrumpet is constituted of small dumbbell-shaped units (Figure 5.6A, B). The dumbbells are arranged in a cross-hand pattern (Figure 5.6C, D) on the microtrumpet wall. As a result, the microtrumpets are mainly formed of two parts: the bobble-hat motif and the

organized calcite-dumbbells. As bobble-hat motifs were found only on glass, it can be suggested that the formation of this is aided by the negatively charged glass surface.¹³⁷

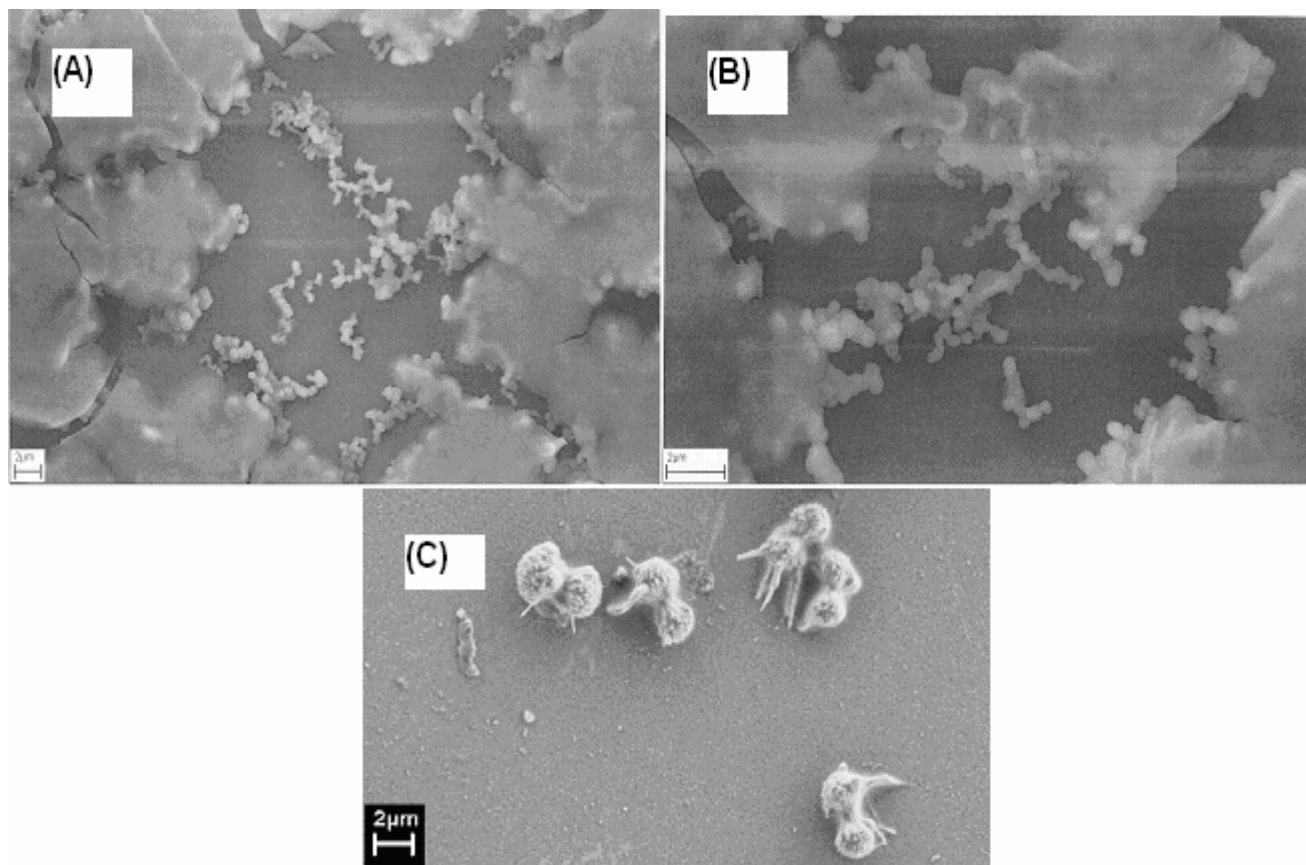


Figure 5.5: The SEM images of the dumbbell-shaped calcite obtained from the solution during the DLS study (A) and B at 60 minutes and 120 minutes respectively) confirm the formation of the dumbbells in solution. Dumbbell-shaped structures deposited on silica (C). large CaCO_3 flakes are present as a result of drying the solution in oven. Scale bar 2 μm .

In contrast, the dumbbell-shaped structures form in the solution and thus they are independent of the surface type. To explore this assumption, DLS study was performed (Figure 5.7), and it was found that the diameter of the particles formed in the solution are very close to the length of the dumbbells present on the microtrumpet-walls (approximately 4 μm). Moreover, it was found that the diameter

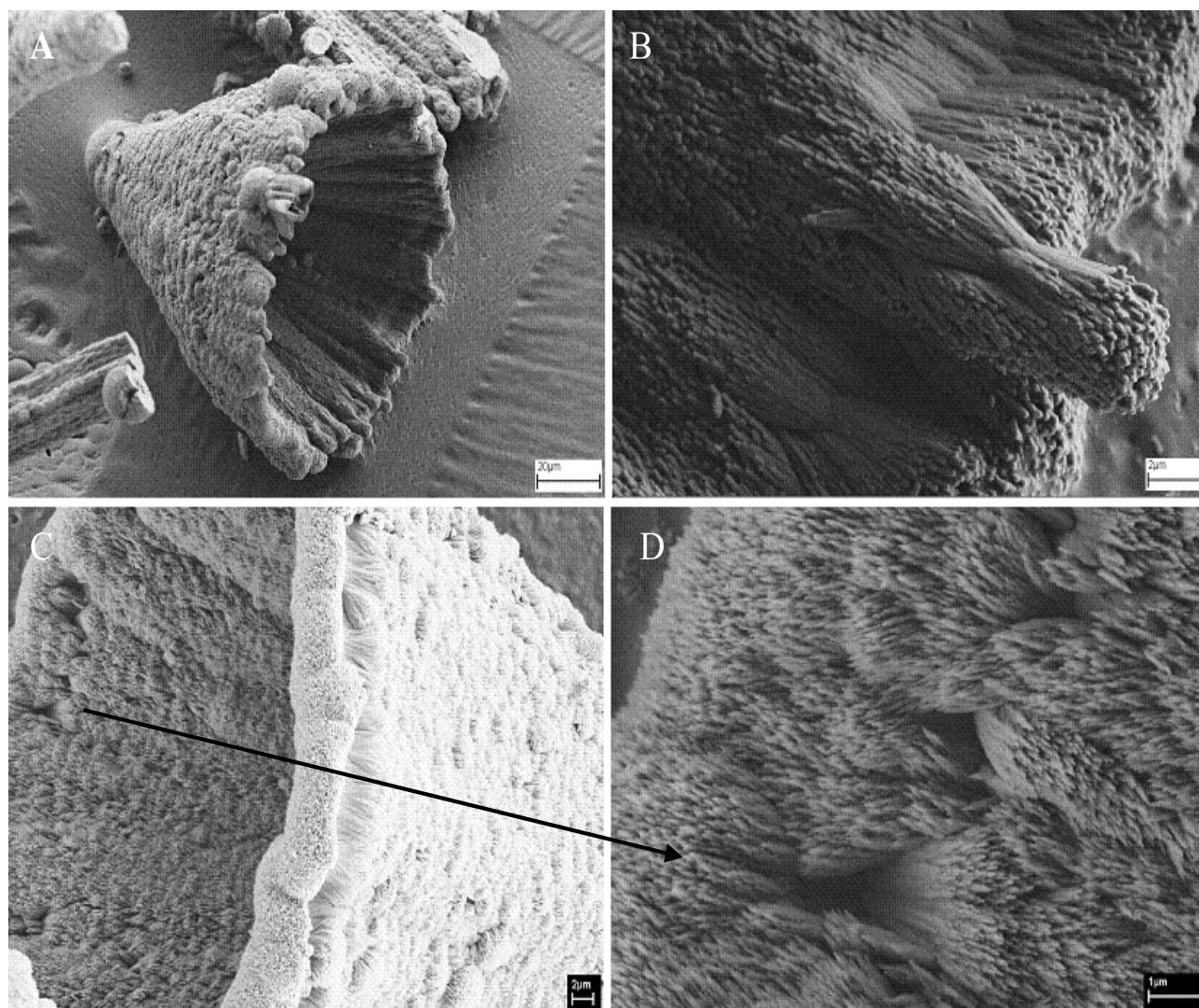


Figure 5.6: (A) A close-up view of the CaCO_3 -microtrumpets; (B) The terminal surface of the microtrumpet showing the dumbbell-shaped units; (C) Close-up view of the wall of the microtrumpet; (D) Cross-hand pattern of the dumbbells on the wall of the microtrumpet. Scale bar A = 20 μm , B and C = 2 μm , D = 1 μm .

of the evolved particles increased rapidly at the beginning, but after 1 hour of reaction no further significant growth was observed. This observation suggests that the dumbbells do not grow further in size, but are deposited to build the walls of the microtrumpets.

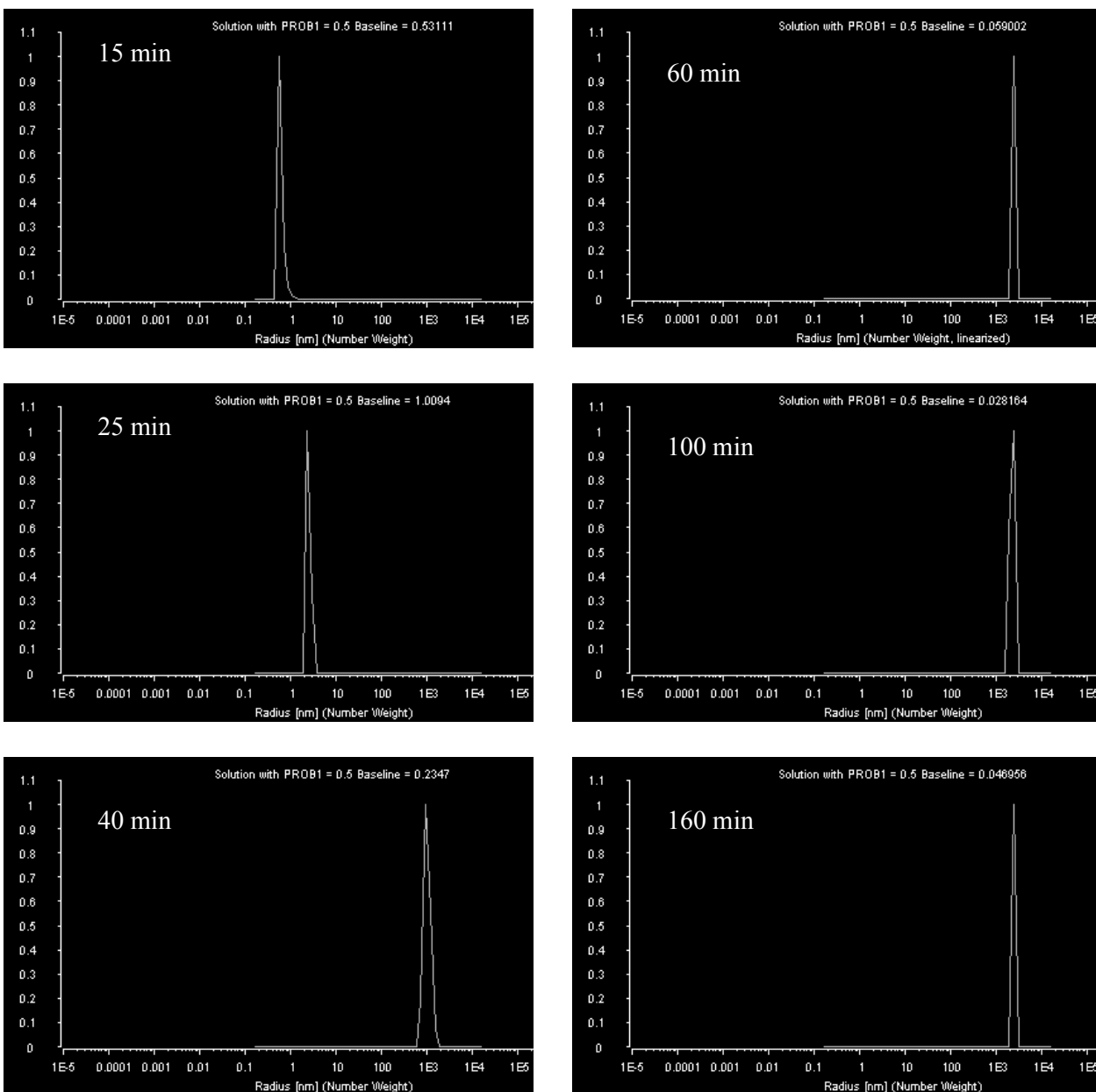


Figure 5.7: The growth of the particle-size in the solution was found by a dynamic light scattering (DLS) study. The vertical axis indicates the normalized quantity and the horizontal axis indicates the hydro dynamic radius of the suspended particle.

A schematic representation is shown in Figure 5.8. To obtain more detailed information, a drop was taken out of the solution at the time of the DLS study and viewed using SEM (Figure 5.5A, B). The drop was first dried in the oven at moderate temperature (60 °C) before placing in the SEM. The presence of dumbbell-shaped units can be observed from the SEM images, but no bobble-hat motifs

were seen, as can be expected from the surface-dependence study. This finding confirms that the bobble-hat motifs do not grow in solution but on the surface. After the dumbbells form in the solution they are deposited on to the bobble-hat units in a “cross-hand pattern” to form the wall of the microtrumpet (Figure 5.6D). Interestingly, based on the powder XRD pattern and IR spectra (Figure 5.4) taken at very early stages, it was found that the precursor of the bobble-hat motif is made of ACC,

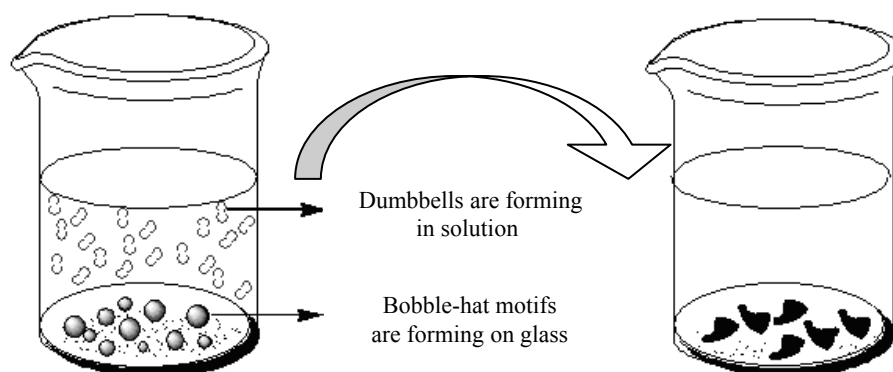


Figure 5.8: Schematic representation of the trumpet formation showing that the bobble-hat motifs are forming on the glass surface and the dumbbell-shaped units are forming in the solution to form trumpets.

5.1.2.2. pH dependence:

Maintaining all the same conditions, the process was studied by adjusting the pH of the medium to 6.25, 7.00, 7.50, 7.75, 8.25 and 8.50 prior to the addition of NaHCO_3 . From the SEM images, a clear trend of change in the nucleation pattern is observed. In Figure 5.9A, the CaCO_3 structure (5.3) obtained at pH 6.50 has a small cavity on either side. Close examination of the surface reveals that the shape is constructed with long crystallites having pentagonal cross-sections. In Figure 5.9B, the SEM image depicts the structures (5.4) obtained at pH 7.00. Here it can be seen that the radial wall of the cavity becomes thicker and the depth of the cavity becomes shallower compared to the structures obtained at lower pH. Figure 5.9C shows the morphology (5.5) obtained

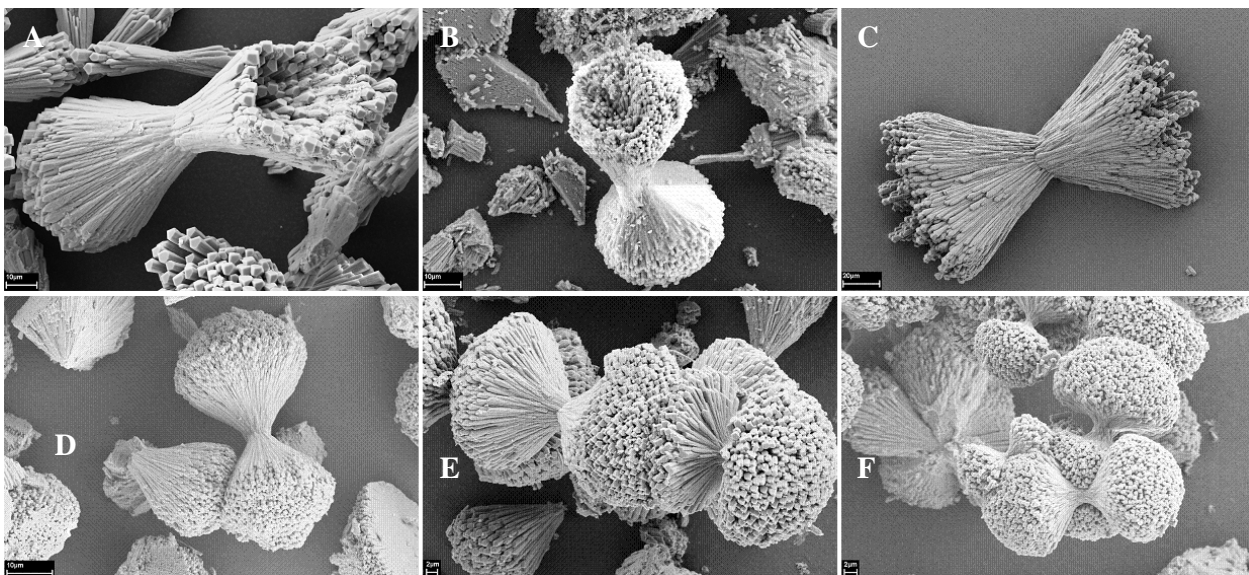


Figure 5.9: SEM images of the calcite dumbbells obtained after 24 hours of mineralization at pH 6.25 (A), pH 7.00 (B), pH 7.50 (C), pH 8.00 (D), pH 8.25 (E) and pH 8.50 (F), respectively. Scale bars A, B and D = 10 μm ; C = 20 μm ; E and F = 2 μm .

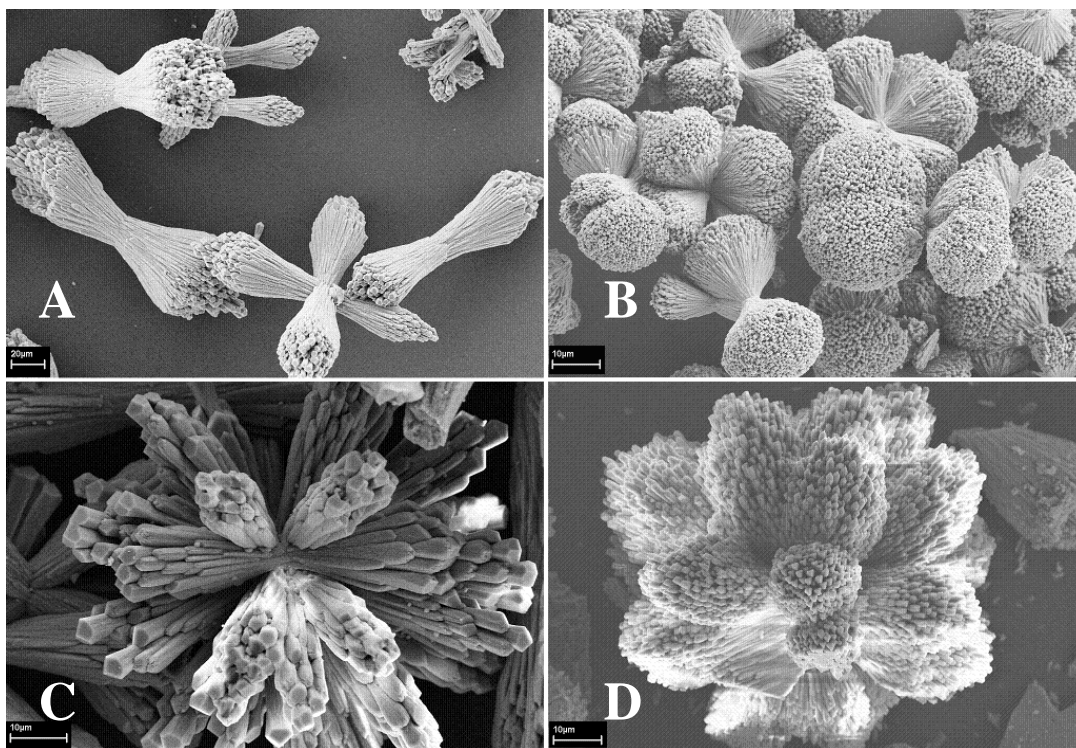


Figure 5.10: Cross-linked structures at pH 8.00 (A, B) and 8.50 (C, D). Scale bars A (20 μm), B, C and D = 10 μm .

at pH 7.50 in which the cavity almost vanishes, and Figure 5.9D indicates the structure (5.6) becomes dumbbell-shaped at pH 7.75. The SEM pictures of the structures (5.7) obtained at higher pH (Figure 5.9E, F) reveal that with the increasing pH, the heads of the dumbbells expand.

At higher pH, some cross-linked structures (5.8) were found beside the majority of dumbbell-shaped structures. In one kind of morphology, two dumbbells are cross-linked at a common center, but in another type many dumbbells are cross-linked at a common center. As observed earlier, the dumbbell-heads are thicker at higher pH 8.50 (Figure 5.10C, D) than at lower pH 8.00 (Figure 5.10A, B).

5.1.2.3. Concentration dependence:

To see the effect of concentration on this process, the concentration ratio of the template and calcium chloride was varied and the evolved structures were isolated after 24 hours of mineralization. A very interesting effect over the evolved morphologies was observed. With a four times enhanced ratio (than that used for microtrumpet formation. *i.e.* $\text{Ca}/\text{hpdaH}_5 = 100/1$) of calcium chloride, flower-like structures (5.9) were found (Figure 5.11A), in which cudgel-shaped petals are attached to a common center (Figure 5.11B). When the ratio of both hpdaH_5 and $\text{CaCl}_2 \cdot 2\text{H}_2\text{O}$ were increased to five-fold and seven-fold respectively ($\text{Ca}/\text{hpdaH}_5 = 125/7$), long spike-like structures (5.10) were found (Figure 5.11C) with a length of up to a few hundred micrometers. After crushing these spikes they were examined under SEM (Figure 5.11D), and it was found that the long spikes are formed of bundles of long fibers (Figure 5.11E) which are formed of one dimensional aggregations of dumbbell-shaped units (Figure 5.11F) similar to those found on the wall of the microtrumpets.

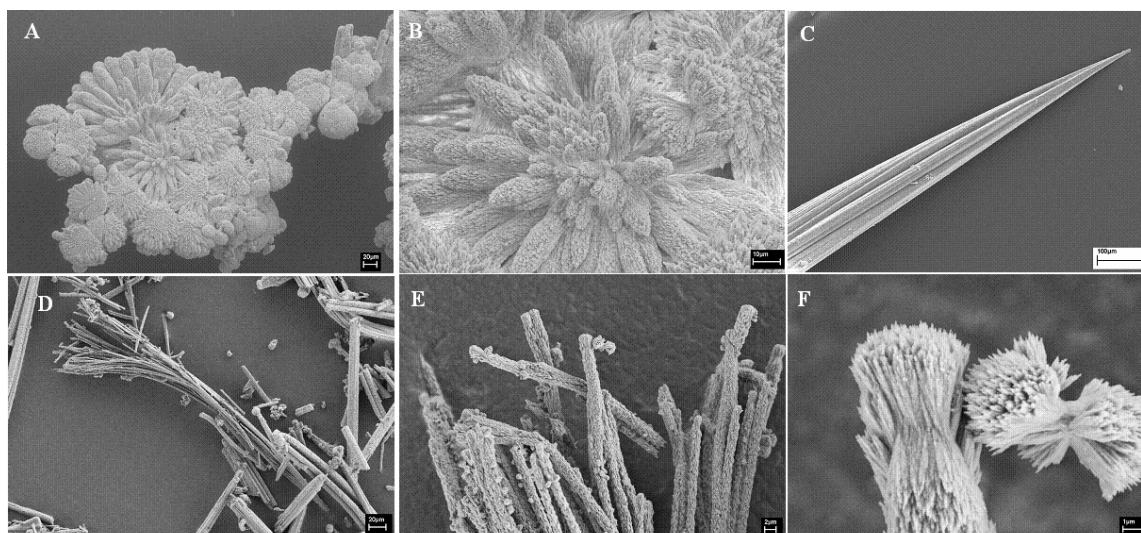


Figure 5.11: (A) Flower-like calcite structures with (B) cudgel-shaped extensions at a higher concentration of calcium chloride. (C) The long spikes obtained with a higher concentration of hpdtAH_5 and calcium chloride. (D, E) represents the crushed spikes with detached fibres. (F) Dumbbell-shaped units constituting the long fibres of the spikes. Scale bar: A, D = 20 μm , B = 10 μm , C = 100 μm , E = 2 μm and F = 1 μm

5.2. A systematic study on the functional group orientations and their effects on CaCO_3 biomineralization

5.2.1. Introduction

Amongst the three crystalline polymorphs of CaCO_3 , vaterite is the most thermodynamically unstable. Although vaterite is the least stable form, it can be found in many organisms. It is a challenge for chemists and material scientists to stabilize this morphology synthetically. Recently, Cölfen *et al.* have reported some means to stabilize the hexagonal vaterite mesostructures by using *N*-trimethylammonium derivative of hydroxyethyl cellulose and ammonia.¹³⁸

In this work, the effect of carboxylate position of the templating groups on CaCO_3 mineralization was investigated. Very simple templates, such as benzene dicarboxylic acids (1,2-BDC, 1,3-BDC, 1,4-BDC) and benzene tricarboxylic acids (1,2,4-BTC and 1,3,5-BTC), were used

to study this process. With this effort, it was possible to synthesize and stabilize novel morphologies of vaterite. A comparative study of the structures obtained using these templates gives insight into how the positions of the carboxyl groups control the morphosynthesis of calcium carbonate. For the first time, it was observed that simple templates like BTCs and BDCs can give very useful information about the steric and positional impact of the template groups over biomineralization of calcium carbonate.

In this section a detailed investigation of the time-dependence of the mineralization process and the most probable mechanism for the evolution of the vaterite structures (**5.2**) are discussed.

5.2.2. Results and discussion

The formation of different kinds of bowl-shaped vaterite morphologies was found to depend on position of the templating carboxylate groups on the benzene ring. The mineralization was performed in the presence of one of two benzenetricarboxylic acids, 1,2,4-BTC and 1,3,5-BTC. These templates were chosen to see the effect of the templating carboxylate groups which are rigidly attached to a benzene ring at different spatial positions, over CaCO₃ mineralization. In this way, well-oriented 3D patterned structures of CaCO₃ (**5.11**, **5.12**) were obtained. Additionally, to gauge further the effect of the two carboxyl groups, experiments were done using the templates 1,2-BDC, 1,3-BDC, and 1,4-BDC which produced 2D vaterite morphologies (**5.13**, **5.14** and **5.15**). This study is rather simpler and more fundamental as compared to the several investigations found in literature where much more complicated templates have been used instead. Moreover, the mineralization processes presented here were carried out in ambient conditions (around pH = 7.50, and temperature = 25 °C) using aqueous medium.

When no template is present in the course of the CaCO₃ mineralization process exclusive formation of the thermodynamically most stable calcite rhombohedra was observed. However, in the presence of templates, characteristic spherical bowl-shaped vaterite structures formed. This

indicated the role of the templates in controlling the structure pattern. From the SEM images, the presence of a minor amount of calcite rhombohedra would be observed.

The SEM image (Figure 5.12A) of the structures formed using 1,2,4-BTC after 12 hours of mineralization shows the early phase of the vaterite bowl-shaped structures. It was observed that initially two identical pyramidal structures form. These are joined together in the middle at the base and each pyramid typically has three smooth faces. The FTIR spectra (Figure 5.13A) of these structures indicate that these pyramidal structures are made of ACC. It was surprising to note that the amorphous phase was stable for more than 3 months, given that ACC is typically unstable. While it is thought to be the precursor for most of the CaCO_3 biominerals in nature, it has rarely been synthetically stabilized before.^{139, 140} Gradually the second phase of the growth starts, when certain seashell-like flanks develop towards the edges of the pyramidal structures (Figure 5.12B, C). From the growth pattern it appears that these structures follow the classical repetitive epitaxial-

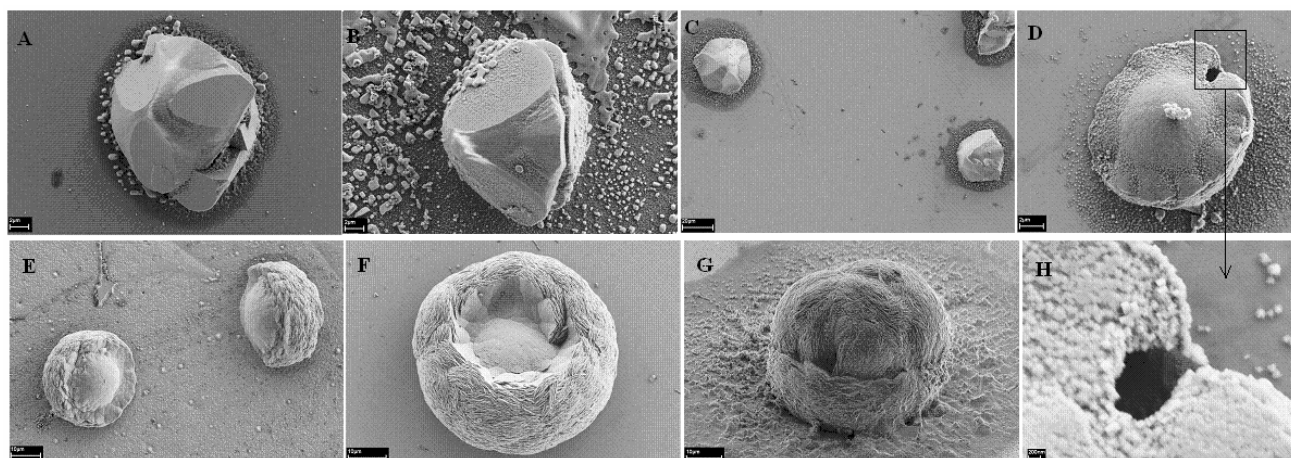


Figure 5.12: Time-dependence study of vaterite-ball formation using 1,2,4-BTC as a template (A, B, C, D, E, F, G represents the formed morphologies at 12, 24, 36, 48, 60, 72 and 108 hours, respectively). H shows the higher magnification image of the area highlighted in Fig. 5.12D.

growth pathway (Figure 5.12).^{138, 141} As a result of such repetitive growth, the characteristic smooth faces of the pyramidal structure disappear and gradually it acquires a lens-like shape (Figure 5.12D, E) ultimately leading to a bowl-shaped structure as shown in Figure 5.12F. The growth continues until this bowl-shaped structure becomes completely covered by the flanks resulting in a spherical ball-like shape after 108 hours as shown in Figure 5.12G.

Interestingly, the phase of the calcium carbonate changes as the final structure evolves. The FTIR spectra (Figure 5.13A) indicate that the initial phase is ACC whereas at the later stages (Figure 5.13B) characteristic peaks of vaterite are observed. The vaterite phase was also characterized using powder XRD patterns (characteristic peaks for vaterite at $2\theta = 20.8, 24.7, 26.9, 32.6, 39.3, 43.6$ and 49.9 degree)³³ as shown in Figure 5.13D. This polymorph-transition could be a reflection of the pH change during the course of the reaction since the pH of the medium during the reaction increases notably with time. The initial pH of the solution was 6.54, and it reaches 8.36 after 108 hours of mineralization. This change in pH is the result of a complex set of equilibria leading to the mineralization process. As the growth rates of these structures were observed to be very slow, samples were collected at 12 h intervals. The initial delay for development of the structures may be due to the lower pH of the medium at the beginning. Initially, carbon dioxide bubbles produced by the decomposition of bicarbonate were observed at the bottom of the beaker. It is likely that the periphery of these bubbles is rich in bicarbonate and thus calcium carbonate formation is facilitated at the bubble surfaces. Here, the organic templates coordinate with Ca^{2+} and take part in directing the CaCO_3 growth. To produce a crystalline form of CaCO_3 (*e.g.*, calcite, vaterite or aragonite), the Ca^{2+} and CO_3^{2-} should attain a regular array. In the present case, due to the rigid templating carboxylic acid groups which are directly attached to a benzene ring, attaining this regular array of Ca^{2+} and CO_3^{2-} is geometrically hindered since this process dominates

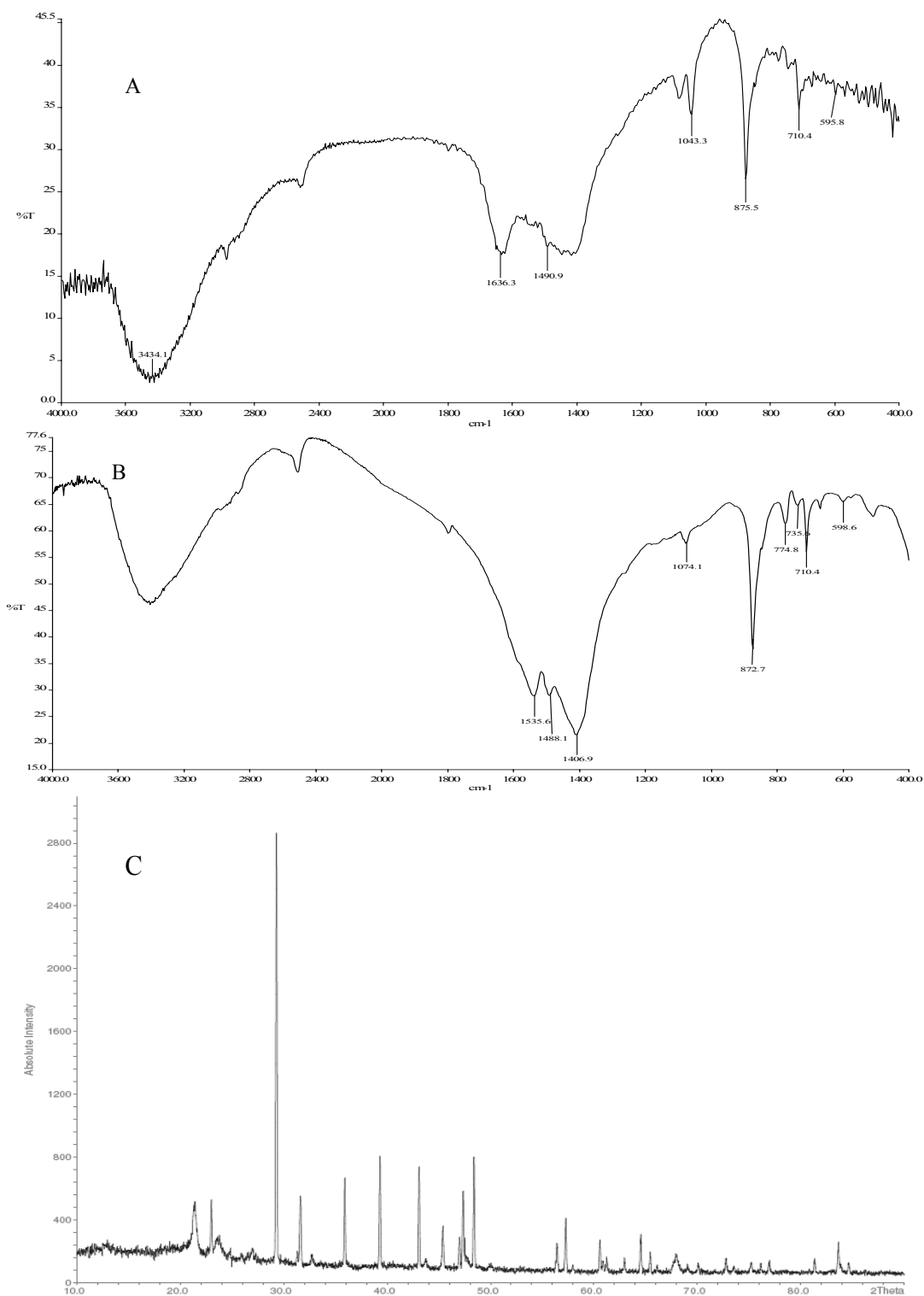


Figure 5.13: (A) IR spectrum of the sample collected after 12 hours of mineralization indicates the presence of ACC by the very broad peak in the range of $1400\text{--}1500\text{ cm}^{-1}$. Broad intense peak near 3400 cm^{-1} indicates the hydrated ACC. (B) IR spectrum of the sample collected after 72 hours showing the peaks for vaterite $735, 872$ and 1074 cm^{-1} . (C) XRD pattern of the samples collected after 72 hours (1,2,4-BTC was the template used for synthesizing the samples) shows characteristic pattern for vaterite.

at the beginning due to the high availability of the template molecules. Therefore, it is unfavourable for crystalline polymorph to form. This may explain the initial formation of the stable amorphous phase of CaCO₃. It is also consistent with the IR spectra of the samples collected at the beginning. From the SEM images (Figure 5.12A and Figure 5.12B), the smooth surface of these amorphous phases can be seen clearly. At the next step of formation, some seashell-like flanks grow from both sides towards the center of these structures (Figure 5.12D). It then attains a lens-like structure which transforms into the shape of a bowl (Figure 5.12F) finally followed by the spherical structure (Figure 5.12G) at the end. From the SEM image (Figure 5.12H) it can be seen that the inner core becomes hollow after the start of the vaterite-flank formation. This may be due to the transformation of the amorphous phase into vaterite.

Although the overall bowl-shaped structures developed using 1,2,4-BTC and 1,3,5-BTC look similar, a closer look (Figure 5.14D) reveals that there are significant differences in their texture. The initial stages are very similar, but at the later stages different growth patterns (Figure 5.14) are followed. Structures evolved using 1,2,4-BTC are made up of approximately 12 bunches of vaterite plates (Figure 5.12G). In contrast, structures evolved using 1,3,5-BTC have only 6 bunches of vaterite plates (Figure 5.14D). This can be explained by assuming a model in which one of the attached carboxylate groups is anchored to the calcium carbonate surface leaving the other two carboxyl groups free to control the shape of the CaCO₃ morphology. For example, in the case of 1,2,4-BTC, the –COOH group at the 4-position (sterically preferred) is attached to the surface so that the other two carboxyl groups at the 1- and 2- positions control the further growth of the CaCO₃ structures. In the case of 1,3,5-BTC, the –COOH group at the 5-position anchors the template to the surface (however, all the –COOH groups are equivalent here) and the –COOH groups at the 1- and 3-positions control the crystal growth pattern. In the case of 1,3,5-BTC the controlling carboxylic

acid groups are 120° apart and thus further from each other compared to those in 1,2,4-BTC (two nearest groups apart by 60°) and this may explain the different textures.

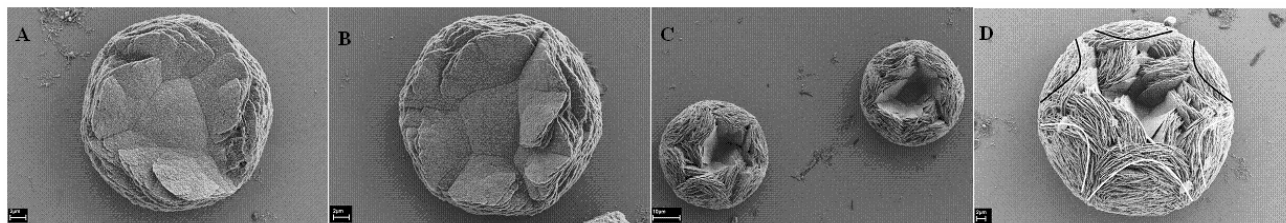


Figure 5.14: Time-dependence study of the vaterite-ball formation using 1,3,5-BTC as the template molecule (A, B, C, D, are at 12, 24, 48, and 108 hours respectively).

When BDCs (i.e 1,2-BDC; 1,3-BDC; and 1,4-BDC) were used as templates in similar conditions, characteristic circular 2D disc-like structures were formed as shown in Figure 5.15A, B and C respectively. These are completely different from the structures evolved using BDCs, as seen in Figures 5.12, 5.14, and 5.15 respectively. In this case, the morphologies are like two-dimensional mesocrystal aggregations rather than the three-dimensional structures obtained using 1,2,4-BTC and 1,3,5-BTC. These differences are the result of one less available carboxylate group in BDCs. In BTCs, the presence of three carboxylate groups may have impact over crystal growth direction in three different directions. One carboxylate group anchors itself on the Ca^{2+} ion, and the other two may direct the crystal growth in two other different directions to form such 3-dimensional structures. In contrast, BDCs have one carboxylate group anchored to the Ca^{2+} ion, and the other carboxylate group can direct crystal growth in only one other direction giving rise to a 2D structure.

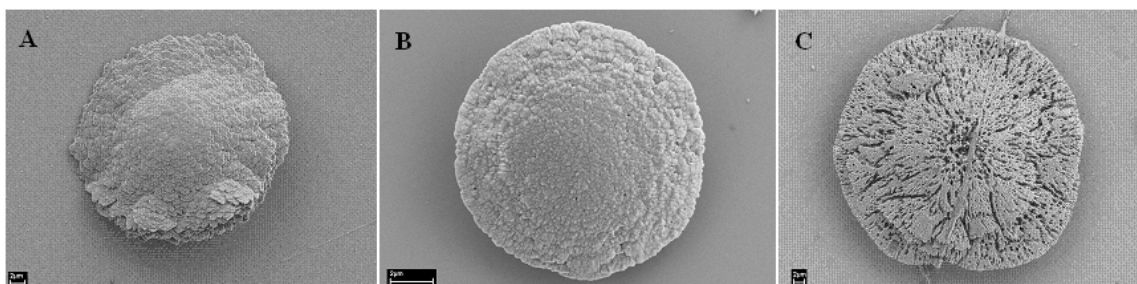


Figure 5.15: CaCO_3 structures formed by using (A) 1,2-benzene dicarboxylic acid; 1,2-BDC, (B) 1,3-benzene dicarboxylic acid; 1,3-BDC, and (C) 1,4-benzene diacboxylic acid; 1,4-BDC.

5.3. A comparative study of the mineralization of BaCO_3 and SrCO_3 influenced by 1,2,4-benzenetricarboxylic acid

5.3.1. Introduction

Barium carbonate and strontium carbonate are widely used as the precursor of several materials.¹⁴³ BaCO_3 is used in preparing glass and porcelain. SrCO_3 is used as an additive in the production of glass for coloured television tubes and as a constituent of ferrite-magnets. In addition, there are many applications of SrCO_3 such as nanometer-sized SrCO_3 -based chemiluminescence-sensors. Thus applying the strategy of nature in the synthesis of such biominerals may allow us to produce similar materials with desired properties and functionalities. For this purpose, several complex organic additives and template molecules have been used in the study of BaCO_3 mineralization.¹⁴³

In the previous sections discussing CaCO_3 , the control over shape was achieved by using benzene tricarboxylic acid (BTC) as a template. Some control over shape was expected in the mineralization of BaCO_3 and SrCO_3 because Ca, Ba, and Sr are in the same group of the periodic table. Therefore as a test, the deposition of BaCO_3 and SrCO_3 was studied using 1,2,4-benzenetricarboxylic acid (1,2,4-BTC) as a template. The terminal carboxyl groups are directly attached to the benzene ring in BTC, and thus are very rigid. A systematic study was done on the mineralization process and a sequential growth-pathway has been proposed for the formation of a nearly spherical cauliflower-like morphology of BaCO_3 (**5.16**) and for the formation of sheaf bundle-like SrCO_3 (**5.17**) mesostructures. The pH-dependence over the deposition was also studied. This is the first comparative study on the mineralization of these two metal carbonates. The final

morphologies of BaCO_3 and SrCO_3 obtained were quite different, but they both had a nearly spherical shape.

5.3.2. Results and discussion

The growth mechanism and the pH-dependence of the formed morphologies were studied on a comparative basis. The organic additive controlled the nucleation and further growth of the biominerals. 1,2,4-BTC has three carboxyl groups attached to the benzene ring which impart rigidity and controlling power to the template molecule. In the presence of 1,2,4-BTC, barium carbonate gives a highly complex cauliflower-like structure (**5.16**, Figure 5.16G), whereas strontium carbonate gives a rather simple spherical structure (**5.17**). This process is simpler than that observed in systematic study found in literature done on MCO_3 ($\text{M} = \text{Ca}, \text{Ba}, \text{Cd}, \text{Mn}, \text{and Pb}$) formation using large bulky double hydrophilic block copolymer as templates.¹³¹ In this experiment, we have used a simple commercially available aromatic template of analytical grade. Moreover, the reaction was carried out in ambient conditions in aqueous medium and in the absence of any inorganic additives.

Although the exact growth mechanism for BaCO_3 and SrCO_3 is still not understood at a molecular level, the experiments gave some insight into it. The SEM images (Figure 5.16A) of the BaCO_3 structures evolved after 24 hours of mineralization show a roughly spherical structure formed by two joined hemispheres. A close-up look at the surface of this morphology (Figure 5.16B) shows that they are made up of densely packed nanofibres. After 48 hours of reaction more bud-like structures evolve (Figure 5.16C) and a few cleavages can be traced on the spherical surface. Interestingly the surface of the structures developed at this stage (Figure 5.16D) appeared to be different from those observed at the initial stage (Figure 5.16B). At this stage, the surface appears to be made up of spike-like structures. This may be due to the fact that these are the

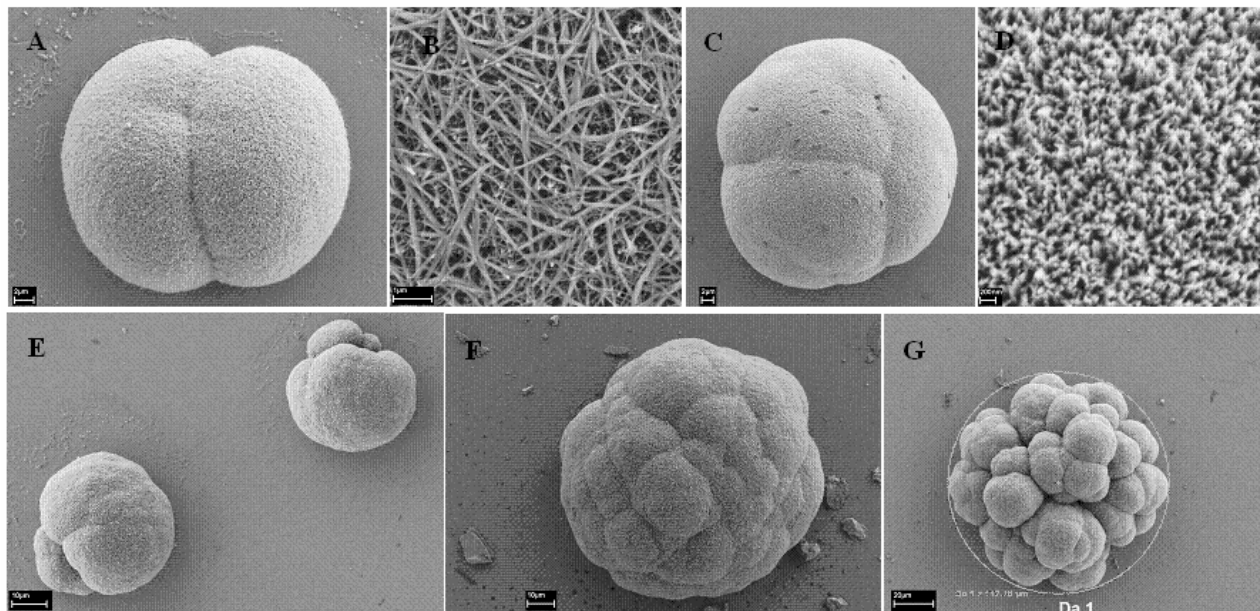


Figure 5.16: Time-dependence study of BaCO_3 structure formation (A, C, E, F, G are at 24, 48, 72, 96 and 120 hours respectively. B and D show the surface structure of structures obtained after 24 and 48 hours respectively)

termini of the fully grown nanofibers initially observed. This fact is supported in Figure 5.17, which shows the lower hemisphere. Three important aspects of the growth process can be seen from this figure. Firstly, as in a cauliflower, these spherical structures start to grow from the center to outwards. At the center there is a perfectly regular hexagon from which nanofibers begin to spread. Secondly, can be seen that the whole sphere is made up of nanofibers whose termini give the sphere a spiky surface (Figure 5.16D). Thirdly, and most importantly, with time the nanofibers assemble together in a parallel way forming a bundle-like morphology.¹⁴³ After 72 hours of reaction, the buds tend to grow independently and uniformly maintaining the spherical structure (Figure 5.16E). In this process, the buds become more prominent. This process continues repetitively (Figure 5.16F) and ultimately, after 5 days of mineralization, a highly complex cauliflower-like structure develops, as shown in Figure 5.16F. This growth process can be described as repetitive-budding. Here, unlike in other studies, we do not observe any stage where rod-like intermediate structures develop.¹²⁹ Finally, the fully grown cauliflower-like structure (Figure 5.16G) results.

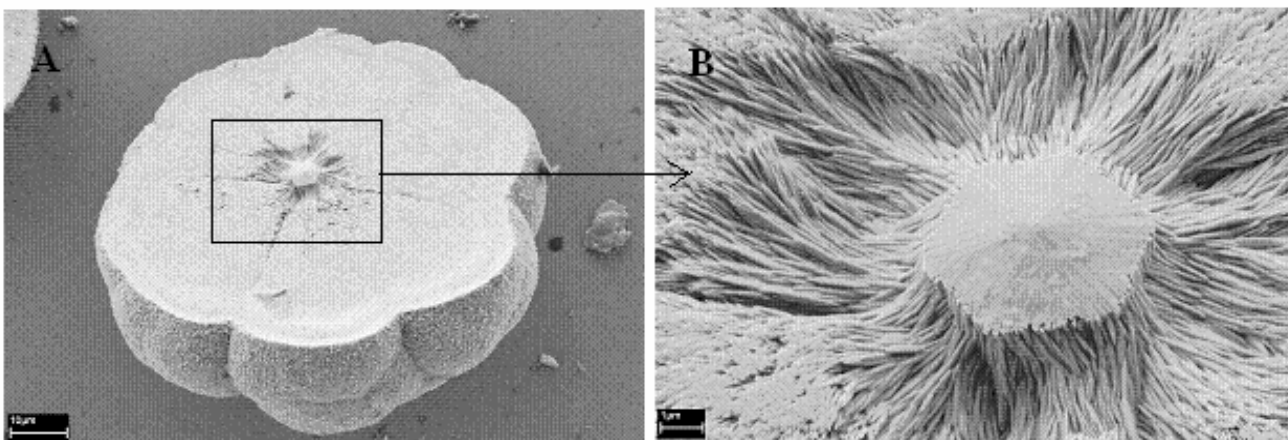


Figure 5.17: (A) A broken structure showing the horizontal view of the BaCO_3 structures formed after 96 hours. (B) A closer view of the central region showing radially arranged nanofibres.

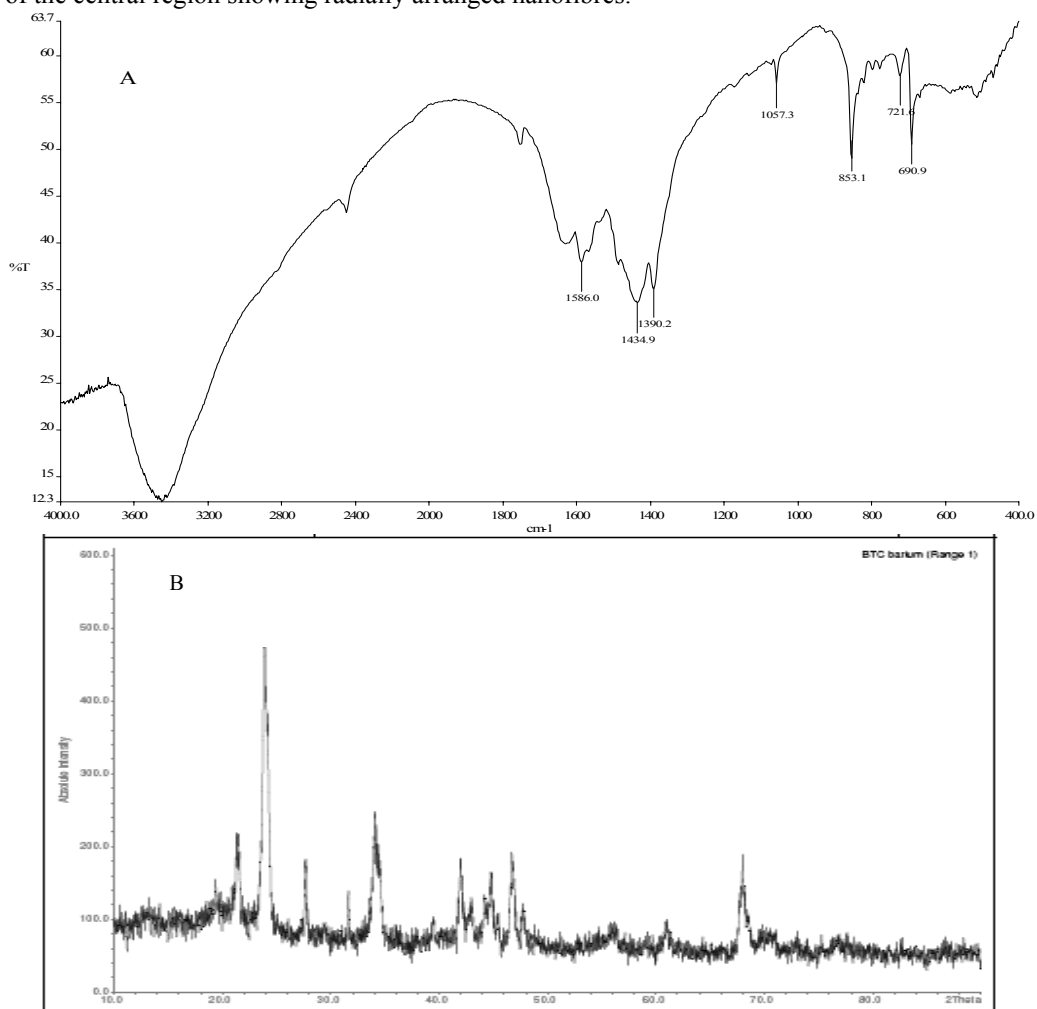


Figure 5.18: (A) IR spectra of the BaCO_3 sample collected after 96 hours. (B) Powder XRD patterns of BaCO_3 particles collected after 96 hours¹⁴⁴

The FTIR spectrum, (Figure 5.18), and the powder XRD (Figure 5.18B) indicate that these spherical BaCO₃ structures are formed of the witherite polymorph¹⁴⁴ of barium carbonate. Another important fact observed during the time-dependent growth study of these barium carbonate structures is that the pH of the medium gradually increases from 6.40 to 8.30 as the mineralization proceeds. This suggests that the process is pH-dependent and thus a systematic study of the pH-dependency of the structures was performed.

In the pH-dependence study the formation of BaCO₃ was studied at various pH values such as 4.50, 7.50, 9.50, and 10.50. At the very low pH value of 4.50 perfectly spherical structures were obtained (Figure 5.19A) without any cleavages on the surface. This may be because most of the carboxyl groups remain protonated and have little effect on controlling the resulting morphology. As a result, no budding occurs and completely spherical structures form. On the other hand, at pH 7.50, the buds were observed as shown in Figure 5.19B. This is consistent with the observations of time study (Figure. 5.16E) where after 72 hours the pH reaches approximately 8.00 and similar structures are obtained. This can be attributed to the equilibrium between the adsorption and desorption equilibrium of the template molecules on the BaCO₃ faces. As this equilibrium is well-maintained at this pH, the template molecules can effectively control the growth and hence we observe the budding. As the pH of the medium was increased to 9.50 and 10.50 the buds tended to disappear and a spherical BaCO₃ structure was obtained, (Figure 5.19A and 5.19C respectively). At this higher pH all the carboxyl groups are likely to be deprotonated. Due to the abundance of –COO[–] in the medium, they may tend to get adsorbed on the barium carbonate faces with less selectivity, which in turn inhibits the adsorption-desorption equilibrium of the template molecules on the BaCO₃ surfaces. As a result of this shift in equilibrium there is little control over BaCO₃ nucleation leading to the characteristic spherical structures of witherite (Figure 5.19D).

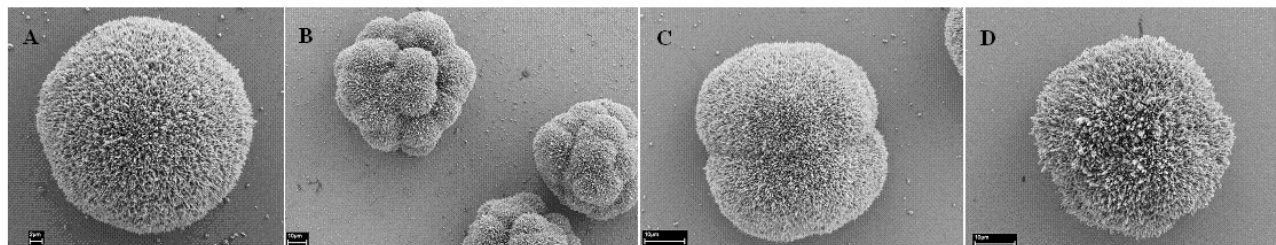


Figure 5.19: Study of the effect of pH on the BaCO_3 structure (A = 4.50, B = 7.50, C = 9.50, and D = 10.50)

In contrast to barium carbonate structure, strontium carbonate follows a different growth pattern. SEM images of the SrCO_3 particles (Figure 5.20) taken after 24 hours of reaction typically show double headed structures with a central neck. A closer examination of the surface suggests that both heads are made of sheaf-like bundles. On further growth, the heads on both of the ends grow and expand to attain a dumbbell-shaped structure. Further nucleation starts from the neck region, as shown in Figure 5.20. From there on, the structure starts to attain a spherical geometry (Figure 5.20C and 5.20D) and ultimately, after 6 days of mineralization, it attains an almost spherical shape. From a detailed analysis of the above results we can broadly divide the complete growth process into three stages. The first stage begins with the nucleation. The characteristic neck-like structure develops. It is tapered at the ends and thick at the center, with a spindle-shaped appearance. Characteristically, the sheaf bundles are radially arranged at this stage. In the second growth stage, secondary nucleation starts from both ends of the neck. In this stage, the arrangements of the sheaf bundles are different from that of the earlier stage. The bundles grow radially. It gives the heads a spherical shape (Figure 5.20B). In the third phase, the secondary nucleation begins from the lateral side of the neck. As a result, multiple heads develop from a single neck in all directions giving it an almost spherical shape (Figure 5.20E). Prolonged growth of these structures results in a perfectly spherical geometry (Figure 5.20F). From the XRD pattern of the SrCO_3 shown in (Figure 5.21B) the peaks 20.35° , 21.04° , 25.15° , 25.81° , 35.11° , 36.52° , 41.29° , and 44.05° , can be

correlated to the (hkl) indices (110), (020), (111), (021), (200), (130), (220) and (221), respectively.

The high intensity of the peak at 25.15° suggests that the crystals grow mainly along 111 planes.

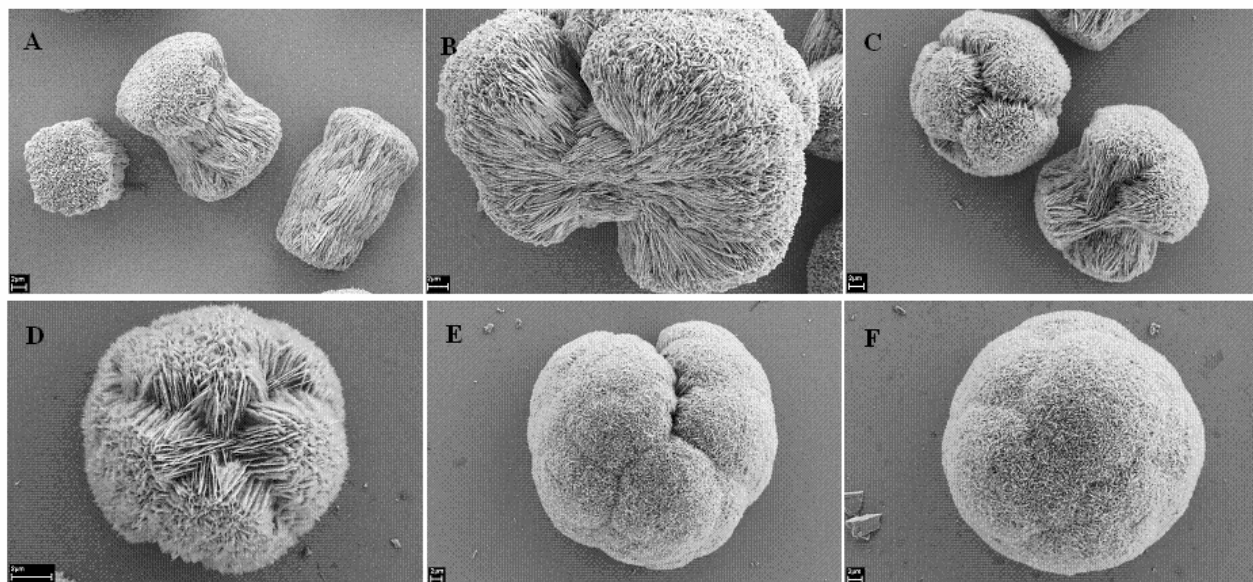


Figure 5.20: Time-dependence study of SrCO_3 structure formation (A, C, E, F are at 24, 48, 72, 96, 120 and 144 hours, respectively).

In the case of SrCO_3 mineralization, we also recorded a notable increase in pH from 6.49 to 9.10.

This change also suggests that there must be some pH-dependence in the growth of these strontium carbonate structures as seen previously for barium carbonate. To analyze the pH-dependence (Figure 5.22), the mineralization was carried out in different pH conditions. For this purpose, the pH of the medium was set artificially at steps of 4.50, 6.50, 8.00 and 10.00 by dropwise addition of dilute HCl or NaOH solution. It was observed that at the low pH of 4.50, we get proper dumbbell-shaped structures (Figure 5.22A). At the higher pH of 6.50, we get quadruple structures (Figure 5.22B), made up of four heads with a common neck arranged diametrically. At the higher pH of 8.00 and 10.00, spindle-like structures were obtained as shown in Figure 5.22C and 5.22D respectively. These structures are similar to those obtained at the initial stage of time dependence study (Figure 5.20A). These results are in excellent agreement with the time-dependence study and

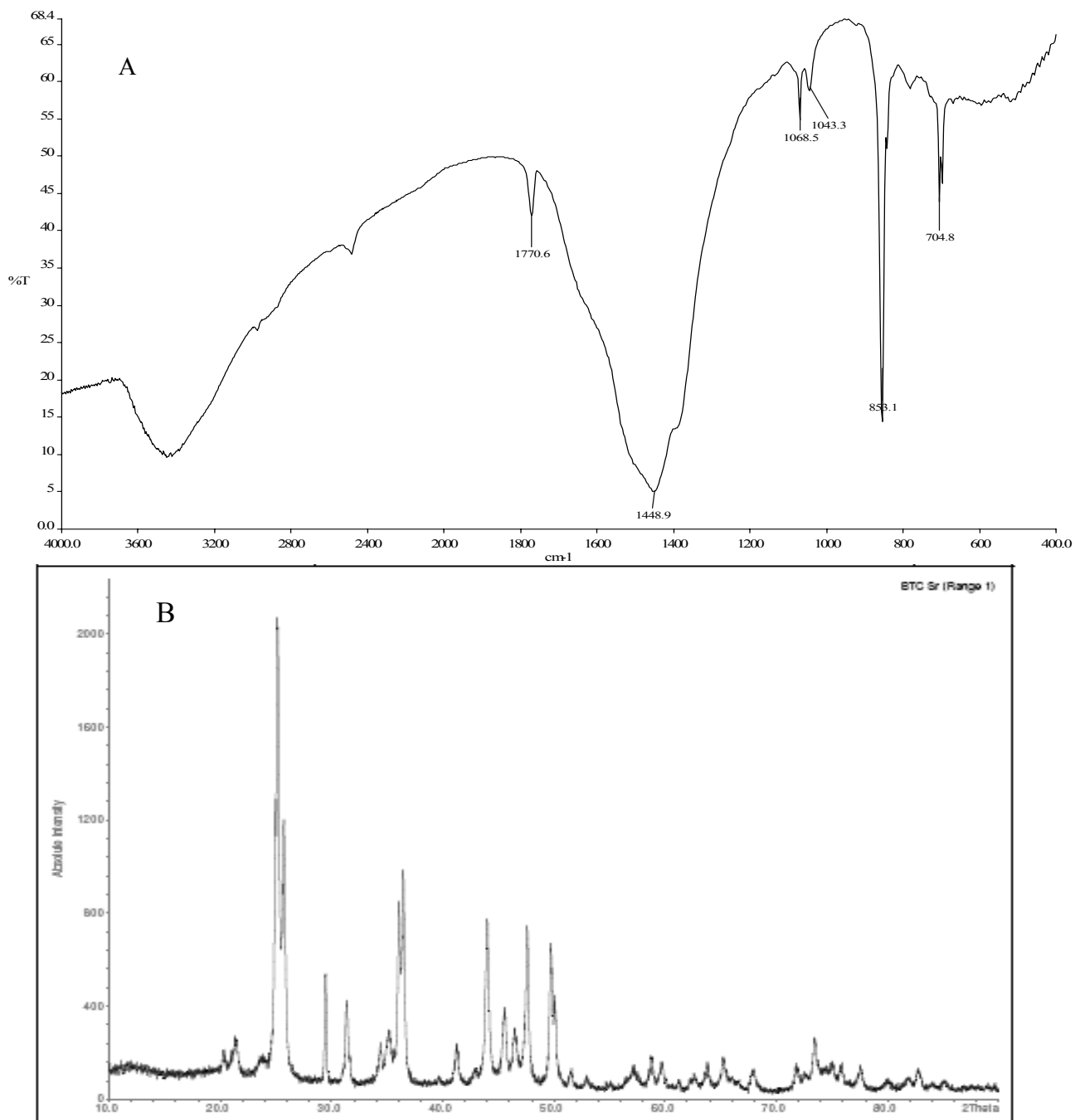


Figure 5.21: (A) IR spectra of the SrCO_3 sample collected after 96 hours. (B) Powder XRD patterns of SrCO_3 sample collected after 96 hours. Broadness of the peaks suggest the presence of nanometer-scale particles in the sample.

follow a similar trend to those for the analogous barium carbonate structures. At lower pH, due to the presence of protonated carboxyl groups, there is little control over growth. Probably as a result

of the adsorption and desorption of the template molecules at the pH of 6.50, the structures grow in a well-controlled way. At the high pH values of 8.00 and 10.00, due to unselective adsorption of the template molecules on the SrCO_3 -surface, the adsorption-desorption equilibrium is inhibited and cannot be maintained. As a result, controlled growth becomes impossible and only the spindle-like SrCO_3 structures form.

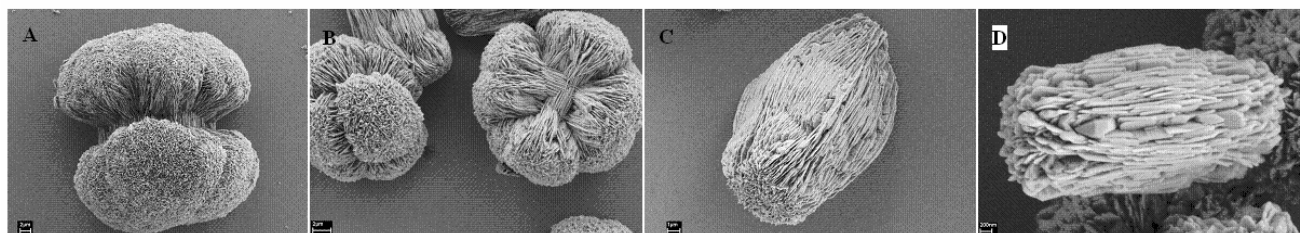


Figure 5.22: Study of pH effect on the SrCO_3 structures (A = 4.50, B = 6.50, C = 8.00, D = 10.00).

5.4 Summary

In the beginning of this section studying the synthesis of calcite microtrumpet formation, three main aspects were found. **First**, it has been proved that the characteristic of the surface has an enormous effect on the biomineral morphology. **Second**, it has been realized that it is possible to tune the shapes of the evolved morphology of the calcites by changing pH and concentration. **Third**, for the first time an interesting combination of surface chemistry and solution chemistry is investigated, and the final result is the calcite trumpets.

In the second part, it was realized from our research that it is possible to produce synthetically stable vaterite morphology under ambient conditions. The rigidity of the template molecules determines the shape and morphology of the precursors and it affects the growth pattern. As a result, the positions of the carboxyl groups play a vital role in the growth and aggregation, with their relative positions determining the final morphology and dimensionality.

From the research on controlled formation of BaCO_3 and SrCO_3 micro-structures, it can be concluded that barium and strontium carbonates follow different growth pathways under the influence of the same template molecules and similar reaction conditions. BaCO_3 structures develop *via* consecutive budding whereas SrCO_3 structures develop *via* a stable dumbbell-shaped intermediate. Moreover, the surface-morphology of barium carbonate structures differ greatly from the analogous strontium carbonate structures. BaCO_3 structures are made up of densely organized nano-fibers whereas SrCO_3 structures are made up of sheaf bundle-like structures. Also a strong pH-dependence was observed in the nucleation and growth of the structures. The pH of the medium increases considerably in both cases as the reaction proceeds. This observation, coupled with those made when the pH of the medium was artificially adjusted, suggests that there is some particular pH range in which controlled growth of both barium and strontium carbonate structures occurs. The structures evolved at higher pH show that the growth becomes less regular.

CHAPTER 6

Conclusions

The work performed during the course of this Ph. D. research can be divided into three major parts which are discussed in the previous three chapters. **Chapter 3** described the use of polyalkoxy ligands in the synthesis of magnetically interesting polynuclear manganese and iron complexes. **Chapter 4** described the synthesis and magnetic studies of a family of 1D lanthanide chain compounds, and **Chapter 5** described the use of simple flexible and rigid organic templates to control the aggregation of calcium carbonate.

In **Chapter 3**, four compounds were described. The aim here was to produce molecules that behave as single-molecule magnets, SMMs. A new Mn_6 cluster, $[(PtolH)_4(O_2CMe)_6(\mu_6-O)Mn^{III}_6] \cdot 1.5en$ (**3.1**) was synthesized using pentaerythritol ($PtolH_4$, $C(CH_2OH)_4$) as a ligand. The compound shows slow relaxation of the magnetization at low temperature indicating that it may be a new SMM. A Mn_{17} cluster, $[Mn^{III}_{11}Mn^{II}_6(\mu_4-O)_8(\mu_3-Cl)_4(\mu_5-O_2CMe)_2(DPD)_{10}Cl_{2.34}(O_2CMe)_{0.66}(py)_3(MeCN)_2] \cdot 7MeCN$ (**3.2**), was synthesized using 2,2-dimethyl propan-1,3-diol ($DPDH_2$, $HOCH_2C(CH_3)_2CH_2OH$). This compound can be regarded as consisting of two fused supertetrahedral Mn_{10} units which are linked *via* a common edge. The supertetrahedral structure is made up of a tetrahedral arrangement of Mn^{II} ions with an octahedral arrangement of Mn^{III} ions inscribed within it. Besides its interesting structure, compound **3.2** possesses a large ground spin state ($S = 28$). The compound may be a SMM because it shows magnetic hysteresis and slow relaxation of magnetization at very low temperature. The origin of the hysteresis may be the result of the anisotropic Mn^{III} ions and/or the intermolecular interactions. In order to gain further information, high-field EPR investigations are underway. Using the ligand propan-1,2,3-triol (glycerol, $HOCH_2CH(OH)CH_2OH$), a 3D network, $[\{ Mn^{III}_{12}Mn^{II}_9(\mu_4-$

$\text{O})_8(\text{glycH})_{12}(\mu\text{-}1,1\text{-N}_3)_6(\text{OH}_2)_6(\text{N}_3)_{1.5}\{\text{Mn}^{\text{II}}(\mu\text{-}1,3\text{-N}_3)_{4.5}(\text{OH}_2)_{1.5}\}\text{Cl}_4 \cdot \text{ca.}7.5\text{H}_2\text{O}$ (**3.3**, where glycH^{2-} is the dianion of propan-1,2,3-triol), with repeating units of Mn_{21} was synthesized. The repeating units are linked *via* mononuclear $\text{Mn}(\text{N}_3)_6$ units. The compound has an aesthetically pleasing structure where the oxygen and manganese atoms are arranged in an array of different kinds of concentric polyhedra. Namely, a Mn^{II} center is surrounded by a cube defined by eight $\mu_4\text{-O}$ groups. This cube is surrounded by an icosahedron made by twelve Mn^{III} centers, and this icosahedron is surrounded by a Mn^{II}_8 cube which is finally surrounded by six Mn^{II} centers to give an octahedron. With its cubic array of alternating cationic and anionic species with coordination numbers $\{6:6\}$, the structure is strongly reminiscent of that of NaCl . A more appropriate structural type, however, would be that of iron pyrites (FeS_2), which can be derived from the NaCl structure by lowering its symmetry to space group $Pa\bar{3}$. In the present case, the Mn_{21} units occupy the of $\bar{3}$ symmetry sites corresponding to the positions of the disulfide dianions in FeS_2 . The compound contains solvent waters which can be driven off by heating resulting in a shrinkage of the unit cell volume. Compound **3.3** exhibits overall antiferromagnetic coupling without any saturation of the magnetization in our experimental range of temperature and magnetic field. This point suggests some inherent anisotropy which is expected from the Jahn-Teller distortions of the Mn^{III} ions present in the structure. Interestingly, when this compound was used to prepare MnO_2 by pyrolysis, it gave micrometer-scale porous β -manganese dioxide with a very high surface area. The capacitance was found to be very high, but unfortunately it falls off rapidly after a few cycles. Furthermore, evidence of an intra-cluster nitrate formation reaction was discovered *via* the decomposition of the azides to give N_2 , H_2 and NO_3^- . At higher temperature, the ligands also decompose into many gases (*e.g.* H_2 , CO_2 and CO). This can account for how the highly porous structure forms. An Fe_6 cluster, $[(\text{Piv})_6(\text{PdolH})_6\text{O}_2\text{Fe}_6](\text{NO}_3)_2 \cdot 2\text{CH}_3\text{CN}$ (**3.4**, PdolH is $\text{CH}_3\text{CH}(\text{OH})\text{CH}_2\text{O}^-$), was synthesized using a pre-formed Fe_3 cluster as the building unit. Two Fe_3

units were linked together by six propan-1,2-diol molecules, in a trigonal antiprismatic arrangement to give a distorted octahedral Fe₆ core. The compound shows strong antiferromagnetic coupling leading to an almost zero ground spin state.

In **Chapter 4**, ethylene glycol together with sodium benzoate was used to synthesize a family of one dimensional lanthanide chains. The isostructural compounds were obtained for seven lanthanides, Pr, Nd, Gd, Tb, Dy, Ho and Er. A systematic study of their magnetic properties was carried out, and the experimental data was in very close agreement with the expected behavior. The dysprosium compound was found to show slow relaxation of magnetization at very low temperature and could be a new example of a single-chain magnet.

In **Chapter 5** the controlled formation of calcium carbonate, barium carbonate and strontium carbonate are discussed. A monohydroxy tetracarboxylic diamine (hpdt₄H₅) was used as a template in the controlled growth of CaCO₃ mesocrystals. Trumpet-like structures, which resemble those found in the coccolithophore, *Discosphaera Tubifera*, were found. Spectroscopic studies revealed that the two precursors, an amorphous calcium carbonate bobble-hat motif and dumbbell-shaped units form first followed by the trumpet structures. With the help of dynamic light scattering (DLS) study, the mechanism of formation of the microtrumpets was established. Subsequently, control over the formation of CaCO₃-aggregation was studied using relatively rigid templates, such as benzene dicarboxylic acids and benzene tricarboxylic acids. Interestingly, it was possible to stabilize the relatively less stable vaterite polymorph of CaCO₃ using this template system. Different kinds of bowl-shaped vaterite structures evolved in the course of this investigation. The effect of the position of the functional groups within the template could be deduced from the shapes of the evolved morphologies. It was thus found that as in coordination chemistry the nature and disposition of the coordinating groups of the ligands play an important role in determining the final structure. The structures formed with barium and strontium were investigated to provide a

comparison, and the effect of 1,2,4-benzenetricarboxylic acid was studied in the mineralization of BaCO_3 and SrCO_3 . Microstructures made of nanofibers were observed. The change of the pH of the medium induced some significant changes in the evolved shapes, and less regular morphologies were found at higher pH.

CHAPTER 7

Experimental

7.1. Materials:

All the chemicals used throughout this research were purchased from commercial chemical suppliers such as Aldrich and Fluka, and they were used without any further purification.

7.2. Identification and characterization of materials

7.2.1. X-ray crystallography. Where single crystals have been obtained, structural characterizations have been performed using either STOE IPDS, STOE IPDS II or Bruker Apex SMART area detector diffractometers. All data sets were measured using graphite monochromated Mo-K α radiation ($\lambda = 0.71069 \text{ \AA}$). The crystals were mounted on a glass-fiber immediately after they were taken out of the solution. An epoxy resin was used to cover the crystal and isolate it from the aerial atmosphere. All the crystallographic data were collected at 200 K. The crystal structure was solved and refined using the SHELXTL software package.⁸⁵

7.2.2. X-ray powder diffraction. The powder X-ray diffraction analysis was carried out using a STOE Stadi P X-ray powder diffractometer having a position sensitive detector and a germanium monochromator. Measurements were performed at room temperature using Co-K α radiation ($\lambda = 1.78897 \text{ \AA}$). The diffractometer was calibrated using silicon. The data were processed using the software program WinXPOW.¹⁴⁵ Samples were finely ground and fixed between two polyethylene sheets using grease (Lithylen).

7.2.3. FT-IR spectroscopy. Infra-red characterizations were performed using a Perkin Elmer Spectrum One spectrometer in the range of 400 cm^{-1} to 4000 cm^{-1} in transmission mode using 4 scans at a resolution of 4 cm^{-1} . Spectra were obtained to provide a fingerprint of the sample.

The samples were ground and mixed finely with KBr in a *ca.* 1:50 ratio. A KBr-disc of the sample, 1 cm in diameter, was obtained by applying hydrolic presure under vacuum.

7.2.4. Elemental analysis. The amounts of carbon, hydrogen and nitrogen in most samples were quantitatively analyzed using an Elementar Vario EL analyzer.

7.2.5. Scanning electron microscopy (SEM). SEM analyses were done using dry samples placed on double-sided conducting carbon tape. In a few cases, samples were sputter-coated with a very thin layer of gold. Sputtering was performed in an argon atmosphere using either an Emitech or a Polaron Equipment LTD sputter coater. The SEM studies were performed using a LEO 1530 scanning electron microscope (< 10 nm lateral resolution) operating between 200 V - 30 kV. This was equipped with an energy-dispersive X-ray detector from Oxford Instruments (EDX INCA 400). The samples were studied on a carbon support at 10^{-4} Pa reduced pressure.

7.2.6. Dynamic light scattering (DLS). Dynamic light scattering (DLS) is also known as quasi-elastic light scattering. It was used for determining the hydro-dynamic diameter of the micrometer-sized particles in solution and for monitoring the kinetics of time-dependent processes, such as particle growth. This method is based upon a mechanism of absorption and re-emission of electromagnetic radiation. The samples were taken into clean and dust-free quartz cuvettes and the cuvettes were placed into the DLS device. DLS measurements were done using a Zetasizer spectrometer (Malvern Instruments Ltd., Model Z3000) equipped with a 5 mW He-Ne laser.

7.2.7. Magnetic measurements. Magnetic susceptibility measurements were performed using a Quantum Design MPMS-XL SQUID susceptometer with an external magnetic field of 7 T. Most measurements were performed on dry polycrystalline samples while a few were done on the polycrystalline material maintained in their mother liqueur to avoid solvent loss. The magnetic data were corrected for the sample holder and the diamagnetic component of the sample. The diamagnetic contribution for the samples were calculated using Pascal's constants.¹⁴⁶

7.3. Preparation of the compounds and materials

7.3.1. Preparation of 3.1. Ethylenediamine (50 μL) was added to a methanolic solution (10 mL) of pentaerythritol (240 mg, 1.5 mmol) and KOH (28 mg, 0.5 mmol). This was followed by the addition of a $\text{Mn}(\text{O}_2\text{CMe})_2 \cdot 4\text{H}_2\text{O}$ (368 mg, 1.5 mmol) solution in 5 mL of methanol. The resulting solution was stirred for one hour at room temperature and kept undisturbed for slow evaporation of the solvent. Dark brown, rod-shaped crystals of **3.1** were observed after several weeks (42% yield). Elemental analysis (%) calculated for $\text{C}_{34}\text{H}_{62}\text{Mn}_6\text{N}_2\text{O}_{29}$ (**3.1**): C 33.60, H 4.90, N 3.09; Found: C 33.86, H 4.69, N 2.98. IR data (KBr disc, cm^{-1}): 3386(b), 2862(m), 2081(w), 1571(s), 1394(s), 1331(m), 1190(w), 1115(s), 1069(m), 1023(s), 962(m), 798(w), 650(s), 585(s), 527(m).

7.3.2. Preparation of 3.2. Pyridine (480 μL , 8 mmol) was added slowly to a stirring mixture of $\text{MnCl}_2 \cdot 4\text{H}_2\text{O}$ (594 mg, 3 mmol), 2,2-dimethyl-1,2-propandiol (420 mg, 4 mmol) and sodium acetate (480 mg, 6 mmol) in 20 mL of acetonitrile. After vigorous stirring for 2 hours, the resulting light brown solution was allowed to evaporate slowly. Reddish-brown, rod-shaped crystals formed after 4 days. Yield 26%. Elemental analysis (%) Calculated for $\text{C}_{88.32}\text{H}_{149.98}\text{C}_{16.34}$ (**3.2**): C 34.53, H 4.92, N 5.47; Found: C 31.21, H 4.48, N 1.76. The lower percentages of C, H, N is attributed to the tendency of **3.2** to desolvate: Calcd for (**1-2MeCN**): C 31.25, H 4.59, N 1.56. IR data (KBr disc, cm^{-1}): 3437 (b), 2927 (m), 2841(m), 2676(w), 1599(m), 1663(s), 1441(m), 1394(s), 1385(s), 1217(w), 1148(w), 1076(vs), 1022(m), 936(w), 912(w), 786(w), 761(w), 711(m), 654(s), 630(s), 608(s), 585(m), 530(s).

7.3.3. Preparation of 3.3. Compound **3.3** was synthesized by dissolving propan-1,2,3-triol (73 μL , 1 mmol) in methanol (20 mL) followed by the addition of $\text{MnCl}_2 \cdot 4\text{H}_2\text{O}$ (198 mg, 1 mmol) with vigorous stirring. The resulting solution was added to a solution of sodium azide (65 mg, 1 mmol) in MeOH (5 mL). The final solution was stirred further for 8 hours, filtered and left undisturbed at room temperature. Slow evaporation of the solvent gave black, prism-shaped crystals

within 3 weeks in approximately 30% yield. Elemental analysis (%): calculated for $C_{36}H_{102}Cl_4Mn_{22}N_{36}O_{59}$ (**3.3**): C 12.97, H 3.08, N 15.12; found: C 12.74, H 3.05, N 15.25. Calculated for $C_{36}H_{87}Cl_4Mn_{22}N_{36}O_{51.5}$ (**3.3a**) (corresponding to loss of all lattice waters): C 13.52, H 2.74, N 15.76; found: C 13.50, H 3.25, N 16.15. Selected IR data (KBr disc, cm^{-1}): 3401(b), 2928(s), 2877(s), 2063(vs), 1633(m), 1466(m), 1348(m), 1321(m), 1265(m), 1086(vs), 1021(s), 956(s), 917(m), 860(s), 743(vs), 593(s).

7.5. Preparation of 3.4. The starting compound, an Fe_3 cluster, $[Fe_3(\mu_3-O)(piv)_6(H_2O)_3]piv$, was synthesized using a reported procedure³⁶ with a slight modification. $Fe(NO_3)_3 \cdot 9H_2O$ (10 g, 24.8 mmol) and Hpiv (28.0 g, 290 mmol) were heated slowly with stirring up to 160 ± 5 °C over 3 h until the elimination of NO_2 was finished. Upon cooling to 75-80 °C, ethanol (85 mL) and water (15 mL) were added slowly under stirring. Upon standing overnight, the red-brown hexagonal prism-shaped crystals of Fe_3 formed. They were filtered off, washed with benzene and hexane, and dried in air.

The Fe_3 compound (111 mg, 0.12 mmol) was added to 10 mL of acetonitrile followed by vigorous stirring at room temperature. The resulting solution was then added to a mixture of propan-1,2-diol (300 mg, 0.4 mmol) and $Dy(H_2O)_3 \cdot 9H_2O$ (228 mg, 0.5 mmol) in 10 mL of acetonitrile. This mixture was then refluxed for 1 h, stirred at room temperature for 30 min, and filtered. The filtrate was kept undisturbed at room temperature. Green, brick-shaped crystals of (**3.4**) were observed within 3 weeks. Yield: 26%. Elemental analysis (%): calculated for $Fe_6C_{52}H_{102}O_{32}N_4$ (**3.4**): C 38.31, H 6.31, N 3.44; found: C 38.93, H 6.25, N 2.96. Selected IR data (KBr disc, cm^{-1}): 3260(b), 2966(s), 2263(w), 1566(s), 1486(s), 1429(s), 1383(s), 1232(s), 1053(s), 852(m), 633(s), 604(s).

7.3.5. Preparations of 4.1-4.7. All the polymeric compounds were synthesized in the following way. The lanthanide salt $Ln(NO_3)_3 \cdot 8H_2O$ ($Ln = Pr, Nd, Gd, Tb, Dy, Ho, Er$) (0.5 mmol)

was added to a methanolic solution (20 mL) of ethylene glycol and sodium benzoate (144 mg, 1 mmol) followed by vigorous stirring for 1 hour. The resulting solution was filtered and kept undisturbed for slow evaporation. Thin small crystals formed within 2 days. Yields: 42% [Pr], 40% [Nd], 48% [Gd], 51% [Tb], 39% [Dy], 47% [Ho], 45% [Er]. FT-IR analysis: All [Ln(PhCOO)₃(EtglyH₂)(MeOH)] compounds display similar IR spectra because Ln-O bond vibrations are not in the investigated range. List of main peaks for [Gd(PhCOO)₃(Etgly)(MeOH)] are provided as the standard spectra (in cm⁻¹): 3233(b), 1972(w), 1930(w), 1627(m), 1593(s), 1537(s), 1423(s), 1307(m), 1179(m), 1071(s), 1023(m), 720(s), 548(m), 422(m). Elemental analysis: Calculated for C₂₁H₂₅O₉Pr (**4.1**): C, 44.85; H, 4.48; found: C, 44.47; H, 4.42. Calculated for C₂₁H₂₅O₉Nd (**4.2**): C, 44.59; H, 4.45; found: C, 44.73; H, 4.56. Calculated for C₂₁H₂₅O₉Gd (**4.3**): C, 43.58; H, 4.35; found: C, 43.21; H, 4.22. Calculated for C₂₁H₂₅O₉Tb (**4.4**): C, 43.46; H, 4.34; found: C, 43.40; H, 4.13. Calculated for C₂₁H₂₅O₉Dy (**4.5**): C, 43.20; H, 4.32; found: C, 43.12; H, 4.25. Calculated for C₂₁H₂₅O₉Ho (**4.6**): C, 43.02; H, 4.30; found: C, 42.98; H, 4.07. Calculated for C₂₁H₂₅O₉Er (**4.7**): C, 42.85; H, 4.28; found: C, 42.23; H, 4.43.

7.3.6. Preparation of 5.1-5.10. Calcium carbonate deposition was done in 100-mL glass beakers cleaned with *aqua regia*, washed thoroughly with distilled water, and then dried in air. Aqueous solutions of hpdtaH₅ (2 mM, 5 mL) and of CaCl₂·2H₂O (25 mM, 10 mL) were prepared. NaHCO₃ (42 mg, 0.5 mM) was added to the vigorously stirred solution of hpdtaH₅. This was followed by the addition of CaCl₂ solution. The resulting solution was kept at room temperature (20 °C) for 24 hours to form the matured microtrumpets. For the pH dependence study, the NaOH solution (0.5 M) or HCl solution (0.5 M) was added dropwise to the solution to obtain the desired pH. The pH was measured by using a WTW pH90 pH-meter.

7.3.7. Preparation of 5.11-5.15. The glassware was cleaned using *aqua regia*, washed thoroughly with distilled water, rinsed with acetone, and dried in air. Silicon wafers (5 mm × 5

mm), placed at the bottom of the beaker) were cut out from a 4-inch silicon wafer, washed with dilute HCl, rinsed with de-ionised water and acetone, and dried in air. The experiments were carried out at room temperature (20 ± 1 °C) and at atmospheric pressure.

The templates, BTCs (0.04 mmol) or BDCs (0.04 mmol), were added with NaHCO₃ (0.25 mmol) to 10 mL of distilled water in a 50-mL beaker with vigorous stirring to ensure complete dissolution. A 10-mL aqueous solution of CaCl₂·2H₂O (0.12 mmol) was added to the aqueous solution of the template (BDC or BTC) and NaHCO₃ with stirring. The precipitation was allowed to proceed with a silicon piece at the bottom of the beaker and left without any further mechanical disturbances. For sequential study of the growth, the silicon pieces were taken out of the solution at regular time-intervals, dried in air and examined using SEM.

7.3.8. Preparation of 5.16 and 5.17. The glassware was cleaned with *aqua regia*, washed thoroughly with distilled water, rinsed with acetone, and finally dried in air. Pieces of silicon wafers, (5 mm x 5 mm placed at the bottom of the beaker) were cut out from a 4-inch silicon wafer. The pieces were washed with dilute HCl, rinsed with deionised water and acetone, and finally dried in air.

The experiments were carried out at room temperature (20 ± 1 °C) and atmospheric pressure. 1,2,4-BTC (0.008 g, 0.038 mmol) was mixed with NaHCO₃ (0.021 g, 0.25 mmol) in 10 mL of distilled water in a 50-mL glass beaker under vigorous stirring to ensure complete dissolution. A solution of either BaCl₂ (0.018 g, 0.073 mmol) or SrCl₂ (0.019 g, 0.073 mmol), prepared in 10 mL of distilled water, was added to the previously prepared solution of the template and NaHCO₃ with stirring. The precipitation was carried out with a silicon piece at the bottom of the beaker, without any further mechanical disturbances. For sequential study of the growth mechanism, the silicon pieces were taken out of the solution at regular intervals, washed with distilled water, dried in air, and examined using SEM.

For the pH dependence study of the mineralization, 1,2,4-BTC (0.008 mmol, 0.038 mmol) was dissolved in 10 mL of distilled water with vigorous stirring. To each solution, NaHCO₃ (0.021 g, 0.25 mmol) was added with stirring, and dilute NaOH (aq, 0.5 M) and/or HCl (aq, 0.5 M) was added dropwise to obtain the desired pH of the resulting solution. Finally, 10 mL of aqueous solution of either BaCl₂ (0.018 mmol, 0.073 mmol) or SrCl₂ (0.019 mmol, 0.073 mmol) was added to each. Precipitation was then allowed to carry out without any mechanical disturbances.

CHAPTER 8

Bibliography

1. G.B. Kauffman, "Alfred Werner - Founder of Coordination Chemistry", Springer-Verlag, Berlin, 1966.
2. F. A. Cotton, *J. Chem. Soc., Dalton Trans.*, **2000**, 1961. (a) Carlucci, L.; Ciani, G.; Proserpio, D.M.; Sironi, A. *Angew. Chem. Int. Ed.*, **1995**, *107*, 2037; (b) Yaghi, O. M.; Sun, Z.; Richardson, D.A.; Groy, T. L. *J. Am. Chem. Soc.*, **1994**, *116*, 807; (c) Carlucci, L.; Ciani, G.; Gudenberg, D. W. V.; Proserpio, D. M.; Sironi, A. *Chem. Commun.*, **1997**, 631; (d) Kitagawa, S.; Munakata, M.; Tanimura, T. *Inorg. Chem.* **1992**, *31*, 1714; (e) Kawata, S.; Kitagawa, S.; Kondo, M.; Furuchi, I.; Munakata, M. *Angew. Chem. Int. Ed.*, **1994**, *33*, 1759; (f) Kitagawa, S.; Okubo, T.; Kawata, S.; Kondo, M.; Katada, M.; Kobayashi. *Inorg. Chem.* **1995**, *34*, 4790; (g) Munno, De, J.; Ruiz, R.; Lloret, F.; Faus, J.; Sessoli, R.; Julve, m. *Inorg. Chem.* **1995**, *34*, 408.
3. (a) R. L. Carlin, *Magnetochemistry*, Springer-Verlag, 1986; (b) O. Kahn, *Molecular Magnetism*, VCH Publ., 1993; (c) C. Kittel, *Introduction to solid state physics*, 2nd Ed., J. Wiley and Sons, New York, 1953.
4. J. M. Lehn, *Supramolecular Chemistry: Concepts and Perspectives*, VCH, publ, 1995.
5. (a) R. Winpenny (ed), *Str. Bonding*, **2006**, 122; (b) D. Gatteschi, R. Sessoli, J. Villain, *Molecular Nanomagnets*, Oxford University Press, **2006**. (c) *Magnetism: Molecules to Materials. Molecule Based Materials*, Vol. 2 (Eds.: J. S. Miller, M. Drillon), Wiley-VCH, Weinheim, 2001.
6. (a) G. Christou, D. Gatteschi, and D. N. Hendrickson, *MRS Bulletin*, **2000**, *25*, 66; (b) J. R. Long, In *Chemistry of Nanostructured Materials*; Yang, P., Ed.; World Scientific: Hong Kong, 2003, pp 291-315 and references therein.
7. (a) T. Lis, *Acta Crystallogr., Sect. B: Struct. Crystallogr. Cryst. Chem.* **1980**, *36*, 2042. (b) A. Caneschi, D. Gatteschi, R. Sessoli, A.-L. Barra, L. C. Brunel, M. Guillot, *J. Am. Chem. Soc.* **1991**, *113*, 5873. (c) R. Sessoli, D. Gatteschi, A. Caneschi, M. A. Novak, *Nature* **1993**, *365*, 141.
8. B. Xu, N. D. Chasteen, *J Biol Chem* **1991**, *266*, 19965.
9. A. M. Ako, I. J. Hewitt, V. Mereacre, R. Clerac, W. Wernsdorfer, C. E. Anson, and A. K. Powell, *Angew. Chem. Int. Ed.* **2006**, *45*, 4926.
10. C. J. Milios, A. Vinslava, W. Wernsdorfer, S. Moggach, S. Parsons, S. P. Perlepes, G. Christou, E. K. Brechin, *J. Am. Chem. Soc.*, **2007**, *129*, 2754.
11. K. Wieghardt, K. Pohl, I. Jibril, G. Huttner, *Angew. Chem. Int. Ed.*, **1984**, *23*, 77.
12. A.L. Barra, P. Debrunner, D. Gatteschi, C. E. Schulz, R. Sessoli, *Europhys. Lett.*, **1996**, *35*, 133.
13. C. Delfs, D. Gatteschi, L. Pardi, R. Sessoli, K. Wieghardt, D. Hanke, *Inorg Chem.*, **1993**, *32*, 3099.
14. (a) S. L. Heath and A. K. Powell, *Angew. Chem. int. Ed.*, **1992**, *31*, 191. (b) 15. A. K. Powell, S. L. Heath, D. Gatteschi, L. Pardi, R. Sessoli, G. Spina, F. Del Giallo and F. Pieralli, *J. Am. Chem. SOC.* **1995**, *117*, 2491
15. J. C. Goodwin, R. Sessoli, D. Gatteschi, W. Wernsdorfer, A. K. Powell, and S. L. Heath, *J. Chem. Soc., Dalton Trans.*, **2000**, 1835.

16. A. T. Tasiopoulos, A. Vinslava, W. Wernsdorfer, K. A. Abboud, G. Christou, *Angew. Chem. Int. Ed.*, **2004**, *43*, 2117.
17. (a) H. A. Lowenstam and S. Weiner, *On Biomineralization*, Oxford University Press, Oxford, **1989**; (b) S. Mann, *Biomimetic Materials Chemistry*, VCH, New York, **1996**.
18. S. Mann, *Biomineralization: Principles and Concepts in Bioinorganic Materials Chemistry*, Oxford Univ. Press: New York, **2001**.
19. S. Weiner, I. Sagi, L. Addadi, *Science* **2005**, *309*, 1027.
20. Y. Politi, T. Arad, E. Klein, S. Weiner, L. Addadi, *Science*, **2004**, *306*, 1161.
21. L. Addadi, M. Geva, *Cryst. Eng. Comm.* **2003**, *5*, 140.
22. D. G. Barnes, *Science*, **1970**, *170*, 1305.
23. J. Aizenberg, G. Lambert, S. Weiner, L. Addadi, *J. Am. Chem. Soc.*, **2002**, *124*, 32.
24. K. Simkiss, K. Wilbur, *Biomineralization. Cell Biology and Mineral Depositions*, Academic Press: San Diego, **1989**.
25. (a) E. Beniash, J. Aizenberg, L. Addadi, S. Weiner, *Proc. R. Soc. Lond. Ser. B*, **1997**, *264*, 461; (b) E. Beniash, L. Addadi, S. Weiner, *J. Struct. Biol.* **1999**, *125*, 50.
26. F. C. Meldrum, *Int. Mater. Rev.*, **2003**, *48*, 187.
27. F. J. Wiercinski, *Biol. Bull.* **1989**, *176*, 195.
28. J. K. J. Jaiswal, *Biosci.* **2001**, *26*, 357.
29. D. N. Trifonov, V. D. Trifonov, *Chemical elements: How they were discovered*, MIR Publishers: Moscow, **1982**.
30. S. J. Ringer, *Physiol.*, **1883**, *4*, 29.
31. S. Ringer, H. J. Sainsbury, *Physiol.*, **1894**, *16*, 1.
32. C. C. Mooren, R. K. H. Kinne, *Biochim. Biophys. Acta*, **1998**, *1406*, 127.
33. A. K. Campbell, *Survey Biochem. Anal.*, **1988**, *19*, 485.
34. P. Chakaborty, *Biochemistry*, **1990**, *29*, 651.
35. P. A. Price, *J. Biol. Chem.*, **1975**, *250*, 1981.
36. M. G. Goodwin, C. Anthony, *Biochem. J.*, **1996**, *318*, 673.
37. C. E. Mortimer, *Chemie*, Georg Thime Verlag: Stuttgart, **1996**.
38. T. Loering, M. H. Moore, R. K. Khama, *Spectrochim. Acta A*, **1991**, *47*, 255.
39. Holleman, A. F.; Wiberg, E. *Lehrbuch der Anorganischen Chemie*, Walter de Gruyter: Berlin, 1995.
40. E. Loste, R. M. Wilson, R. Seshadri, F. C. Meldrum, *J. Crys. Growth*, **2003**, *254*, 206.
41. X. Xu, J. T. Han, K. Cho, *Chem. Mater.*, **2004**, *16*, 1740.
42. E. DiMasi, S. Y. Kwak, F. F. Amos, M. J. Olszta, D. Lush, L. B. Gower, *Phys. Rev. Lett.* **2006**, *97*, 045503.
43. G. H. Nancollas, K. J. Sawada, *Petrol. Technol.*, **1982**, *34*, 645.
44. P. G. Koutsoukos, C. G. Kontoyannis, *J. Chem. Soc.* **1984**, *80*, 1181.
45. P. Kjellin, K. Holmberg, M. Nyden, *Colloids Surf. A*, **2001**, *194*, 49.
46. J. J. J. M. Donners, B. Heywood, E. W. Meijer, R. Nolte, Sommerdijk, *N. Chem. Eur. J.* **2002**, *8*, 2561.
47. J. J. J. M. Donners, B. R. Heywood, E. W. Meijer, R. J. M. Nolte, C. Roman, A. P. H. J. Schenning, N. A. J. M. Sommerdijk, *Chem. Commun.*, **2000**, *19*, 1937.

48. A. Xu, Q. Yu, W. Dong, M. Antonietti, H. Cölfen, *Adv. Mater.* **2005**, *17*, 2217.
49. G. T. Zhou, Y. F. Zheng, *J. Mater. Sci. Lett.*, **1998**, *17*, 905.
50. M.; Okumura, Y. Kitano, *Geochim. Cosmochim. Acta*, **1985**, *50*, 49.
51. W. H. Taft, *Developments in sedimentology*, vol 9B, eds. G. V. Chilingar, H. J. Bissell, R. W. Fairbridge, Elsevier: Netherlands, **1967**.
52. T. Ogino, T. Susuki, K. J. Sawada, *Cryst. Growth* **1990**, *100*, 159.
53. M. Okumura, Y. Kitano, *Geochim. Cosmochim. Acta*, **1986**, *50*, 49.
54. S. D. Sims, J. M. Didymus, S. J. Mann, *Chem. Soc., Chem. Commun.*, **1995**, 1031.
55. S. J. Zawacki, P. Koutsoukos, M. H. Salimi, G. H. Nancollas, *ACS Symposium* **1986**, 322.
56. A. Mucci, *Geochim. Cosmochim. Acta*, **1986**, *50*, 2255.
57. M. M. Reddy, *J. Cryst. Growth*, 1977, *41*, 287.
58. N. Wada, K. Kanamura, T. J. Umegaki, *Colloid Int. Sci.*, 2001, *233*, 65.
59. G. Yu, N. Yao, I. A. Aksay, J. T. Groves, *J. Am. Chem. Soc.* **1998**, *120*, 11977.
60. I. Sondi, E. Matijevic, *J. Colloid Interface Sci.* **2001**, *238*, 208.
61. A. Xu, M. Antonietti, H. Cölfen, Y. Fang, *Adv. Funct. Mater.* **2006**, *16*, 903.
62. J. Rudloff, M. Antonietti, H. Cölfen, J. Petrula, K. Kaluzynsky, S. Penczek, *Macromol. Chem. Phys.*, **2002**, *203*, 627.
63. G. Zhou, J. C. Yu, X. Wang, L. Zhang, *New. J. Chem.*, **2004**, *28*, 1027.
64. H. Tong, W. Ma, L. Wang, P. Wan, J. Hu, L. Cao, *Biomaterials*, **2004**, *25*, 3923.
65. D. Walsh, S. Mann, *Nature*, **1995**, *377*, 320.
66. R. J. Park, F. C. Meldrum, *Adv. Mater.*, **2002**, *14*, 1167.
67. R. J. Park, F. C. Meldrum, *J. Mater. Chem.*, **2004**, *14*, 2291.
68. N. B. J. Hetherington, A. N. Kulak, K. Sheard, F. C. Meldrum, *Langmuir*, **2006**, *22*, 1955.
69. A. Caneschi, D. Gatteschi, R. Sessoli, A.-L. Barra, L. C. Brunel and M. Guillot, *J. Am. Chem. Soc.*, **1991**, *113*, 5873.
70. R. Sessoli, D. Gatteschi, A. Caneschi and M. A. Novak, *Nature*, **1993**, *365*, 141.
71. J. S. Miller, A. J. Epstein, *MRS Bull.* **2000**, *11*, 21.
72. M. Cavallini, J. Gomez-Segura, D. Ruiz-Molina, M. Massi, C. Albonetti, C. Rovira, J. Veciana, and F. Biscarini, *Angew. Chem.* **2005**, *117*, 910.
73. C.-I Yang, W. Wernsdorfer, Y.-J Tsai, G. Chung, T.-Sh Kuo, G.-H Lee, M. Shieh, H.-L. Tsai, *Inorg. Chem.* **2008**, *47*, 1925.
74. (a) R. T. W. Scott, S. Parsons, M. Murugesu, W. Wernsdorfer, G. Christou, and E. K. Brechin, *Angew. Chem.* **2005**, *117*, 6698; (b) A. Mukherjee, C. Boskovic, and R. W. Gable, *Acta Cryst.* **2007**, *C63*, m71.
75. R. Bagai, K. A. Abboud, G. Christou, *Dalton Trans.*, **2006**, 3306.
76. L. M. Wittick, L. F. Jones, P. Jensen, B. Moubaraki, L. Spiccia, K. J. Berry, K. S. Murray, *Dalton Trans.*, 2006, 1534.
77. C.-H. Ge, Z.-H Ni, C.-M. Liu, Ai-Li Cui, D.-Q Zhang, H.-Z Kou, *Inorg. Chem. Commun.* **2008**, *11*, 675.
78. J. T. Brockman, T. C. Stamatatos, W. Wernsdorfer, K. A. Abboud, G. Christou, *Inorg. Chem.*, **2007**, *46*, 9160.

79. T. Stamatatos, K. A. Abboud, W. Wernsdorfer, G. Christou, *Angew. Chem. Int. Ed.*, **2007**, *46*, 884.
80. M. Manoli, A. Prescimone, R. Bagai, A. Mishra, M. Murugesu, S. Parsons, W. Wernsdorfer, G. Christou, E. K. Brechin, *Inorg. Chem.*, **2007**, *46*, 6968.
81. M. Murugesu, W. Wernsdorfer, K. A. Abboud, E. K. Brechin, G. Christou, *Dalton Trans.*, **2006**, 2285.
82. M. Murugesu, M. Habrych, W. Wernsdorfer, K. A. Abboud, G. Christou, *J. Am. Chem. Soc.*, **2004**, *126*, 4766.
83. A. J. Tasiopoulos, A. Vinslava, W. Wernsdorfer, K. A. Abboud, G. Christou, *Angew. Chem. Int. Ed.*, **2004**, *43*, 2117.
84. M. Murugesu, J. Raftery, W. Wernsdorfer, G. Christou, E. K. Brechin, *Inorg. Chem.*, **2004**, *43*, 4203.
85. (a) G. M. Sheldrick, SHELXTL 5.1, Bruker AXS, Inc., 6300 Enterprise Lane, Madison, WI 53719-1173, USA, **1997**; (b) G.M. Sheldrick, *Acta Cryst.*, **2008**, *A64*, 112.
86. W. Liu, H. H. Thorp, *Inorg. Chem.* **1993**, *32*, 4102.
87. (a) J. E. McGrady, and R. Stranger, *J. Am. Chem. Soc.* **1997**, *119*, 8512. (b) C. D. Delfs, and R. Stranger, *Inorg. Chem.* **2001**, *40*, 3061. (b) K. Wieghardt, U. Bossek, D. Ventur, J. Weiss, *J. Chem. Soc., Chem. Commun.* **1985**, 347.
88. J. P. Vincent, H. Tsai, A. G. Blackman, S. Wang, P. D. W. Boyd, K. Folting, J. C. Huffman, E. B. Lobkovsky, D. N. Hendrickson, G. Christou, *J. Am. Chem. Soc.* **1993**, *115*, 12353.
89. T. C. Stamatatos, K. A. Abboud, W. Wernsdorfer, and G. Christou, *Angew. Chem. Int. Ed.* **2006**, *45*, 4134.
90. W. Wernsdorfer, *Adv. Chem. Phys.* **2001**, *118*, 99.
91. E. E. Moushi, T. C. Stamatatos, W. Wernsdorfer, V. Nastopoulos, G. Christou, A. J. Tasiopoulos, *Angew. Chem. Int. Ed.* **2006**, *45*, 7722.
92. (a) F. Jiao and P. G. Bruce, *Adv. Mater.* **2007**, *19*, 657. (b) M. Stanley Whittingham, *Dalton Trans.*, **2008**, DOI: 10.1039/b806372a.
93. R.K. Henderson, *Ph.D. Thesis*, University of East Anglia, Norwich, **1993**.
94. G. Abbas, Y. Lan, G. Kostakis, C. E. Anson, A. K. Powell; *Inorg. Chim. Acta*, **2008**, *361*, 3494.
95. R. J. Glauber, *J. Math. Phys.*, **1963**, *4*, 294.
96. A. Caneschi, D. Gatteschi, N. Lalioti, C. Sangregorio, R. Sessoli, G. Venturi, A. Vindigni, A. Rettori, M. G. Pini and M. A. Novak, *Angew. Chem., Int. Ed.*, **2001**, *40*, 1760.
97. (a) K. Bernot, L. Bogani, A. Caneschi, D. Gatteschi and R. Sessoli, *J. Am. Chem. Soc.* **2006**, *128*, 7947; (b) C. Coulon, H. Miyasaka, R. Clérac, *Struct Bond* **2006** *122*, 163; (c) L. Bogani, A. Caneschi, M. Fedi, D. Gatteschi, M. Massi, M. A. Novak, M.G.Pini, A.Rettori, R.Sessoli, A.Vindigni, *Phys. Rev. Lett.* **2004**, *92*, 207204; (d) R. Lescouezec, J. Vaissermann, C. Ruiz-Perez, F. Lloret, R. Carrasco, M. Julve, M. Verdaguer, Y. Dromzee, D. Gatteschi, W. Wernsdorfer, *Angew. Chem. Int. Ed.* **2003**, *42*, 1483.
98. T. Liu, D. Fu, S. Gao, Y. Zhang, H. Sun, G. Su, Y. Liu, *J. Am. Chem. Soc.* **2003**, *125*, 13976.
99. L. M. Toma, R. Lescouezec, F. Lloret, M. Julve, J. Vaissermann, M. Verdaguer, *Chem. Commun.* **2003**, 1850.
100. E. Pardo, R. Ruiz-Garcia, F. Lloret, J. Faus, M. Julve, Y. Journaux, F. Delgado, C. Ruiz-Perez, *Adv. Mater.* **2004**, *16*, 1597.
101. C. Coulon, R. Clérac, L. Lecren, W. Wernsdorfer, and H. Miyasaka, *Phys Rev B* **2004**, *69*, 132408.
102. R. Clérac, H. Miyasaka, M. Yamashita, and C. Coulon, *J. Am. Chem. Soc.*, **2002**, *124*, 12837.

103. L. Bogani, C. Sangregorio, R. Sessoli, and D. Gatteschi, *Angew. Chem. Int. Ed.* **2005**, *44*, 5817.
104. H. Miyasaka and R. Cle´rac, *Bull. Chem. Soc. Jpn.*, **2005**, *78*, 1725.
105. T. Moeller, D. F. Martin, L. C. Thompson, R. Ferros, G. R. Feistel and W. J. Randall, *chem. Rev.*, **1965**, *65*, 1.
106. H. Miyasaka, and M. Yamashita, *Dalton Trans.*, **2007**, 399.
107. (a) M. L. Kahn, J.-P. Sutter, S. Golhen, P. Guionneau, L. Ouahab, O. Kahn, D. Chasseau, *J. Am. Chem. Soc.* **2000**, *122*, 3413; M. L. Kahn, R. Ballou, P. Porcher, O. Kahn, J. P. Sutter *Chem. Eur. J.* **2002**, *8*, 525.
108. C. Benelli and D. Gatteschi, *Chem. Rev.* **2002**, *102*, 2369.
109. (a) R. Georges, J. J. Borrás-Almenar, E. Coronado, J. Curély and M. Drillon, “*Magnetism: Molecules to Materials I*, Wiley-VCH, J.S. Miller and M. Drillon Ed., p. 1-47; (b) J. C. Bonner, M. E. Fisher, *Phys. Rev.*, 1964, *135*, A640.
- 110 H. A. Lowenstam and S. Weiner, in *On Biomineralization* (Oxford University Press, Oxford, 1989.)
- 111 P. D. Thacker, *Environ. Sci. Technol. A-Pages* **2005**, *39(1)*, 10A
- 112 R. A. Feely, C. L. Sabine, K. Lee, W. Berelson, J. Kleypas, V.J. Fabry, F. J. Millero, *Science* **2004**, *305*, 362.
- 113 S. H. Wei, S. K. Mahuli, R. Agnihotri, L. S. Fan, *Ind. Eng. Chem. Res.* **1997**, *36*, 2141.
- 114 Y. Li, S. Buchi, J. R. Grace, C. J. Lim, *Energy & Fuels* **2005**, *19*, 1927.
- 115 S. F. Chen, S. H. Yu, J. Jiang, F. Li, Y. Liu, *Chem. Mater.* **2006**, *18*, 115.
- 116 G. Falini, S. Fermani, M. Gazzano, A. Ripamonti, *Chem. Eur. J.* **1998**, *4*, 1048.
- 117 T. Sakamoto, A. Oichi, A. Sugawara, T. Kato, *Chem. Lett.* **2006**, *35*, 310.
- 118 T. Kato, T. Amamiya, *Chem. Lett.* **1999**, *24*, 199.
- 119 P. K. Ajikumar, R. Lakshminarayanan, B. O. Ong, S. Valyaveetil, R. M. Kini, *Biomacromolecules* **2003**, *4*, 1321.
- 120 D. Volkmer, M. Fricke, T. Huber, N. Sewald, *Chem. Commun.* **2004**, *16*, 1872.
- 121 C. A. Orme, A. Noy, A. Wierzbicki, M. T. McBride, M. Grantham, H. H. Teng, P. M. Dove, J. J. DeYoreo, *Nature* **2001**, *411*, 775.
- 122 G. Falini, S. Albeck, S. Weiner, L. Addadi, *Science* **1996**, *271*, 67.
- 123 Y. Levi, S. Albeck, A. Brack, S. Weiner, L. Addadi, *Chem. Eur. J.* **1998**, *4*, 389.
- 124 D. B. DeOliveira, R. A. Laursen, *J. Am. Chem. Soc.* **1997**, *119*, 10627.
- 125 R. J. Park, F. C. Meldrum, *J. Mater. Chem.* , **2004**, *14*, 2291.
- 126 S. Albeck, S. Weiner, L. Addadi, *Chem. Eur. J.* **1996**, *2*, 278.
- 127 F. H. Shen, Q. L. Feng, C. M. Wang, *J. Cryst. Growth* **2002**, *242*, 239.
- 128 S. B. Mukkamala, C. E. Anson, A. K. Powell, *J. Inorg. Biochem.* **2006**, *100*, 1128.
- 129 J. J. J. M. Donners, B. R. Heywood, E. W. Meijer, R. J. M. Nolte, N. A. J. M. Sommerdijk, *Chem. Eur. J.* **2002**, *8*, 2561.
- 130 S. H. Yu, H. Cölfen, M. Antonietti, *Phys. Chem. B* **2003**, *107*, 7396.
- 131 H. Cölfen, L. Qi, *Chem. Eur. J.* **2001**, *7*, 106.
- 132 E. Loste, E. Diaz-Marti, A. Zorbakhsh, F.C. Meldrum, *Langmuir* **2003**, *19*, 2830.
- 133 K. Sato, Y. Kumaga, K. Watari, J. Tanaka, *Langmuir* **2004**, *20*, 2979.

- 134 (a) C. Ma, C. Chen, Q. Liu, D. Liao, L. Li and L. Sun, *New J. Chem.*, **2003**, 27, 890; (b) L. C. Yu, Z. F. Chen, H. Liang, C. S. Zhou, Yan Li, *J. Mol. Struct.*, **2005**, 750, 35; (c) M. J. Plater, M. R. St J. Foreman, R. A. Howie, J. M. S. Skakle, E. Coronado, C. J. G. Garcia, T. Gelbrich, M. B. Hursthouse, *Inorg. Chim. Act.* **2001**, 319, 159.
- 135 S. B. Mukkamala, A. K. Powell, *Chem. Commun.* **2004**, 16, 918.
- 136 J. Aizenberg, L. Addadi, *Adv. Mater.* **1996**, 8, 222.
- 137 S. H. Behrens, D. G. Grier, *J. Chem. Phys.* **2001**, 115, 6716.
- 138 A. W. Xu, M. Antonietti, H. Cölfen, and Y. P. Fang, *Adv. Funct. Mater.* **2006**, 16, 903.
- 139 J. J. J. M. Donners, B. R. Heywood, E. W. Meijer, R. J. M. Nolte, C. Roman, A. P. H. J. Schenning and N. A. J. M. Sommerdijk, *Chem. Commun.* **2000**, 19, 1937.
- 140 L. Addadi, S. Raz, S. Weiner, *Adv. Mater.* 2003, 15, 959.
- 141 M. Cao, X. Wu, X. He, and C. Hu, *Langmuir*, **2005**, 21, 6093.
- 142 L. Dupont, F. Portemer and the late M. Figlarz, *J. Mater. Chem.*, **1997**, 75, 797.
- 143 S. H. Yu, H. Cölfen, K. Tauer and M. Antonietti, *Nature Materials*, **2005**, 4, 51.
- 144 X. H. Guo, S. H. Yu, *Cryst Growth Des.*, **2007**, 7, 354.
- 145 WinXPOW 1.07-manual, Stoe & Cie GmbH, Darmstadt, **2000**.
- 146 E. A. Bordeaux, L. N. Mulay, Eds, *Theory and Applications of Molecular Paramagnetism*, John Wiley & Sons, New York, **1976**.

Appendix I: Crystallographic data

Compound	3.1	3.2	3.3
Formula	C ₃₄ H ₆₂ Mn ₆ N ₂ O ₂₉	C _{88.32} H _{149.98} Cl _{6.34} Mn ₁₇ N ₁₂ O _{33.32}	C ₂₇ H ₇₂ Cl ₆ Mn ₂₂ N ₅₄ O _{58.50}
Molecular weight	1286.58	3071.88	3510.77
Cryst size[mm]	0.5×0.4×0.3	0.32×0.18×0.14	0.35×0.32×0.07
colour	Black-brown	Black-brown	Black
Cryst Syst	Triclinic	Triclinic	cubic
Space group	$P\bar{1}$	$P\bar{1}$	$Pa\bar{3}$
T[K]	100 K	100 K	100 K
<i>a</i> [Å]	16.3547(12)	15.1766(6)	21.5248(12)
<i>b</i> [Å]	20.3207(15)	16.6851(7)	21.5248(12)
<i>c</i> [Å]	21.9546(16)	26.4026(11)	21.5248(12)
α [deg]	103.000(6)	97.2440(10)	90.00
β [deg]	103.623(6)	100.9490(10)	90.00
γ [deg]	109.854(6)	105.0310(10)	90.00
<i>V</i> [Å ³]	6287.5(8)	6230.1(4)	9972.8(10)
<i>Z</i>	5	2	4
ρ_{calcd} [g cm ⁻³]	1.699	1.638	2.338
$\mu(\text{Mo K}\alpha)$ [mm ⁻¹]	1.551	1.864	2.961
<i>F</i> (000)	3320	3126	6928
reflns collected	30671	43119	31618
unique reflns	22003	26817	2389
<i>R</i> _{int}	0.0740	0.0271	0.0733
reflns obsd [<i>I</i> > 2σ(<i>I</i>)]	9998	18659	1626
parameters/restraints	1358/0	1428/119	212/8
GOF on <i>F</i> ²	1.386	1.085	1.232
<i>R</i> ₁ [<i>I</i> > 2σ(<i>I</i>)]	0.2729	0.0588	0.0942
w <i>R</i> ₂ (all data)	0.1187	0.1311	0.2604
Larg. residuals [e Å ⁻³]	+1.492/-1.111	+1.123/-0.573	+2.476/-1.781

Compound	3.4	4.3	4.5
Formula	C ₆₀ H ₁₀₂ Fe ₆ N ₈ O ₃₂	C ₂₄ GdH ₂₅ O ₉	C ₂₄ DyH ₂₅ O ₉
Mr	1782.60	614.69	619.94
Cryst size[mm]	0.38×0.31×0.26	0.32×0.25×0.08	0.28×0.15×0.11
colour	Green	Light yellow	Colorless
Cryst Syst	triclinic	triclinic	triclinic
Space group	$P\bar{1}$	$P\bar{1}$	$P\bar{1}$
T[K]	100 K	100 K	100 K
<i>a</i> [Å]	13.3404(7)	9.6795(10)	9.6624(6)
<i>b</i> [Å]	17.5299(10)	10.3757(11)	10.3438(7)
<i>c</i> [Å]	16.3050(9)	13.1729(14)	13.1697(7)
α [deg]	90.015(1)	92.577(2)	92.631(1)
β [deg]	93.889(1)	90.780(2)	90.759(2)
γ [deg]	90.008(1)	116.763(2)	116.637(2)
<i>V</i> [Å ³]	3804.2(4)	1179.2(2)	1174.47(12)
<i>Z</i>	2	2	2
ρ_{calcd} [g cm ⁻³]	1.556	1.731	1.753
$\mu(\text{Mo K}\alpha)$ [mm ⁻¹]	1.203	2.864	3.233
<i>F</i> (000)	1860	610	614
reflns collected	26321	7232	7429
unique reflns	16353	4095	4526
<i>R</i> _{int}	0.0212	0.0398	0.0333
reflns obsd [<i>I</i> > 2σ(<i>I</i>)]	14762	3583	3755
parameters/restraints	867/16	316/3	316/21
GOF on <i>F</i> ²	1.615	1.057	1.057
<i>R</i> ₁ [<i>I</i> > 2σ(<i>I</i>)]	0.0789	0.0400	0.1164
w <i>R</i> ₂ (all data)	0.2048	0.0926	0.1164
Larg. residuals [e Å ⁻³]	+2.556/-1.467	+2.143/-2.156	+2.118/-2.926

Appendix II: List of crystalline compounds

- 3.1 $[(\text{PtolH})_4(\text{O}_2\text{CMe})_6(\mu_6\text{-O})\text{Mn}^{\text{III}}_6] \cdot 1.5\text{en}$
- 3.2 $[\text{Mn}^{\text{III}}_{11}\text{Mn}^{\text{II}}_6(\mu_4\text{-O})_8(\mu_3\text{-Cl})_4(\mu_5\text{-O}_2\text{CMe})_2(\text{DPD})_{10}\text{Cl}_{2.34}(\text{O}_2\text{CMe})_{0.66}(\text{py})_3(\text{MeCN})_2] \cdot 7\text{MeCN}$
- 3.3 $[\{\text{Mn}^{\text{III}}_{12}\text{Mn}^{\text{II}}_9(\mu_4\text{-O})_8(\text{glycH})_{12}(\mu\text{-}1,1\text{-N}_3)_6(\text{OH}_2)_6(\text{N}_3)_{1.5}\} \{\text{Mn}^{\text{II}}(\mu\text{-}1,3\text{-N}_3)_{4.5}(\text{OH}_2)_{1.5}\}] \text{Cl}_4 \cdot \text{ca.} 7.5\text{H}_2\text{O}$
- 3.3a $[\{\text{Mn}^{\text{III}}_{12}\text{Mn}^{\text{II}}_9(\mu_4\text{-O})_8(\text{glycH})_{12}(\mu\text{-}1,1\text{-N}_3)_6(\text{OH}_2)_6(\text{N}_3)_{1.5}\} \{\text{Mn}^{\text{II}}(\mu\text{-}1,3\text{-N}_3)_{4.5}(\text{OH}_2)_{1.5}\}] \text{Cl}_4 \cdot \text{ca.} 4\text{H}_2\text{O}$
- 3.4 $[\text{Fe}_6\text{O}_2(\text{Piv})_6(\text{PdolH})_6](\text{NO}_3)_2 \cdot 2\text{CH}_3\text{CN}$
- 4.1 $[\text{Pr}(\text{PhCOO})_3(\text{EtglyH}_2)(\text{MeOH})]$
- 4.2 $[\text{Nd}(\text{PhCOO})_3(\text{EtglyH}_2)(\text{MeOH})]$
- 4.3 $[\text{Gd}(\text{PhCOO})_3(\text{EtglyH}_2)(\text{MeOH})]$
- 4.4 $[\text{Tb}(\text{PhCOO})_3(\text{EtglyH}_2)(\text{MeOH})]$
- 4.5 $[\text{Dy}(\text{PhCOO})_3(\text{EtglyH}_2)(\text{MeOH})]$
- 4.6 $[\text{Ho}(\text{PhCOO})_3(\text{EtglyH}_2)(\text{MeOH})]$
- 4.7 $[\text{Er}(\text{PhCOO})_3(\text{EtglyH}_2)(\text{MeOH})]$

Appendix III: List of abbreviations

Chemical Terms

ACC	Amorphous calcium carbonate
BDC	Benzene dicarboxylic acid
BTC	Benzene tricarboxylic acid
DPPH ₂	2,2-dimethyl propane-1,3-diol

EtglyH ₂	HOCH ₂ CH ₂ OH (Ethylene glycol)
Fe ₃	[Fe ₃ (μ ₃ -O)(piv) ₆ (H ₂ O) ₃]piv
Fe ₁₉	[Fe ₁₉ (heidi) ₁₀ (OH) ₄ O ₆ (H ₂ O) ₁₂] ⁻
glycH ₃	Propan-1,2,3-triol (glycerol)
heidi	N(CH ₂ COOH) ₂ (CH ₂ CH ₂ OH)
H ₃ L	2,6-bis(hydroxy-methyl)-4-methylphenol
hpdtaH ₅	1,3-diamino-2-hydroxypropane- <i>N,N,N',N'</i> -tetraacetic acid
Mn _{12-ac}	[Mn ₁₂ O ₁₂ (CH ₃ COO) ₁₆ (H ₂ O) ₄]·2CH ₃ COOH·4H ₂ O
Mn ₁₉	[Mn ^{III} ₁₂ Mn ^{II} ₇ (μ ₄ -O) ₈ (μ ₃ ,η ¹ -N ₃) ₈ (HL) ₁₂ (MeCN) ₆]Cl ₂ ·10MeOH·MeCN
Mn ₁₇	[Mn ^{III} ₁₁ Mn ^{II} ₆ (μ ₄ -O) ₈ (μ ₃ -Cl) ₄ (μ ₅ -O ₂ CMe) ₂ (DPD) ₁₀ Cl _{2.34} (O ₂ CMe) _{0.66} (py) ₃ (MeCN) ₂]·7MeCN
Mn ₂₁	[{Mn ^{III} ₁₂ Mn ^{II} ₉ (μ ₄ -O) ₈ (glycH) ₁₂ (μ-1,1-N ₃) ₆ (OH ₂) ₆ (N ₃) _{1.5} } {Mn ^{II} (μ-1,3-N ₃) _{4.5} (OH ₂) _{1.5} }]Cl ₄ · <i>ca.</i> 7.5H ₂ O
PdolH ₂	Propan-1,2-diol
PtolH ₄	2,2-di(methyl hydroxyl) propan-1,3-diol (pentaerythritol)
saoH ₂	2-hydroxybenzaldehyde oxime
tacn	1,4,7-triazacyclononane

Miscellaneous

<i>B</i>	magnetic flux density
<i>b</i>	Broad
<i>D</i>	Zero-field splitting parameter
DLS	Dynamic light scattering
FT	Fourier-transform
<i>H</i>	Magnetic field

H_c	coercive field
IR	Infra-red
M	Magnetization
NMR	Nuclear magnetic resonance
Pa	Pascal
s	Strong
vs	Very strong
S	Spin state
SCM	Single-chain magnet
SEM	Scanning electron microscopy
SMM	Single-molecule magnet
SQUID	Superconducting Quantum Interference Devices
T	Temperature
T_B	Blocking temperature
T_c	Curie temperature
T_N	Néel temperature
w	Weak
vw	Very weak
ZFS	Zero-field splitting
χ	Molar magnetic susceptibility
ΔE	Energy barrier
μ_0	Permeability
μ_B	Bohr magneton
μ_r	Relative permeability

Appendix IV: List of figures

Figure 1.1:	χ^{-1} versus T plot and χ versus T plot for different kinds of materials	3
Figure 1.2:	The illustration of a magnetization hysteresis loop	4
Figure 1.3:	Structure of $[\text{Mn}_{12}\text{O}_{12}(\text{CH}_3\text{COO})_{16}(\text{H}_2\text{O})_4] \cdot 2\text{CH}_3\text{COOH} \cdot 4\text{H}_2\text{O}$	7
Figure 1.4:	Energy level diagram of Mn12-ac ($S = 10$)	7
Figure 1.5:	The structure and magnetic properties of $[\text{Mn}^{\text{III}}_{12}\text{Mn}^{\text{II}}_7(\mu_4\text{-O})_8(\mu_3, \eta^1\text{-N}_3)_8(\text{HL})_{12}(\text{MeCN})_6]$	9
Figure 1.6:	The structure and magnetic hysteresis of $[\text{Mn}^{\text{III}}_6\text{O}_2(\text{Et-sao})_6(\text{O}_2\text{CPh}(\text{Me})_2)_2(\text{EtOH})_6]$	10
Figure 1.7:	Structure of $[\text{Fe}_8\text{O}_2(\text{OH})_{12}(\text{tacn})_6]$ with iron spin centers	11
Figure 1.8:	The structure and magnetic properties of $[\text{Fe}_{19}(\text{heidi})_{10}(\text{OH})_4\text{O}_6(\text{H}_2\text{O})_{12}]$	12
Figure 1.9:	The structure and magnetic properties of $[\text{Mn}_{84}\text{O}_{72}(\text{O}_2\text{CMe})_{78}(\text{OMe})_{24}(\text{OH})_6(\text{MeOH})_{12}(\text{H}_2\text{O})_{42}]$	13
Figure 1.10:	Few examples of natural biominerals.	15
Figure 1.11:	SEM showing the expression of (001) tabular faces in aragonite crystals grown in the presence of Li^+	18
Figure 1.12:	Various morphologies of calcium carbonate	20
Figure 3.1:	Poly-alkoxy ligands used in the synthesis of manganese and iron clusters	25
Figure 3.2:	Molecular view of $[(\text{PtolH})_4(\text{O}_2\text{CMe})_6(\mu_6\text{-O})\text{Mn}^{\text{III}}_6] \cdot 1.5\text{en}$ (3.1)	26
Figure 3.3:	Magnetic data-plot for 3.1	29
Figure 3.4:	The structure of $[\text{Mn}^{\text{III}}_{11}\text{Mn}^{\text{II}}_6(\mu_4\text{-O})_8(\mu_3\text{-Cl})_4(\mu_5\text{-O}_2\text{CMe})_2(\text{DPD})_{10}\text{Cl}_{2.34}(\text{O}_2\text{CMe})_{0.66}(\text{py})_3(\text{MeCN})_2] \cdot 7\text{MeCN}$ (3.2)	32
Figure 3.5:	Polyhedral representations of the cores of the Mn_{17} cluster of 3.2 (A) and the Mn_{19} (B) clusters	33

Figure 3.6:	The Jahn-Teller elongations are shown in compound 3.2	33
Figure 3.7:	Polyhedral representation of octahedral Mn^{III}_6 units in compound 3.2 (A) and in Mn_{19} cluster. (B).	33
Figure 3.8:	Susceptibility, magnetization and hysteresis plot for compound 3.2	35
Figure 3.9:	The core of the Mn_{21} aggregate in 3.3	39
Figure 3.10:	Representation of the concentric polyhedra present in compound 3.3	40
Figure 3.11:	The disorder of the organic and terminal ligands in the structure of 3.3 .	40
Figure 3.12:	Different kinds of representation of the unit cell of 3.3	42
Figure 3.13:	Magnetic susceptibility and the magnetization plots for 3.3 and 3.3a	43
Figure 3.14:	Thermogravimetric analysis of compound 3.3	46
Figure 3.15:	Powder XRD analysis of 3.3	47
Figure 3.16:	Presence of the characteristic peak for nitrate group in the IR spectra of the heated sample of 3.3	48
Figure 3.17:	Smooth crystal faces of 3.3 were observed before heating	49
Figure 3.18:	Porous crystal surface of 3.3 after heat treatment	50
Figure 3.19:	Capacitance measurements for the porous $\beta\text{-MnO}_2$	51
Figure 3.20:	Molecular structure of compound 3.4	54
Figure 3.21:	Magnetic susceptibility and magnetization of compound 3.4	55
Figure 4.1:	Structural view of of $[\text{Gd}(\text{PhCOO})_3(\text{EtglyH}_2)(\text{MeOH})]$ chain, 3.3	61
Figure 4.2:	The calculated and experimental powder XRD patterns for 4.3	62
Figure 4.3:	χT versus T plot for $[\text{Pr}(\text{PhCOO})_3(\text{EtglyH}_2)(\text{MeOH})]$ chain 4.1	64
Figure 4.4:	χT versus T plot for $[\text{Nd}(\text{PhCOO})_3(\text{EtglyH}_2)(\text{MeOH})]$ chain, 4.2	64
Figure 4.5:	χT versus T plot for $[\text{Gd}(\text{PhCOO})_3(\text{EtglyH}_2)(\text{MeOH})]$ chain, 4.3	65
Figure 4.6:	χT versus T plot for $[\text{Tb}(\text{PhCOO})_3(\text{EtglyH}_2)(\text{MeOH})]$ chain, 4.4	66

Figure 4.7:	Magnetic data for [Dy(PhCOO) ₃ (EtglyH ₂)(MeOH)] chain 4.5	67
Figure 4.8:	χT versus T plot for [Ho(PhCOO) ₃ (EtglyH ₂)(MeOH)] chain, 4.6	68
Figure 4.9:	χT versus T plot for [Er(PhCOO) ₃ (EtglyH ₂)(MeOH)] chain, 4.7	69
Figure 4.10:	The M versus H plots for 4.1-4.7	71
Figure 4.11:	The M versus HT^{-1} plots for 4.1-4.7	72
Figure 4.12:	Magnetic susceptibility and magnetization fit for compound 4.3	73
Figure 5.1:	Templates used in biomineralization of CaCO ₃	78
Figure 5.2:	SEM images of calcite formation after 6 h, 12 h and 24 h	80
Figure 5.3:	A complete view and a trumpet-like unit of <i>Discophaera Tubifera</i> .	81
Figure 5.4:	The IR spectra and powder XRD pattern of the precursor of the microtrumpets	82
Figure 5.5:	The SEM images of the dumbbell-shaped calcite obtained from the solution during the DLS study	83
Figure 5.6:	(A) A close-up view of the CaCO ₃ -microtrumpets	84
Figure 5.7:	The (DLS) study for the investigation of the growth of the microtrumpets	85
Figure 5.8:	Schematic representation of the trumpet formation	86
Figure 5.9:	SEM images of the calcite dumbbells obtained at different pH	87
Figure 5.10:	Cross-linked structures at different pH values	87
Figure 5.11:	Different morphologies of CaCO ₃ at different Ca : hpdta concentration ratio	89
Figure 5.12:	Time-dependence study of vaterite-ball formation using 1,2,4-BTC	91
Figure 5.13:	IR spectrum and powder XRD pattern of the sample showing the presence of ACC and vaterite in the sample	93
Figure 5.14:	Time-dependence study of the vaterite-ball formation using 1,3,5-BTC	95
Figure 5.15:	CaCO ₃ structures formed by using 1,2-BDC, 1,3-BDC, and 1,4-BDC.	95
Figure 5.16:	Time-dependence study of BaCO ₃ structure formation using 1,2,4-BDC	98

Figure 5.17: A broken structure of the BaCO ₃ morphology formed after 96 hours.	
A close-up view of the radially arranged nanofibres.	99
Figure 5.19: Study of the effect of pH on the BaCO ₃ structures	101
Figure 5.20: Time-dependence study of SrCO ₃ structure formation	102
Figure 5.21: IR spectra and powder XRD patterns of SrCO ₃ sample formed using 1,2,4-BTC	103
Figure 5.22: Study of pH effect on the SrCO ₃ structures	104

Appendix V: List of schemes

Scheme 3.1: Synthesis of compound 3.1 is shown. PtolH ₄ and en represent pentaerythritol and ethylenediamine, respectively.	27
Scheme 3.2: Synthesis of compound 3.4 is shown	53
Scheme 4.1: Synthetic scheme for the preparation of [Ln(PhCOO) ₃ (EtglyH ₂)(MeOH)] (Ln = Pr, Nd, Gd, Tb, Dy, Ho and Er) chains.	60

Appendix VI: List of tables

Table 4.1: The electronic configurations and the ionic radii are given for the lanthanide atoms and ions.	59
Table 4.2: A comparison of the susceptibility data for the isostructural chain compounds is shown.	70

CURRICULUM VITAE

Sanjit Nayak

1. PERSONAL INFORMATIONS

Date of birth: 02.01.1981

Place of birth: Bankura (WB, India)

Nationality: Indian

Work address

Institut für Anorganische Chemie

Universität Karlsruhe (TH)

Engesserstrasse 15

Karlsruhe 76131

Germany

Home address

Karl Wilhelm strasse-22

Karlsruhe 76131

Germany

2. EDUCATION

(A) Pursuing Ph.D. since September, 2005.

Universität Karlsruhe (Germany)

Research title: "The Use of Coordination Chemistry Principles to Control Aggregation Processes of Metal Ions"

Supervisor: Prof. Annie K. Powell

(B) M.Sc. in Chemistry, July, 2005.

Indian Institute of Technology, Kanpur, India

Research title: "Modular Chemistry with New Multidentate Ligands: Self Assembly to Supramolecular Metal Organic Frameworks"

Supervisor: Prof. Parimal. K. Bharadwaj

(C) B.Sc. in Chemistry (with Honours), 2003.

The University of Burdwan, West Bengal, India.

(D) Higher Secondary (10+2 level) Education, 1999.

Burdwan Christian Missionary High School, West Bengal, India.

(E) Secondary (10th level), 1997.

Burdwan Banipith High School.

3. TEACHING EXPERIENCES, RESPONSIBILITIES, TECHNICAL EXPERTISE:

- (A) Responsible for undergraduate inorganic chemistry laboratories.
- (B) Assigned projects and supervised undergraduate students.
- (C) Technical operating knowledge:
STOE-IPDS II single-crystal diffractometer, Powder diffractometer (STOE), Perkin Elmer Spectrum One I.R spectrophotometer, Zetasizer spectrometer, TGA/DTA.
- (D) Familiar with:
SQUID magnetometry, SEM.

4. PUBLICATIONS

- (1). S. Nayak, L. Yanhua, C. A. Anson, R. Clérac, A. K. Powell, “Concentric Archimedean Polyhedra: $Mn^{III}_{12}Mn^{II}_9$ Aggregates Linked into a Cubic Network”. (*Chem. Commun*, 2008, 5698)
- (2). S. Nayak, S. Neogi, P. K. Bharadwaj, “A Series of Metal Organic Frameworks Formed by a new Tripodal Ligand and Several Transition Metals”. (Processing)
- (3). S. Nayak, L. M. C. Beltran, Y. Lan, R. Clérac, N. G. R. Hearn, W. Wernsdorfer, C. E. Anson, and A. K. Powell, “A New High-Spin $Mn^{II}_6Mn^{III}_{11}$ Complex with $S = 28 \pm 1$ Spin Ground State”. (in press, *CrystEngComm*)
- (4). S. Nayak, Sarali Malik, A. K. Powell, “A sponge-like morphology of MnO_2 ”. (Processing)
- (5). S. Nayak and A. K. Powell, “A Systematic Study on the $CaCO_3$ -Microtrumpet Formation”, *Abstract ICBICXIII*, 2007.
- (6). S. Nayak, L. Yanhua, C. E. Anson, R. Clérac and A. K. Powell, “An Assembly of Concentric Archimedean Polyhedrons: A 3D Network with Big Mn_{21} Cluster Units”, *Abstract ICC38*, 2008.
- (7). S. Nayak, L. M. C. Beltran, Y. Lan, R. Clérac, N. G. R. Hearn, W. Wernsdorfer, C. E. Anson, and A. K. Powell, “A New High Spin $Mn^{II}_6Mn^{III}_{11}$ Cluster with $S = 28 \pm 1$ ”, *Abstract ICMM*, 2008.

